UC Davis
UC Davis Electronic Theses and Dissertations

Title

Sublimation Cooling for CubeSat Waste Heat Rejection

Permalink

https://escholarship.org/uc/item/4td2f8w3

Author

Moses, Janine Rosenberg

Publication Date

2024

Peer reviewed|Thesis/dissertation

eScholarship.org Powered by the California Digital Library
University of California

Sublimation Cooling for CubeSat Waste Heat Rejection

By

JANINE ROSENBERG MOSES

THESIS

Submitted in partial satisfaction of the requirements for the degree of

MASTER OF SCIENCE

in

Mechanical and Aerospace Engineering

in the

OFFICE OF GRADUATE STUDIES

of the

UNIVERSITY OF CALIFORNIA

DAVIS

Approved:

Stephen K. Robinson, Chair

Vinod Narayanan

Eugene K. Ungar

Committee in Charge

2024

Contents

Contents ii

List of Figures v

List of Tables ix

List of Acronyms x

Nomenclature xi

Acknowledgements xiii

Abstract xv

1 Introduction 1
- 1.1 Overview . . . 1
- 1.2 CubeSat Thermal Control . . . 3
- 1.3 Overview of a Sublimator . . . 6
- 1.4 Transient Start-Up . . . 10
- 1.5 Derivation of Phase Change Heat Transfer Equation . . . 11
- 1.6 Advantages & Disadvantages of a Sublimator . . . 12

2 Literature Review 14
- 2.1 1960s-1970s . . . 16
- 2.2 1980s-1990s . . . 17
- 2.3 2000s-2010s . . . 23
- 2.4 Summary . . . 26

3 CubeSat Thermal Control System 28
- 3.1 TCS Components . . . 28
- 3.2 Sizing a Sublimator . . . 33
- 3.3 CubeSat Systems Considerations . . . 36
  - 3.3.1 Thrust from Sublimator . . . 36
  - 3.3.2 Solar Radiation Heating . . . 38
  - 3.3.3 Miscellaneous Considerations . . . 40

4 Sublimator Model 42

4.1 Goals of the Model . . . 42
4.2 Shortcomings & Knowledge Gaps . . . 43
4.3 Thermal Resistance Circuit . . . 45
4.4 Assumptions . . . 47
4.5 Conduction Model (Temperature) . . . 52
4.6 Mass Flow Model (Pressure) . . . 56
4.6.1 Evaporation/Sublimation Rate Limit . . . 56
4.6.2 Scaling of Evaporation/Sublimation Rate . . . 59
4.6.2.1 Porous Media . . . 60
4.6.2.2 Flow Regimes . . . 63
4.6.2.3 Modeling Flow through Porous Media . . . 66
4.7 Evaporation in the Sublimator . . . 70
4.7.1 Evaporation Mode . . . 70
4.7.1.1 Comparison of Pressures . . . 70
4.7.1.2 Comparison of Permeability Coefficients . . . 72
4.8 Combining Models . . . 77
4.9 Summary . . . 82

5 Hardware Characterization & Experiment 84
5.1 3D Imaging . . . 85
5.1.1 PuMA . . . 86
5.2 Water Vapor Flow Experiment . . . 88
5.2.1 Experimental Set-Up . . . 88
5.2.1.1 Sensors Suite . . . 93
5.2.2 Results: Flow Regime . . . 94
5.2.3 Results: Uncertainty Analysis . . . 95
5.2.4 Results: Assumptions & Observations . . . 97
5.2.4.1 Assumption #1: Ideal Gas . . . 97
5.2.4.2 Assumption #2: Isothermal . . . 99
5.2.4.3 Assumption #3: Low Speed Flow . . . 102
5.2.4.4 Observation #1: Adiabatic . . . 104
5.2.4.5 Observation #2: Isenthalpic . . . 106
5.2.5 Results: Pressure Drop . . . 108
5.2.6 Results: Saturation Temperature Comparison . . . 111
5.2.7 Results: Mass Flow Rate & Steady-State Assumption . . . 113
5.2.8 Results: Mass Flow Rate - Pressure Drop Ratio . . . 116
5.3 Lessons Learned . . . 118
5.4 Future Improvements . . . 119

6 Model Validation 120
6.1 Ideal Gas Assumption for a CubeSat . . . 121
6.2 Weber Equation & Experimental Data: Pore Size . . . 121
6.3 Weber Equation & Experimental Data: Mass Flow Rate - Pressure Drop Ratio 122
6.4 Comparison: Historical & Experimental Data . . . 124
6.5 Realizability of Sublimator Design Parameters . . . 127

7 Conclusion **131**
7.1 Summary of Contributions 131
7.2 Open Research Areas & Future Work 132

Bibliography **136**

Appendix A **143**

List of Figures

1.1 NASA CHOMPTT (2018) on-orbit temperature data (blue) and steady-state high temperature predictions (red) [4]. . . . 3
1.2 Phase diagram of water with the triple point pressure/temperature indicated [11]. Note that at pressures above the critical point, the relationship between ice and liquid water is unusual and counter-intuitive [12]. . . . 6
1.3 Basic components of a sublimator in which heat flux is applied into the bottom of the aluminum frame. Feedwater reservoir and tubes not shown. . . . 8
1.4 NASA EMU sublimator [19]. . . . 9
1.5 Water flow through porous layer for application of the first law of thermodynamics. 10

2.1 The Apollo spacesuit PLSS, left [32] and the Apollo Lunar Module, center/right [33, 34]. . . . 16
2.2 NASA EMU sublimator [16, 19]. The bottom right image shows the sublimator stack without the porous plate or frame (blue tape is not for flight). Author credit. 18
2.3 Feedwater breakthrough during ground testing on an unspecified sublimator design at Johnson Space Center (year unknown) [37]. . . . 19
2.4 Schematic of the Orlan with the sublimator indicated in red box, left [39], and the sublimator vent in Kretchet PLSS (the Orlan's predecessor), right [40]. . . . 20
2.5 The sublimator from the European Space Suit System (ESSS), left [39], and a visualization of porous plate cut-away to show woven wire layers, right [41]. . . . 22
2.6 X-38 sublimator view from inside crew cabin, left [42], and sublimator hardware at JSC , right (author credit). . . . 23
2.7 Diagram of contaminant-insensitive sublimator (CIS) with the large pores on the vacuum side and small pores on the feedwater side [20]. . . . 23
2.8 Johnson Space Center's sublimator-driven coldplate (SDC) [46] . . . 24
2.9 CNSA's Chang'E-5 thermal control system schematic [49] and images of sublimator test beds [50]. . . . 25

3.1 CAD visualization of a 6U CubeSat with a sublimator thermal control system. Courtesy Katie Ricketts/ UC Davis 2024. . . . 29
3.2 CAD visualization of a 6U CubeSat with a sublimator thermal control system in the sandwich configuration. Courtesy Katie Ricketts/ UC Davis 2024. . . . 29
3.3 EMU feedwater bladder [16]. . . . 30
3.4 Cut-away visualization of a CubeSat sublimator with hardware contacted directly to inner surface of sublimator via thermal paste. . . . 31

3.5 Left: Heat pipe mechanism [56]. Right: aluminum ribbons and braided copper thermal strap examples [57]. 32
3.6 Contribution of disturbances to satellites in earth orbit. Courtesy Adam Zufall [61]. 38

4.1 Side view visualization of a sublimator indicating locations of assumed ice formation. 45
4.2 The "layers" of a sublimator oriented with the heat source to the left of the figure and the vacuum of space to the right of the figure. 46
4.3 The "layers" of a sublimator oriented with the heat source to the left of the figure and the vacuum of space to the right of the figure, represented as a thermal resistance network. 47
4.4 Visualization of water/ice sphere in transient heat transfer problem. 48
4.5 Heisler chart for transient conduction for a sphere [24]. 49
4.2 The "layers" of a sublimator oriented with the heat source to the left of the figure and the vacuum of space to the right of the figure. 53
4.7 Relationship between ice layer thickness, heat flux from the source, and solid-vapor interface temperature for sublimation in a porous media with 15% porosity. 54
4.8 Sublimation/evaporation rate using the Hertz-Knudsen equation and based on interface temperature and pressure. 58
4.9 Historical sublimation (mass flux) compared to the Hertz-Knudsen equation. . . 59
4.10 3D Rendering of X-ray tomography scan of porous samples from Mott Corp using Dragonfly and PuMA software with reported pore sizes of 40 μm (left) and 100 μm (right) [70–72]. 60
4.11 Relationship between mean-squared displacement (MSD) and the diffusion coefficient [80] 63
4.12 Knudsen Number flow regime and visualization (not to scale). 64
4.13 Relationship between Knudsen number, pore radius, and pressure for an example CubeSat sublimator porous media. The grey plane represents the boundary between the rarefied and transition flow regimes. 65
4.14 Visualization of porous media (left) as a bundle of capillary tubes (right). 66
4.15 Relationship between Knudsen number and mass flow rate normalized by pressure drop and area, based on the Weber equation for molecular and transition flow. . 68
4.16 Relationship between vapor region thickness, phase change interface temperature, pore size, and heat flux for a porous media with $\phi = 15\%$. The four surfaces represent four different heat fluxes, from top to bottom: $q" = 12,\ 10,\ 8,\ 6\ kW/m^2$. 69
4.17 Ratio of permeability coefficients compared to Knudsen number Note the transition regime is $10^{-1} < Kn < 10$ and rarefied regime is $10 \leq Kn$. 75
4.18 Representation of evaporaiton location based on relative permeability coefficients for liquid water and water vapor. 76
4.19 Zoom-in of temperature profile in Figures 4.20 - 4.23 to point out the meaning of each point. 78
4.20 Temperature profile within sublimator which incorporates both the solution to the conduction equations and the Weber equation. 78
4.21 Visualization of sublimator with $q" = 12\ kW/m^2$, $\phi = 15\%$, $T_{sv} = -0.15°C$, $r = 1.56\ \mu m$ 79

4.22 Heat flux versus phase change location. Sublimater "layers" are rotated 90°. . . 80
4.23 Temperature profile within sublimator which incorporates both the solution to the conduction equations and the Weber equation for the evaporation case [104]. 81

5.1 Screenshot of Dragonfly: X-Ray of 100 μm pore size, 10 μm voxel, FDK. The magenta areas are the solid stainless steel microstructure and the green areas are the void space. 86
5.2 Phase diagram for water with experiment parameters. 90
5.3 Experiment Schematic 91
5.4 Full experimental set-up. 92
5.5 Water reservoir in chiller bath. PRT probe is taped to the outside of the stainless steel reservoir. Valves 1-3 and the relief valve are also visible and low vacuum pump is in the background. 93
5.6 Test filter assembly, including pressure sensors (top) and temperature sensors (bottom). Water vapor flows from right to left in this image and entrance to vacuum chamber is seen on the left. 93
5.7 Knudsen number as determined by pore size and water vapor saturation pressure, where $T = 21°C$ (average superheated water vapor temperature). The horizontal plane divides the transition and rarefied regimes and the red lines show the vapor pressure range in the experiment. 95
5.8 Propagation of uncertainty in pressure measurements. 96
5.9 Propagation of uncertainty in temperature measurements. 97
5.10 Isenthalpic curves on p-T diagram showing Joule-Thomson coefficient ranges [110]. 99
5.11 Temperature data across filter for $T = -4°C$. 100
5.12 Temperature data across filter for $T = -3°C$. 101
5.13 Temperature data across filter for $T = 0°C$. 101
5.14 Temperature data across filter for $T = 1°C$. 102
5.15 Temperature data across filter for $T = 5°C$. 102
5.16 Mach number versus Knudsen number along the porous plug for each set of temperature trials. 104
5.17 Continuation; thermocouple temperatures in support of validity of adiabatic assumption. Note the y-axis range is only 2.5 degrees and the confidence intervals are not shown. 105
5.18 Thermocouple temperatures in support of validity of adiabatic assumption. Note the y-axis range is only 2.5 degrees and the confidence intervals are not shown. . 106
5.19 Pressure drop across filter porous plug. 109
5.20 Pressure drop across filter porous plug ($P_1 - P_2$ from experiment schematic) with labels pointing to the "pressure drop phenomena". 110
5.21 Water Reservoir Temperature: Measured from temperature probe and calculated from measured saturation pressure. 112
5.22 Mass flow rate for all experiment trials. 114
5.23 Pressure drop across porous filter for $T_{sat} = -3°C$, Trial 2. The green rectangle on the left figure shows the steady-state region and the yellow triangle on both plots show the transient region. 115

5.24 Mass flow rate per pressure drop for all experimental trials. Note that confidence interval is not visible on the logarithmic scale. 117

6.1 Mass flow rate/pressure drop ratio: comparison of Weber model to experimental data. The tortuosity value from PuMA and used in the Weber model is $\tau = 2$. Note that confidence interval is not visible on the logarithmic scale. 123
6.2 Comparison of Weber model to experimental data in terms of Knudsen number. Note that confidence interval is not visible on the logarithmic scale. 124
6.3 Figure 4.20: Temperature profile within sublimator which incorporates both the solution to the conduction equations and the Weber equation. 127
6.4 Figure 4.23: Temperature profile within sublimator which incorporates both the solution to the conduction equations and the Weber equation for the evaporation case [104]. 128
6.5 Temperature distribution for an example of a non-realizable set of sublimator parameters. 129
6.6 Realizable ranges for pore size and porosity for a CubeSat sublimator. 130

A.1 Inputs for tortuosity calculation in PuMA. 145
A.2 PuMA GUI with terminal log (upper left), inputs for calculation (lower left), and .tiff file (right). 145

List of Tables

1.1 CubeSat thermal control challenges (inspired by [2]). 4

2.1 Summary of sublimator specifications and features from 1960s-present. 15

3.1 Summary of CubeSat sublimator specifications. 35
3.2 Comparison of thermal cooling systems. 35

4.1 Knudsen Number and flow regimes [83]. 64
4.2 Percentage reduction in pressure-driven nature of flow due to water vapor pressure. 71
4.3 Pressure drop and permeability values for porous media samples of varying pore size and porosity at $T = 0°C$. 74

5.1 Hardware Characterization & Experiment Goals 84
5.2 Description of Porous Medium Hardware from manufacturers [72, 75]. 85
5.3 X-Ray CT scanner configuration [105]. 85
5.4 Comparison of Manufacturer & Computed Specifications for Sample Discs. . . . 87
5.5 Description of pressure, temperature, and mass sensors used in experiment. . . . 94
5.6 Compressibility Factor and Joule-Thomson Coefficient for supreheated water vapor in experiment [18]. 99
5.7 Temperature - pressure - enthalpy comparison for ideal gas and superheated water vapor in experiment. 107
5.8 Difference in ΔP in the beginning versus end of trials. 110
5.9 Mass flow rate data. 114
5.10 Extra mass of water utilized during transient period. 116
5.11 Experimental Data of $\frac{\dot{m}}{\Delta P}$ 117

6.1 Compressibility Factor and Joule-Thomson Coefficient for near-saturation water vapor in experiment [18]. 121
6.2 Pore Size data for RMSE calculation. 122
6.3 Historical data and Weber equation. 126

A.1 PuMA Results 146

List of Acronyms

CIS	Contaminant-Insensitive Sublimator
CMGI	Center for Molecular and Genomic Imaging
CNSA	Chinese National Space Administration
CSFR	Center for Spaceflight Research
CT	Computed Tomography
DGM	Dusty Gas Model
DMM	Digital Multimeter
DSMC	Direct Simulation Monte Carlo
ECLSS	Environmental Control and Life Support System
EMU	Extravehicular Activity Mobility Unit
EVA	Extravehicular Activity
GSFC	Goddard Space Flight Center
HRVIP	Human, Robotics, Vehicle Integration and Performance Lab
IR	Infrared
LEO	Low Earth Orbit
MSD	Mean-squared displacement
MFP	Mean Free Path
PLSS	Portable Life Support System
PRT	Platinum Resistance Thermometer
ROI	Region of Interest
RTD	Resistance Thermometer Detector
SDC	Sublimator-Driven Cold plate
TCS	Thermal Control System

Nomenclature

A	Area	m^2
Bi	Biot number	–
D	Diffusion coefficient	m^2/s
d	Pore diameter	m
d_{H_2O}	Molecular diameter of water	$2.65 * 10^{-10}\ m$
E	Energy	J
Fo	Fourier number	–
h	Convective heat transfer coefficient	W/m^2C
h_{lv},h_{sv}	Enthalpy of vaporization/sublimation	J/kg
k	Thermal conductivity	W/m^2C
k_B	Boltzmann Constant	$1.38 * 10^{-23}\ m^2kg/s^2K$
Kn	Knudsen number	–
l	Length (or thickness)	m
M_{H_2O}	Molar mass of water	$0.018015\ kg/mol$
$\dot{m}$	Mass flow rate	kg/s
p_1	Experiment inlet pressure	Pa
p_2, p_{exit}	Experiment Outlet/exit pressure	Pa
Q"	Volumetric flow rate per area (flux)	$m^3/s/m^2,\ m/s$
q	Applied heat (thermal energy)	W
q"	Heat flux	W/m^2
R	Universal gas constant	$8.3145\ J/molK$
r	Pore radius	m
T_{base}	Temperature of heat source	$^\circ C$
t	Time	s
U	Unit of volume for a CubeSat	$10cm\ *\ 10cm\ *\ 10cm$
u_t	Internal energy	J
v	Specific volume	m^3/kg
v	Flow rate	m/s
$\dot{W}$	Work	J

α	Sticking coefficient	–
α	Thermal diffusivity	m^2/s
$\mathcal{K}$	Permeability coefficient	m^2
λ	Mean free path	m
μ	Dynamic viscosity	$Pa-s$
ρ	Density	kg/m^3
τ	Tortuosity	–
ϕ	Porosity	%

Subscripts

Al	Aluminum
eff	Effective
FW	Feedwater
g	Generated
ice	Ice
ls	Liquid/solid interface (freezing)
PM	Porous media
ref	Reference
sat	Saturation
ss	Stainless steel
sv	Solid/vapor interface (sublimation)
tp	Triple point
vap	Vapor
Al, FW	Aluminum/feedwater gap interface
FW, PM	Feedwater gap/porous media interface
PM, ice	Porous media with ice
PM, vap	Porous media with water vapor

Acknowledgments

This thesis would not be possible without the constant support and encouragement of those in my life I am lucky enough to call my friends, family, mentors, and colleagues. Thank you Professor Robinson, I could not have asked for a better mentor and advisor. The questions you asked during our research meetings guided me through the *tortuous* world of sublimators and helped me gain a better intuition for which out-of-the-box research ideas are worth exploring. Thank you for your care, not just toward my research adventures but toward my life adventures too. Thank you, Dr. Gene Ungar, I greatly appreciate your "sublimator intuition", decades of experience, and positive attitude. You helped me see the forest through the trees...or the sublimator through the pores. Prof. Narayanan, your liquid-vapor phase change phenomena class was my introduction to phase change heat transfer in an academic setting and I am grateful for your support on my thesis committee. Thank you, Professor Baughn, for our hours-long weekly discussions over coffee. Our discussions ranged from heat transfer and thermodynamics to aviation, outdoor adventures, cooking, and religion. The questions you asked me via the Socratic method pushed my research in directions I didn't know it could go. And I will think of you every time I cook hard-boiled eggs.

I am indebted to all of the folks I have worked with on this research: Dr. Doug Rowland from the UC Davis Center for Genomic and Molecular Imaging for helping me take the X-ray CT scans and teaching me how to use Dragonfly. I thoroughly enjoyed working with you and discussing the overlap between spacecraft engineering and veterinary research. Thanks to all the folks at NASA Johnson Space Center in EC2 and EC6, especially Dr. Tom Leimkuehler and Hee Jong Song. Our discussions about sublimators - past, present, and future - helped push my research in the right direction. Thank you to all the folks at NASA Goddard Space Flight Center in Code 545, especially Frank Robinson in the T2D2 lab. I could not have completed my experiment without you! During the long days in the lab, you taught me so much about vacuum chamber operations, testing, propagation of error, data analysis, and experimental set-up in general. Thank you to Dr. Joseph Ferguson, one of the PuMA creators, whose conversations provided us with invaluable guidance.

Mom, dad, and Lisa: thank you for your endless love and support and for listening to hours of explanations about my research. Thank you for creating opportunities for me to pursue my dreams! Hannah and Rachel, spending time with you was the recharge I always needed. Thank you to my dear friends: whether you live half-way around the world, in another state, or in the same apartment, you gave me the strength to keep going when research felt insurmountable. Thank you to Peyton Hilford whose undergraduate research supported this thesis, it was always a pleasure to work with you and hear your physics-based perspective. A huge thank you to my fellow HRVIPers with whom I spent most of my waking hours. Thanks for helping me navigate graduate school, for being my research sounding board, and for reading and re-reading papers and important emails. Thank you for the endless laughs, puns, memes, and for making me your sublimation queen. Carl, you took the brunt of my lows even when we weren't in the same city to experience the highs together. Thank you for always believing in me, especially when I didn't believe in myself. Last, but not least...Levi and Myla, being your auntie has brought me endless joy! May your dreams be great and your determination be even greater.

Abstract

Sublimation Cooling for CubeSat Waste Heat Rejection

Small, inexpensive satellites called CubeSats are commonly used for conducting academic and commercial space research. Typically, there is not a robust thermal control system to dissipate heat from the CubeSat avionics or payloads, which limits onboard computing power and mission capabilities. This research proposes the use of a sublimator to reject waste heat from a CubeSat to enable more powerful computers to be flown along with payloads that require significant thermal cooling. During the sublimation process, the phase-change of ice to water vapor, heat is transferred away from the spacecraft and into the vacuum of space. In a water sublimator, liquid water from a supply line freezes within a porous component and sublimates to water vapor upon exposure to the vacuum of space. The CubeSat's waste heat is channeled into the sublimator and transferred out of the spacecraft via the sublimation process through the porous component. The heat dissipation rate is determined by the sublimation rate, which depends on the mass flow rate of the water vapor released into space. The mass flow rate is limited by the physical properties of the porous component, and passively controlled by the amount of thermal energy available to cause the water ice to sublimate into vapor.

Even though sublimators have been used as spacecraft cooling technology for decades, they have not been used for CubeSat thermal control and the heat transfer and thermodynamic mechanisms in the sublimator are still not fully understood. The focus of this research is threefold. First, the design process for sizing a sublimator based on mission requirements and integrating it with a CubeSat thermal control system is explored. Second, a model is developed to examine the driving factors in sublimator performance. Most notably, this model incorporates both the conductive heat transfer through the sublimator, expressed as a thermal resistance network, and the rarefied water vapor diffusion through the porous component, expressed using the "Weber equation" to analytically model vapor behavior in multiple flow regimes. The resulting temperatures obtained from the thermal resistance network inform the parameters for the analytical Weber equation.

Lastly, an experiment is conducted specifically to validate the model for rarefied water vapor diffusion through a porous medium. The most notable result is the use of experimental data to validate the relationship between heat rejection, mass flow rate and pressure drop in the porous medium. These validated results are then used to inform sublimator design choices such as pore size and porosity. Throughout this thesis, shortcomings from literature are addressed, as are knowledge gaps from this current research to help identify future research directions. This thesis utilizes the sublimator model and experiment validation, combined with overall CubeSat and thermal control systems knowledge, to relate high-level mission requirements to detailed sublimator design choices.

Chapter 1

Introduction

1.1 Overview

The work presented in this thesis is a product of the project named Ice Sublimation Cooling for Heat REjection Amid Microgravity, or I-SCHREAM (pronounced *ice cream*). This research took place at the University of California, Davis' Center for Spaceflight Research (CSFR). One of the labs in the CSFR is the Human, Robotics, Vehicle Integration and Performance (HRVIP) Lab and in HRVIP, student researchers develop enabling technology to make human spaceflight safer and to make scientific missions more accessible to university researchers. Both types of missions may be accomplished or aided with the use of small, relatively inexpensive satellites called CubeSats. Presently, HRVIP is developing a number of new technologies for CubeSat proximity operations (e.g. an Inspection CubeSat flying close to the International Space Station to inspect a potential external anomaly). One of these technologies, and the focus of this thesis, is thermal cooling for CubeSats via sublimation for waste heat rejection, inspired by the sublimators on the current NASA spacesuits.

Sublimators are a small-volume, passive thermal control technology with proven flight history which may allow CubeSats to fly more powerful computers or processors and conduct more complex experiments, as described in detail in Section 1.3. During sublimation of ice to water vapor, significant thermal energy is transferred from a heat source into the vacuum of space due to water's high latent heat. Although sublimators utilize water, a consumable, their size and passive nature is especially appropriate for CubeSat missions with volume

constraints and short mission durations.

In a sublimator, liquid water from a supply line freezes in a porous component. This ice is exposed to a vacuum and sublimates to water vapor, transferring waste heat from the energy-consuming electronic components into the vacuum of space via phase change heat transfer. The porous component passively regulates the sublimation rate and electronics heat rejection by providing a resistance to water (and water vapor) flow exiting the sublimator. Many sublimators utilize a coolant loop to convectively transfer heat from the source to the sublimator, but this research focuses specifically on sublimator behavior, not on the coolant loop.

The goals of this sublimator research are fourfold:

1. Introduce a CubeSat thermal control system (TCS) and example missions in which sublimators may be advantageous.

2. Mathematically describe the heat and mass transfer mechanisms in a sublimator.

3. Validate the mathematical model with a rarefied vapor diffusion experiment.

4. Relate the big-picture mission requirements to the low-level design choices in a sublimator.

This thesis is organized as follows: Chapter 1 provides background information on how sublimators work and why they could be beneficial for CubeSats; Chapter 2 gives a literature review of sublimator usage over the decades; and Chapter 3 discusses how a CubeSat thermal control system could be configured with a sublimator and steps through the process for sizing a sublimator based on mission requirements. Next, Chapter 4 explains the model used to describe the heat and mass transfer through the sublimator and Chapter 5 discusses both the hardware and experiment used to validate the model and learn more about the porous component itself. Chapter 6 describes how the model was validated with the experiment and finally Chapter 7 concludes the thesis and discusses future work.

1.2 CubeSat Thermal Control

In the next five years, there are projected to be over 2,000 CubeSats launched by governments, universities, and commercial companies [1]. All spacecraft, including CubeSats, generate waste heat which is defined as all electrical power produced by the spacecraft that is not converted to energy such as radiowaves (data). Traditional thermal control technologies used on larger spacecraft may be modified and scaled down for some CubeSat applications [2], but often there is little to no thermal control for rejecting heat generated from electronics onboard a CubeSat. Historically, there has not been a need for active or phase-change heat dissipation technology onboard CubeSats because mission requirements often cap hardware operating temperatures and the avionics/payloads do not generate enough heat to surpass these temperature limits. For example, NASA's CHOMPTT (CubeSat Handling of Multisystem Precision Time Transfer) was designed specifically with a power-limited platform, which avoids the need for active thermal control [3]. The measured on-orbit temperatures were between $-10°C$ and $50°C$ without an active thermal cooling system (see Figure 1.1) [4].

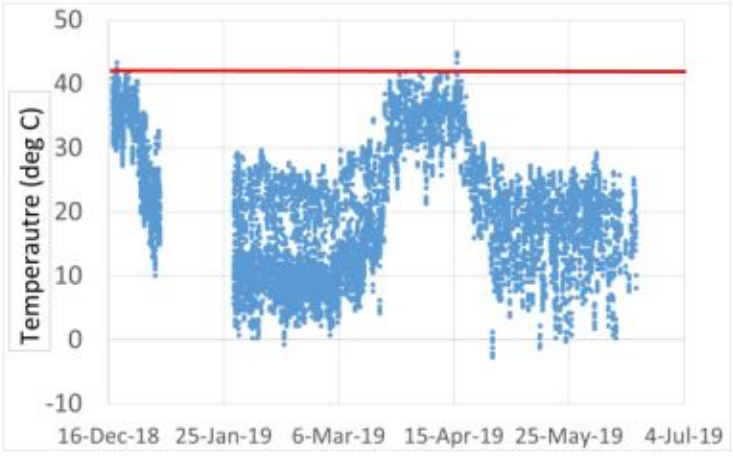

Figure 1.1: NASA CHOMPTT (2018) on-orbit temperature data (blue) and steady-state high temperature predictions (red) [4].

This begs the question, *is heat rejection technology rarely emphasized because there is not a need for it, or are CubeSats designed around the assumption that there is not an efficient method of rejecting large amounts of waste heat?* Perhaps the *need* for more effective CubeSat thermal cooling does not exist because there have been few attempts to find a heat rejection

solution. Table 1.1 summarizes the challenges to developing a CubeSat-scale thermal control system [2].

Table 1.1: CubeSat thermal control challenges (inspired by [2]).

CubeSat Property	Challenge
Low thermal mass	The spacecraft is more reactive to changing thermal environments.
Limited external surface area	External real estate is often allocated to solar cells, leaving little to no surface area for thermal coatings or radiator attachments.
Limited volume	There is less space for electronic components, science instruments, and thermal control hardware.
Limited power	There is less power available for active thermal control technology.
Limited attitude control	If CubeSats have an attitude control system, it is often used for payload pointing requirements and not for meeting thermal requirements.
Highly variable environment	Most CubeSats in LEO are subject to many thermal cycles over their lifetime.
Integrated electronics	Electronics (heat sources) in close proximity are thermally coupled in the small CubeSat volume.
Commercial off-the-shelf components	Low-budget CubeSat missions utilize commercial off-the-shelf components, which often have narrower temperature operating ranges if they are not specifically rated for a space environment.

The three cases in which active thermal control is especially useful are examined in more detail.

High-powered payload: The small form factor of CubeSats, increasingly powerful payloads, and large energy densities contribute to the generation of more thermal energy (waste heat) which must be rejected. Present-day small satellites may have spacecraft busses and payloads which generate 10W during nominal operations and up to 100W during high powered operations [2, 5–7]. Fennel describes the development of a 6U CubeSat (1U is a 10cm x 10cm x 10cm volumetric unit) with an additive manufacturing payload that generates 135W of waste heat and utilizes radiators, thermal coatings, and phase change material to maintain a temperature between $-40°C$ and $75°C$ [7]. Butler-Craig describes a 3U CubeSat with a power-dense system for high-impulse electric propulsion capabilities [5]. This CubeSat generates 100W of waste heat and utilizes an aluminum block heat sink with a $70°C$ limit which

radiates waste heat to the environment.

Specific pointing requirements: The UC Davis HRVIP lab is developing an inspection CubeSat which will perform an external inspection of high-value human-rated spacecraft prior to extravehicular activities (EVAs). This CubeSat may be subject to increased radiative heat loads if its surfaces are simultaneously exposed to the Sun, Earth, and a large spacecraft. It also has pointing requirements specific to its mission, so a radiator which must be pointed away from environmental heat sources is poorly suited for this inspector class of CubeSats. The NASA Johnson Space Center Seeker CubeSat is another inspection CubeSat with specific pointing requirements [8]. The National Oceanic and Atmospheric Administration (NOAA) Earth Observing Nanosatellite—Infrared (EON-IR) is a 12U CubeSat with a precision-pointing requirement and high power-generating payload [9]. These examples demonstrate an increasing demand for spacecraft with pointing profiles that may benefit from hardware other than a radiator for their TCS.

Highly sensitive payloads: CubeSats with biological experiments or electro-optical instruments for Earth observation or astronomy need to be maintained at very cold temperatures in low-Earth orbit (LEO), which will require an active heat rejection system. For example, the Thermosphere Ionosphere Mesophere Energetics Dynamics (TIMED) mission requires active thermal control to keep its instruments cool [6]. Another example is the BioSentinel CubeSat with a live yeast payload or the EcAMSat with an *E.coli* payload (among a number of other similar CubeSats with biological experiments) [10]. These biological experiments did not necessarily need to be maintained at below-freezing temperatures, but an active thermal control system may help the CubeSat maintain the appropriate thermal environment for the experiment.

Performance of a thermal cooling system is often measured in energy (waste heat) rejection per unit mass or volume of the TCS (J/kg or J/m^3). While this sublimator research has not yet progressed enough to compare its performance to other CubeSat cooling technologies, this type of metric should be applied to future developments of this technology.

There are a number of recent projects that explore thermal control solutions for CubeSats, such as miniature cryocoolers and other active thermal control technologies [9]. One notable example is the Active CryoCubeSat research (ACCS) whose goal was to demonstrate a thermal cooling system with a small form factor and low-power budget [6]. None of the known cooling systems applied to CubeSats have included a sublimation approach. The specific requirements for cooling technology are discussed more in Section 3.2.

1.3 Overview of a Sublimator

A sublimator is a small-volume and self-regulating thermal control technology, suitable for heat rejection in a vacuum. Sublimators are so named because their operation includes a phase change of ice to water vapor which occurs below the triple point of water ($T = 0.01°C$ and $p = 611.6\ Pa$) identified in Figure 1.2.

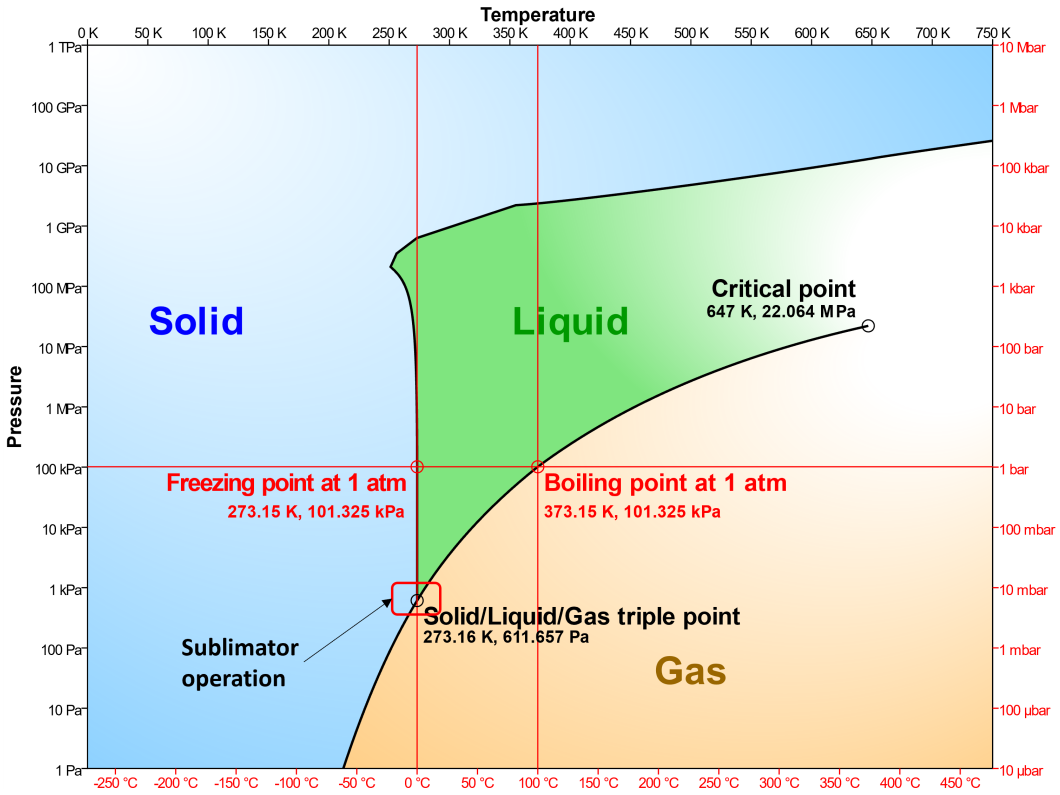

Figure 1.2: Phase diagram of water with the triple point pressure/temperature indicated [11]. Note that at pressures above the critical point, the relationship between ice and liquid water is unusual and counter-intuitive [12].

During sublimation of ice to water vapor, latent heat is transferred from a heat source to the ice as it sublimates into the vacuum of space. Water's high latent heat, or enthalpy of vaporization ($h_{lv} = 2500\ kJ/kg$ at $0°C$), means that significant waste heat can be rejected via phase change. The use of h_{lv} instead of the enthalpy of sublimation, h_{sv}, is discussed later in this section.

According to literature, in sublimators, liquid water from an on-board reservoir is supplied to and freezes in a porous component as depicted in Figure 1.3 [13–15]. Rather than a single, continuous sheet of ice covering a cross-section of the porous medium during steady-state, there is ice in the pores at a constant depth where the phase change phenomena occurs. The phase-change phenomena is inherently non-equilibrium: as long as the ice is exposed to vacuum or near-vacuum conditions, it will sublimate at the ice-vapor interface within the pores. The heat from spacecraft avionics, electronics, or payload is conductively transferred to the ice-vapor interface and exits the spacecraft via phase-change heat transfer. The porous component serves a number of functions: it provides a conductive path through which the heat load is transferred to the sublimation interface and it passively regulates the sublimation (and thus, heat rejection) rate by adding resistance to water vapor flow exiting the sublimator.

Although sublimators transfer water overboard, their size and passive nature are especially appropriate for CubeSat missions described in Section 3.2. Sublimators can handle a wide range of heat loads while keeping the heat source (e.g. avionics) within an acceptable temperature range because of their self-regulating nature. The more heat flux applied to a sublimator, the greater the sublimation rate.

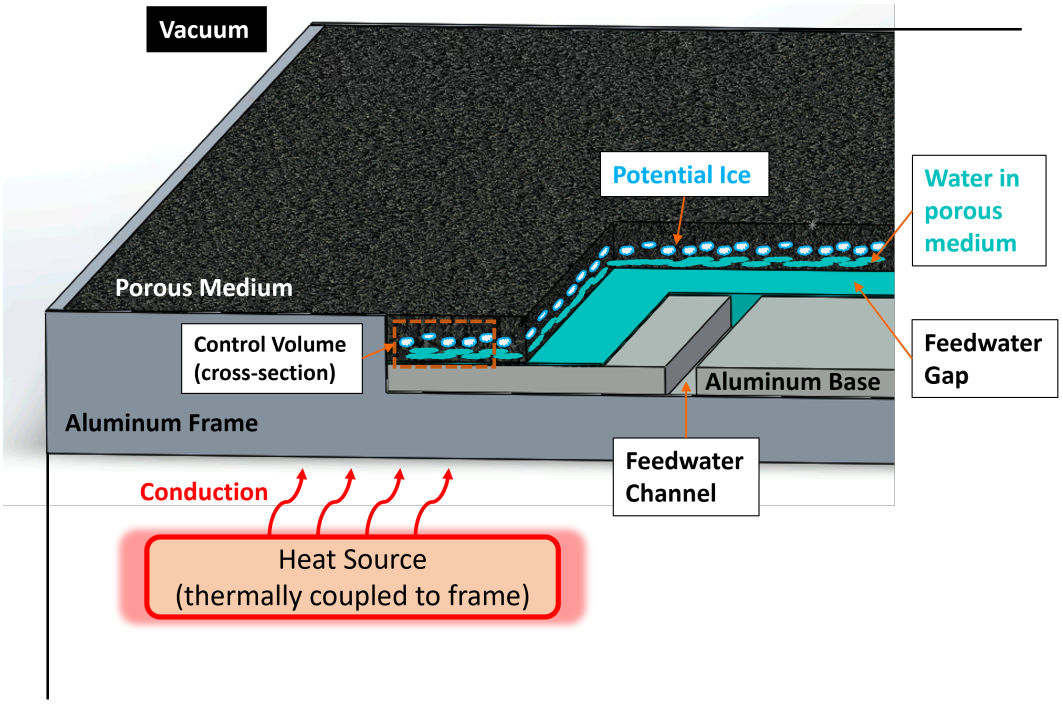

Figure 1.3: Basic components of a sublimator in which heat flux is applied into the bottom of the aluminum frame. Feedwater reservoir and tubes not shown.

A sublimator consists of four main components: the feedwater reservoir and tubes (not shown in Figure 1.3), the thermally conductive frame, the feedwater gap and channel, and the metal porous component. As previously mentioned, the sublimator explored in this research does not include the closed coolant loop; only the sacrificial water utilized during sublimation. Water, which is not actively temperature controlled but is typically $4-32°C$, is self-contained on the spacecraft in a feedwater reservoir (e.g. flexible bladder) and pressurized to approximately 7-10 kPa [16]. The low-conductivity metal porous component (usually stainless steel or nickel) is positioned directly "on top" of the feedwater gap so that one side is exposed to vacuum. There have been efforts from a manufacturing and design perspective to minimize the feedwater gap to $< 2mm$ because this distance contributes the largest thermal resistance to the system. The porous component is usually 1.5mm - 3mm thick: that is all that is needed for the sublimation process. It is typically of low porosity (5-15% void space) with micron-scale pore sizes, which yield a water mass flux proportional to the heat load and available surface area from which ice can sublimate [16]. Before the thermal energy is transferred to the phase-change interface, most of the conductive heat transfer

occurs through the metal substrate, rather than through the water in the porous volume, because the thermal conductivity of metal such as stainless steel ($k_{SS,316} = 16.3\ W/mK$) is higher than that of water ($k_{H_2O} = 0.55\ W/mK$) [17, 18]. A high-porosity medium would reduce the conductive heat transfer through the metal porous microstructure, and thus limit the overall heat transfer capabilities. It is believed that the amount of ice in the porous component is a small fraction of its overall cross-sectional area, the majority of which is metal surrounding the ice. Some sublimators with large porous surface areas also have a grate to secure the thin porous component and prevent it from bowing out due to feedwater pressure, such as in Figure 1.4. The CubeSat sublimator does not require this grate due to its small surface area.

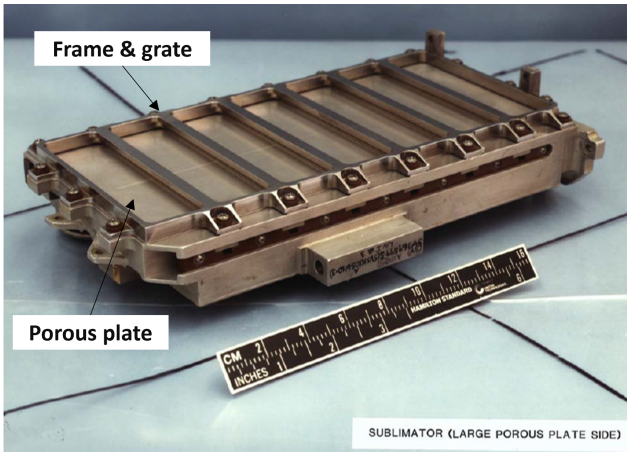

Figure 1.4: NASA EMU sublimator [19].

If evaporation rather than sublimation were to occur, the same amount of heat may be transferred. Leimkuehler describes, "As long as vapor is formed inside the [porous medium], then the thermal energy necessary for the phase change will be drawn from the surrounding material. " [20]. In other words, regardless of the presence of ice, there will always be liquid water entering and water vapor exiting the control volume and the quantity of heat transfer is described by the phase change heat transfer equation, Eq. 1.4. The presence of ice helps to prevent feedwater breakthrough by physically blocking the flow of liquid water, especially if the feedwater pressure were to get too high, but it does not contribute to a greater heat rejection capacity for the sublimator [16]. In the evaporation mode, surface tension alone retrains the water in most cases (there are some instances in the 1960s of a hydrophobic

coating being applied to the porous medium, not the focus of this work) [15, 21].

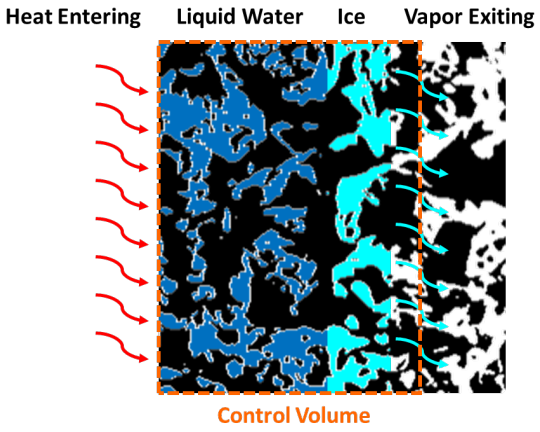

Figure 1.5: Water flow through porous layer for application of the first law of thermodynamics.

1.4 Transient Start-Up

This research is concentrated on steady-state operation and limits the discussion of sublimator transient behavior to a conceptual overview. The sublimator operation is initiated when a valve at the feedwater reservoir opens, allowing water to move through a tube to the vacuum environment of the sublimator assembly. The water enters the assembly through the frame, into the feedwater channel, and spreads through the feedwater gap as shown in Figure 1.3. As soon as the feedwater is exposed to vacuum, it begins to evaporate (and not yet sublimate because the feedwater is still in liquid form), but there is a net feedwater pressure driving the flow toward the vacuum region. The water vapor pressure, both during transient start-up and during steady-state operation, is small compared to the feedwater pressure, as discussed in Section 4.7.1.1 and shown in Table 4.2. The feedwater percolates into the porous component which acts as a retainer via surface tension for the liquid water in the pores.

Within the porous layer, the feedwater is exposed to a pressure below its saturation pressure (p_{sat} is a function of the temperature of the surrounding porous structure). Simultaneously, waste heat from the CubeSat is transferred via conduction through the aluminum frame and feedwater gap and into the porous component. The top "layer" of water initially evaporates, which removes heat from the liquid water immediately "behind" the evaporation

interface. The temperature of the evaporation interface drops and eventually freezes. This creates the ice "layer" within the porous component. In steady-state operation, the water on the upstream side of the ice freezes when it meets the water-ice interface. When thermal energy reaches the ice, it leaves the ice via sublimation, at a rate proportional to the applied heat and latent heat of water. In steady-state, sublimation occurs at the same rate at which water is freezing, forming a self-regulating flow-rate system.

1.5 Derivation of Phase Change Heat Transfer Equation

The relationship between heat transfer and sublimation is derived from the first law of thermodynamics ($\Delta U = q - W$) and the conservation of energy for a control volume as in Figure 1.5 [22, 23]. The control volume in question includes the porous medium, in which there exists a "layer" of liquid water and of ice. Equation 1.1 shows the energy balance of a sublimator by comparing the rate of incoming energy ($\dot{E}_{in}$), generated energy supplied ($\dot{E}_g$), the rate of outgoing energy ($\dot{E}_{out}$) and change in energy stored ($\frac{dE}{dt}$)

$$\left(\dot{E}_{in} + \dot{E}_g\right) - \dot{E}_{out} = \frac{dE}{dt} \tag{1.1}$$

$\dot{E}$ can be in the form of heat entering or exiting the control volume (q), work done by the system ($\dot{W}$), or mass flow into or out of the control volume ($\dot{m}$), among other forms not relevant here (e.g. nuclear, chemical). For the current sublimator system, there is no change in energy stored in the system ($\frac{dE}{dt} = 0$), no energy generated ($\dot{E}_g$=0), no work done by the system ($\dot{W} = 0$), and no energy other than conductive heat transfer entering the system ($\dot{E}_{in} = q$). Thermal energy enters the control volume via conduction (q) and water vapor leaves the control volume, as depicted in Figure 1.5. The first law is reduced to

$$\left(q + \cancel{\dot{E}_g}\right) - \left(\dot{E}_{out} + \cancel{\dot{W}}\right) = \frac{\cancel{dE}}{\cancel{dt}} \quad \rightarrow \quad q = \dot{E}_{out} \tag{1.2}$$

There is no kinetic ($\frac{1}{2}\dot{m}v^2$) or potential ($\dot{m}gz$) energy considered in this system, but internal energy of the system must be accounted for as u_t. In addition, when there is flow across the

boundary of a control volume, *flow work* is defined as a product of the pressure and specific volume of the fluid, pv [24]. Enthalpy/latent heat, the transfer of thermal energy during the phase-change of a substance, is a property defined as $h_{lv} = u_t + pv$. Thus, the supplied heat can be expressed as:

$$q = \dot{m} \left(u_t + pv \right)_{out} \tag{1.3}$$

The energy required for a phase change is the product of the mass flow of the substance, $\dot{m}$ and its enthalpy, h_{lv}, and so the first law of thermodynamics may be rewritten as:

$$q = \dot{m} h_{lv} \tag{1.4}$$

This phase change heat transfer equation captures the heat transfer phenomena in which incoming thermal energy (in this case, supplied via conduction conduction) is transferred via phase change to a mass flow (in this case, water vapor exiting the sublimator). In Equation 1.4, q is the applied heat in W which is equivalent to the rate of thermal energy transfer in J/s, $\dot{m}$ is the mass flow rate in kg/s, and h_{lv} is the enthalpy of vaporization in J/kg. This equation can also be normalized by area so it would read as heat flux in W/m^2 and mass flow rate per area in $kg/s/m^2$. As stated previously, in the case of a sublimator, the enthalpy of vaporization (h_{lv}) is used because it is the net phase change between the exothermic process of freezing (heat of fusion) and the endothermic process of sublimating (enthalpy of sublimation). The first law of thermodynamics can be used to derive the heat transfer equation for sensible heat, or the transfer of thermal energy required to change the temperature of a substance, but the change in internal energy from the sensible heat component is not significant and is much smaller than phase change heat transfer (see Section 5.2.4).

1.6 Advantages & Disadvantages of a Sublimator

A sublimator is advantageous because it passively controls the heat rejection rate. The only power required is to open the feedwater valve when sublimation cooling is first initiated and possibly to pressurize the feedwater reservoir (although this sub-system requires further

research). A sublimator can handle a large variation in heat flux from a heat source while maintaining the heat source within a narrow temperature band. For example, the sublimator on the extravehicular activity (EVA) mobility unit (EMU) performs well with heat loads between 100-600 W and even up to 1000W in some cases [16]. A sublimator also does not require as large a surface area as a radiator. Because of the high latent heat of vaporization of water, a small porous component exposed to vacuum is an effective and efficient heat rejection mechanism. In addition, a sublimator's performance is not orientation dependent, meaning it does not need to face a certain direction, such as away from the sun or toward deep space, to perform as expected.

Historically, there have been a number of anomalies associated with sublimators which will be highlighted in Chapter 2, but many of these issues are not a concern for CubeSat applications. There are two relevant anomalies that have been observed either in testing or on-orbit: feedwater breakthrough and contamination of the porous medium. Feedwater breakthrough, discussed at length in Section 2.2, occurs when the sublimator is not operated within its nominal limits. Contamination of the porous medium over time, also discussed in Section 2.2, occurs when contaminated feedwater is utilized and can eventually lead to some of the causes of feedwater breakthrough. During feedwater breakthrough, liquid water passes completely through the porous layer and freezes on the outer surface of the sublimator, rendering it unusable. The manufacturing of sublimators is one of the most challenging parts of the hardware life cycle: the precision with which welding or brazing of the frame around the porous component is performed can *also* affect feedwater breakthrough via leakage. The main restriction with a sublimator is the use of a consumable (water), which occupies mass and volume. While it would be unrealistic to launch and carry enough water to continuously cool a large-scale spacecraft, a CubeSat with a short-duration mission could have enough volume and mass budget for the feedwater, as demonstrated in Section 3.2.

Chapter 2

Literature Review

This chapter summarizes the 60-year history of sublimator technology, presented in chronologic order, covering four space agencies: NASA, Roscosmos, the European Space Agency (ESA), and the Chinese National Space Administration (CNSA), as well as dozens of sublimator designs, tests, and models. Chang *et al.* also provides a literature review of sublimator technology thus far and emphasizes that, even after 60 years, there is still a limited understanding of the sublimation (or evaporation) mechanism within the porous medium under a vacuum environment [25]. Section 4.2 enumerates the most significant knowledge gaps and shortcomings found from this literature review with an emphasis on the unfounded assumptions from the sublimator models.

Table 2.1 summarizes the key specifications and notable features for each sublimator discussed for ease of reference. Almost all of the sublimators which have been used in the past are integrated with a larger thermal control system which includes a coolant loop to bring waste heat from all parts of the spacecraft/spacesuit to the sublimator. A CubeSat sublimator TCS would not incorporate a coolant loop, typically used when the heat source(s) and heat sink are positioned far apart from each other in the spacecraft. As such, this literature review does not focus on the design or performance of coolant loops.

Table 2.1: Summary of sublimator specifications and features from 1960s-present.

Name [references]	Year/ Program	Manuf.	Mission Description	Mission Requirements	Status	Dry Mass	Heat Rejection Range	Feedwater Utilization	Specific Heat Rejection	Notable Features
Lunar EMU [15, 24, 25, 27, 29, 31]	Apollo	NASA	Lunar EVAs	Cool crewmember for 8.5 hours	Model, ground test, flight	2.75 kg	100-800W	0.67 kg/hr*	0.29 kW/kg	First sublimator designed and used in flight.
EMU [16, 17, 36]	1980s-current (Shuttle/ISS)	NASA/ Hamilton Sundstrand	ISS EVAs	Cool crewmember for 8.5 hours	Model, ground test, flight	1.57 kg	100-800 W	0.475 kg/hr	0.5 kW/kg	Most used and studied sublimator. Typical operation is at 300 W.
Orlan-M [37, 38]	1980s-current	Roscosmos/ Zvezda	ISS EVAs	Cool crewmember for 8.5 hours	Model, ground test, flight	--	80-950W	0.43 kg/hr	--	Similar to Shuttle/ISS EMU. Dry mass and porous media surface area data were not available.
X-38 [14, 40]	1990s	NASA/ Hamilton Sundstrand	Space plane for crew re-entry	Cool 6 crew for 8.5 hrs on-orbit, 30 min in atmosphere	Model, ground test, first flight (cancelled)	9.3 kg	300-1,025 W	--	1.04 kW/kg	Modeled after Lunar Module sublimator. Heat fins in feedwater gap enhance conduction to porous component.
Contaminant Insensitive Sublimator (CIS) [18, 35]	2000s Constellation	NASA/Jacobs	Crew exploration vehicle with 180 day dormancy	Not specified	Model, ground test	--	6000 W**	15.3 kg/hr**	0.93 kW/kg	Small pores for traditional sublimator use and large pores to prevent contaminant clogging. Unclear if CIS utilization can be stopped/restarted.
Sublimator Driven Coldplate (SDC) [43-45]	2000s Constellation	NASA	Altair Lunar Ascent Module & other applications	6.5 hour usage	Model, ground test	3.5 kg***	< 3100 W	3.6 kg/hr	1 kW/kg	Modeled after the X-38 sublimator. Eliminated the pumped cooling loop for mass and volume savings. Inspiraiton for the CubeSat sublimator.
Chang'E-5 [13, 23, 47]	2010s-present	CNSA	Lunar lander & Ascent stage	13.1 hours for one sublimator and 7.56 hours for the other.	Model, ground test, flight	<10 kg	400 W	0.25 kg/hr	0.04 kW/kg	"Hot start" capabilities (start-up at 40C). Two identical sublimators on TCS can operate independently or in sync.

*From ground testing
** Unrealized goal
***Excludes integrated avionics

2.1 1960s-1970s

The first official record of sublimator development is a 1965 patent for the Porous Plate Sublimator, different versions of which were used on the Saturn 1B second stage, Saturn V third stage, Apollo lunar space suits, and the Lunar Module [26–30]. On the Saturn rockets and lunar spacecraft, the sublimator provided supplemental heat rejection capabilities during mission phases with peak heat loads from the spacecraft, inspiring future spacecraft such as the X-38 and Chang'E-5 to do the same. Figure 2.1 shows the Apollo EMU Portable Life Support System (PLSS) with the sublimator positioned on top. A sublimator was also used for heat rejection for the Environmental Control and Life Support System (ECLSS) on the lunar module. The 1960s and 1970s also saw the first sublimator models which set the stage for future modeling efforts, including this research. The sublimator conduction model was coupled with the phase change heat transfer equation 1.4 and the porous medium was treated as a bundle of capillary tubes with a simplified treatment of vapor flow which is expanded upon in Chapter 4 [15, 31].

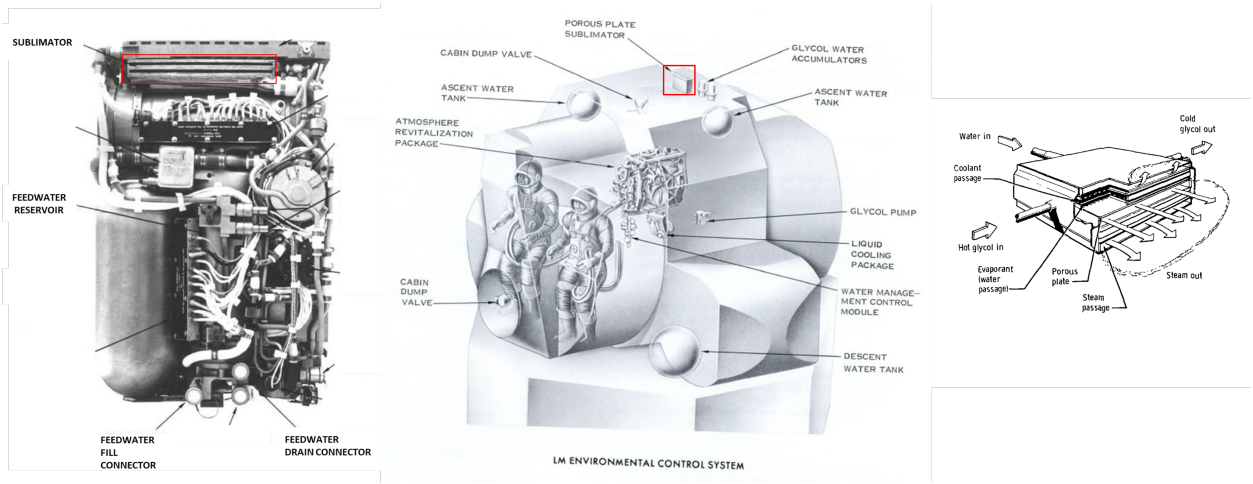

Figure 2.1: The Apollo spacesuit PLSS, left [32] and the Apollo Lunar Module, center/right [33, 34].

There are several disadvantages to the Apollo-era spacesuit sublimators compared to that of the current EMU sublimators. First, the stainless steel assembly and nickel porous component were relatively heavy. The total Apollo suit sublimator assembly mass was 2.75 kg (6.08 lbs) [35], compared to the current NASA EMU aluminum frame and stainless steel

porous component mass of 1.58kg (3.48 lbs) [16, 35]. Second, the Apollo-era brazing process during assembly created a relatively large feedwater gap compared to that of the EMU, leading to a long shut-down time because of the need to sublimate the remaining water in the feedwater gap (30 minutes compared to the current EMU's 30 seconds) [16]. Third, the brazing process required the replacement of the entire Apollo sublimator assembly when the porous component needed to be refurbished because it alone could not be removed [16]. In the early 1970s, Hamilton Sundstrand developed an updated sublimator design with several new features, most notably a replacable porous plate (nickel), a decreased feedwater gap thickness, and an aluminum frame for lower weight [16]. Most of this design remained the same into the 1980s with the development of the current NASA EMU sublimator. Despite the disadvantages of the Apollo-era sublimator identified in retrospect, the sublimators proved to be successful in both ground testing and flight: they were reliable, passive, and ideal for short-duration utilization.

2.2 1980s-1990s

NASA Shuttle/ISS EMU

The most well-known use of a sublimator today is on the current spacesuits to cool crewmembers during EVAs, seen in Figure 2.2. Despite the differences in environment between the Apollo lunar missions and the more recent low-earth orbit missions, sublimators have performed well in both environments. There are a number of relatively recent improvements to the sublimator compared to the Apollo design and the early EMU design which have led to a weight reduction and increased heat flux: the replacement of stainless steel structural parts with aluminum (i.e. the frame and grate to secure the porous component) and the replacement of the nickel porous component with one of stainless steel. The arrangement of the current EMU sublimator is similar to that of the Apollo-era (feedwater reservoir, feedwater gap, porous component) and has an expected operating life of 40 years with the porous component requiring service or replacement every 35 EVAs (approximately 280 hours) [19]. The NASA EMU Requirements Evolution (2005) [16] points out, "the thermodynamic processes that occur within the sublimator have never been the subject of a

concerted research program, but much information can be deduced from the varied component testing which has been accomplished through the life of the program" which, once again, demonstrates the surprising success of the sublimator despite its mystery.

The current EMU can reject about 300 W nominally and up to double that during peak metabolic loads [36]. It requires 3.8 kg of feedwater for an 8-hour EVA [35]. The feedwater temperature is not actively controlled but the feedwater bladder remains between approximately $4 - 32°C$ inside the PLSS [16]. This is a large feedwater temperature range which may impact performance and is addressed in Section 4.4. The porous component is stainless steel comprised of a compressed series of screens, not sintered metal, as utilized in later sublimators. The inner and outer sections of the porous component have a 7% porosity, a more open structure of unspecified porosity in the center, and a pore diameter of 3-6 microns [16].

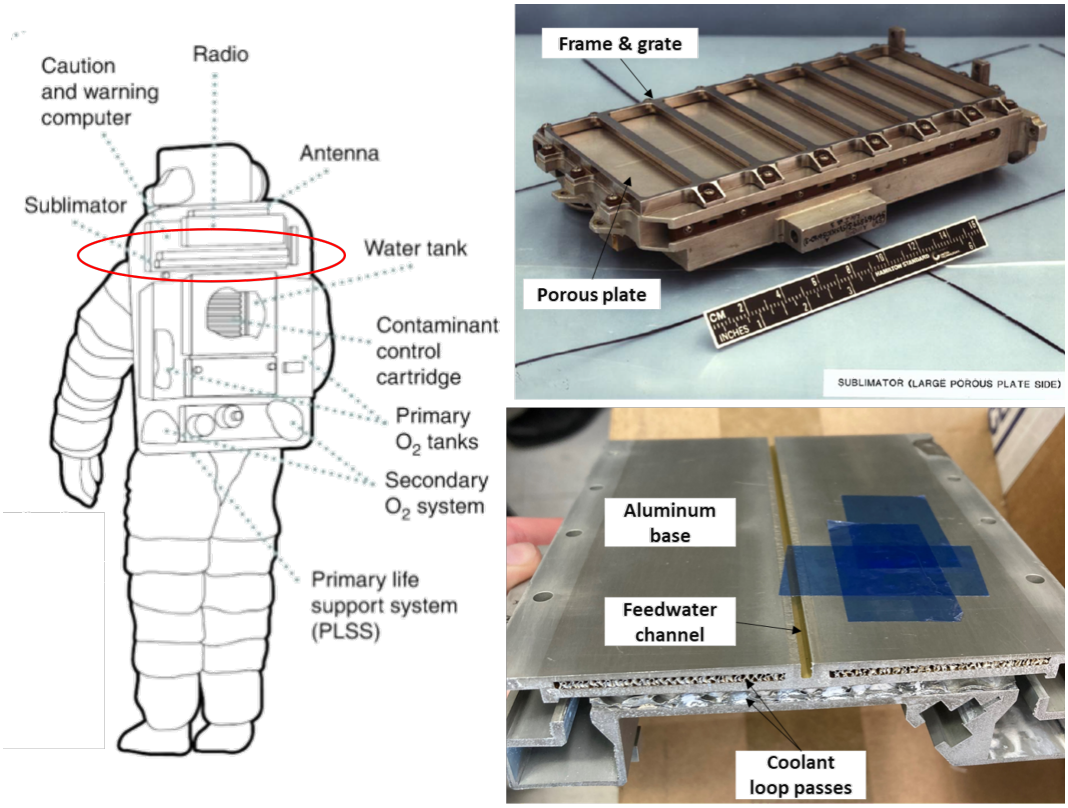

Figure 2.2: NASA EMU sublimator [16, 19]. The bottom right image shows the sublimator stack without the porous plate or frame (blue tape is not for flight). Author credit.

There have been a number of anomalies associated with the EMU sublimators, some of

which were also observed on the Apollo-era and X-38 sublimators. Some anomalies have been observed in testing and others have occurred on-orbit. Feedwater breakthrough is "unchecked flow of water through the porous plate" [16] which freezes on the vacuum-side surface of the porous component, rendering the sublimator unusable, as seen during a ground test in Figure 2.3.

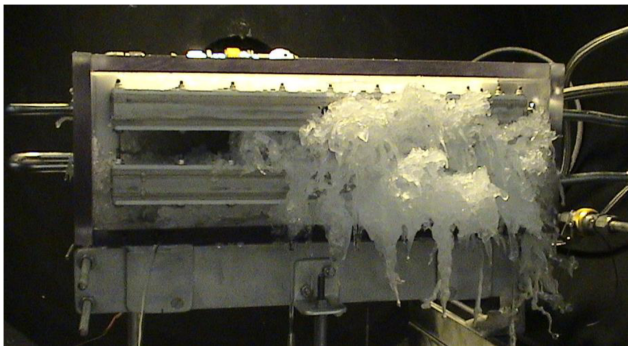

Figure 2.3: Feedwater breakthrough during ground testing on an unspecified sublimator design at Johnson Space Center (year unknown) [37].

Historically, the main causes of feedwater breakthrough are:

1. The feedwater pressure is too high in the reservoir and forces the liquid water through the porous plate without changing phase. Feedwater pressure is measured with a sensor; even if the feedwater pressure was known to be too high, there was no mitigation option other than shutting off the sublimator altogether.

2. The heat flux into the sublimator is higher than its operating limits, often spatially localized (not occurring uniformly throughout the entire porous component volume). This anomaly is generally associated with transient sublimator start-up when feedwater first begins to flow [19].

3. Feedwater leaks out through the interfaces between the porous component and the frame. This water may freeze and expand, potentially damaging the sublimator assembly hardware. This anomaly can be mitigated with manufacturing improvements.

The other most common anomaly is when the porous component gets clogged with particulates and reduces its heat rejection capacity. In the 1980s EMU sublimator usage, the porous component was clogged when residue from the feedwater bladder material and/or

the feedwater itself was left over after sublimation and blocked the micron-size pores [16, 38]. This anomaly required an extensive investigation in the 1980s because it caused the sublimator performance to degrade after just three EVAs instead of the expected 35 EVAs [16]. The initial solution was to add a second, smaller sublimator to supplement the primary sublimator's reduced heat rejection capabilities. A few years later, this anomaly was resolved, a new feedwater bladder material was chosen, and the secondary sublimator remains in current EMUs.

Roscosmos & European Space Agency (ESA)

The development of the sublimator in the USSR/Russia mirrors the development of its American counterpart. Roscosmos' SKV moon spacesuit (an acronym for the Russian term for EVA) utilized a water evaporator as a heat exchanger in the early 1960s, which was later updated to a sublimator in the late 1960s on the Yastreb orbital spacesuit and Kretchet lunar spacesuit [39]. Zvezda, a space technology company in the former USSR, developed the Orlan spacesuit, a more advanced iteration of the Yastreb from the same time period as Apollo. The sublimator on the Orlan handles thermal loads up to 600W, shown in Figure 2.4.

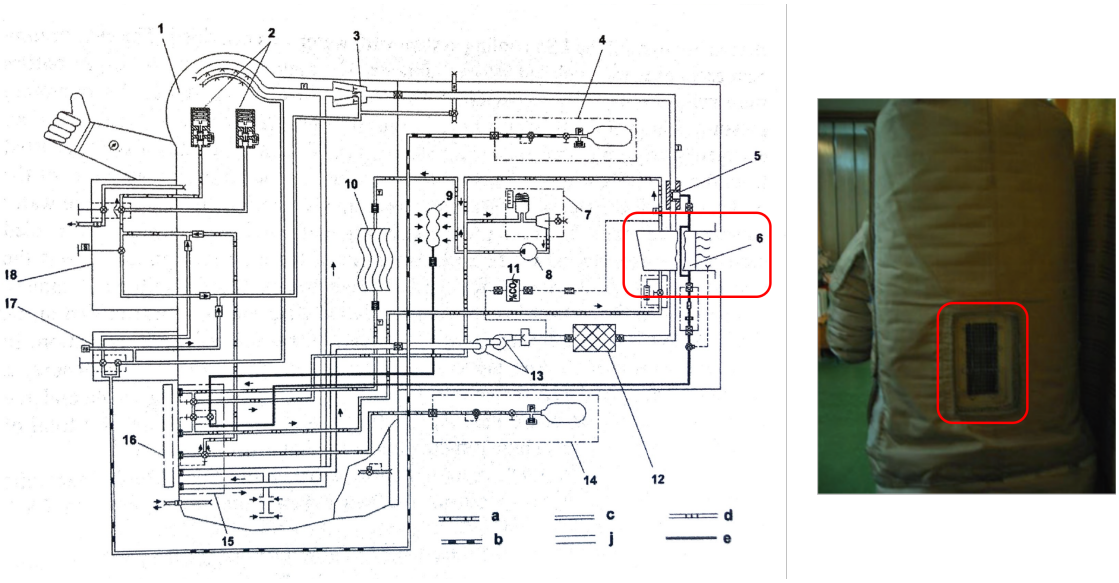

Figure 2.4: Schematic of the Orlan with the sublimator indicated in red box, left [39], and the sublimator vent in Kretchet PLSS (the Orlan's predecessor), right [40].

The Orlan is currently used by cosmonauts and particular attention should be paid to these sublimator improvements [39]:

- A maintenance/cleaning procedure was developed to extend the life of the feedwater loop which was prone to contaminants.
- The feedwater reservoir was lined with a fluoroplastic film and the reservoir outlets from a PVC tube to prevent contaminants commonly seen with metal parts.
- The sublimator housing was made of an aluminum alloy with an undisclosed "special coating", similar to those from NASA and later CNSA.
- The feedwater reservoir was made to be easily disconnected and replaced in case of contamination.
- Installation of a quick-disconnect filter between the feedwater reservoir and the sublimator to extend the operating life of the porous component.

Sublimators are found on two spacesuits from Europe, inspired by the USSR and USA: the first was for a crewed Hermes spacecraft in the 1980s-1990s and second was for the EVA Suit 2000 (a joint effort between Europe and Russia), seen in Figure 2.5. This sublimator incorporated the same elements as the Apollo and early Shuttle EMU sublimators: a stainless steel frame for the feedwater gap, a porous component from layers of wired mesh rolled together, and nickel fins to enhance heat transfer from the cooling loop to sublimator core [41]. The initial design yielded a lower than expected amount of waste heat removal so the design was modified and proved to be successful in ground tests, although sources did not specify the cause of the reduced performance [39]. Not enough details were found on the European sublimator designs, so they are not included in Table 2.1.

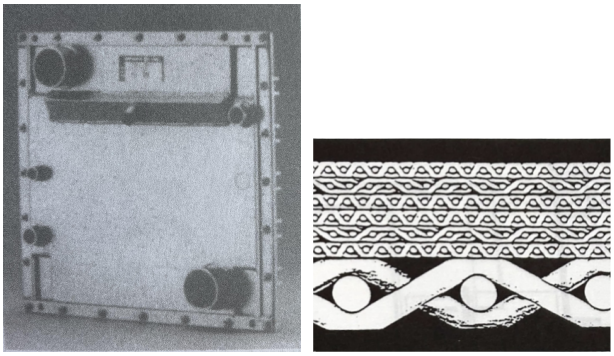

Figure 2.5: The sublimator from the European Space Suit System (ESSS), left [39], and a visualization of porous plate cut-away to show woven wire layers, right [41].

X-38 Space Plane

The X-38 Crew Return Vehicle (CRV) is a space plane developed in the 1990s by Hamilton Sundstrand to be used for crew return from a low-Earth orbiting space station [42]. The X-38 sublimator, shown in Figure 2.6, was designed based on the Lunar Module sublimator with a secondary sublimator which used a refrigerant (in place of feedwater) with a sea-level boiling point to facilitate cooling during the atmospheric phase of the flight [14, 42]. The X-38 sublimator's dry mass is 9.3 kg with an efficiency of 1.04 kW/kg, capable of cooling 6 crewmembers for an 8.5-hour period on-orbit and another 30 minutes within the atmosphere. Its waste heat rejection range is between 293-1025 W. The X-38 sublimator has one notable improvement compared to that of the current EMU design: heat transfer through the feedwater gap is enhanced with metal fins and spot welds [42]. In the early 2000s, a proposed contaminant-insensitive sublimator was modeled for use on the X-38, discussed next [14]. There was a small-scale modeling effort in support of the X-38's updated contaminant-insensitive sublimator which was design-specific and inspired the model in this research [14]. One of the focuses of this model was on the heat transfer from the coolant loop to the porous component layers which is not applicable to a CubeSat sublimator.

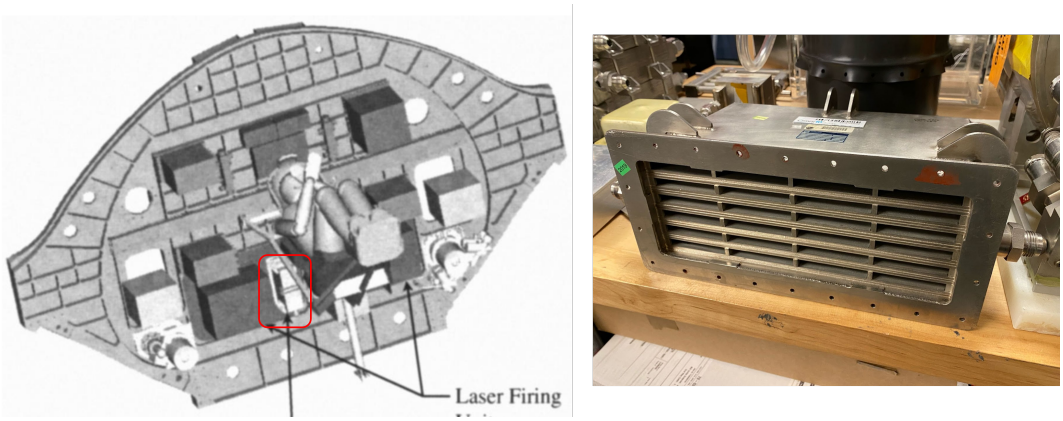

Figure 2.6: X-38 sublimator view from inside crew cabin, left [42], and sublimator hardware at JSC , right (author credit).

2.3 2000s-2010s

Constellation Program

There have been several proposed improvements to sublimators in the 2000s-2010s, the most notable of which are the contaminant insensitive sublimator (CIS) [20, 43] and the sublimator-driven cold plate shown in Figures 2.7 and 2.8, respectively [44–46].

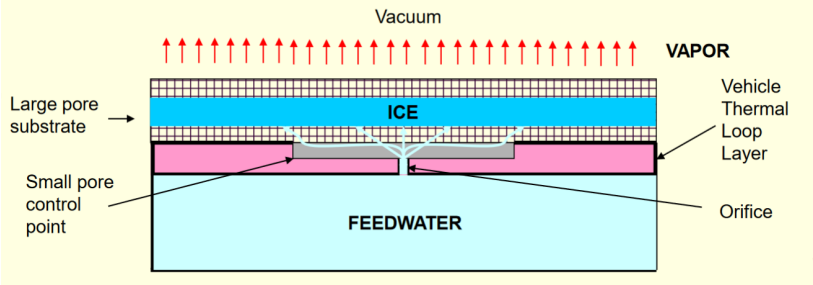

Figure 2.7: Diagram of contaminant-insensitive sublimator (CIS) with the large pores on the vacuum side and small pores on the feedwater side [20].

The CIS was originally designed for a crew exploration vehicle which included a 180-day dormancy while docked to the ISS, making reliability paramount to the sublimator design. The CIS contains two porous components of different pore sizes and porosities which serve different purposes. The small-pore component, on the upstream/inside edge, retains the feedwater and provides a medium through which the feedwater pressure drops as in a traditional sublimator. It is postulated that the large pore component, on the

downstream/outside, is where the ice forms, sublimates (and where water pressure drops) so any residue left over by the feedwater is less likely to clog the larger pores. The ultimate goal of the CIS was for 6000 W of heat rejection and a feedwater utilization rate of 15.3kg/hr but this goal was not realized before the program was cancelled. A mini-CIS was designed and manufactured for a technology demonstration and testing yielded a specific heat rejection of 0.93 kW/kg [20, 37]. During testing, the mini-CIS experienced leaks, both external (the feedwater seeping out of poorly welded points) and internal (feedwater seeping into the coolant loop and vice versa). The research team developed a model for the CIS similar to the model proposed in this research. However, there is not extensive experimental data with which to validate this model [37]. This research effort was halted due to budget cuts in the 2000s.

The sublimator-driven cold plate (SDC), pictured in Figure 2.8, eliminates the cooling loop typical in a sublimator thermal control system by mounting the avionics directly on the thermally conductive base of the sublimator for a simpler design.

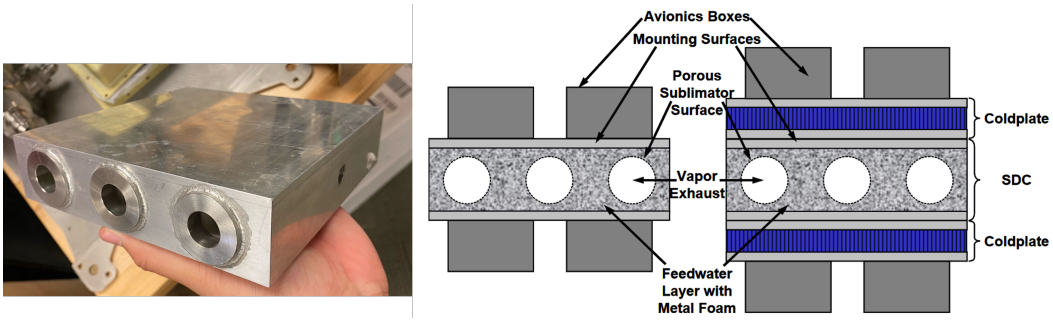

Figure 2.8: Johnson Space Center's sublimator-driven coldplate (SDC) [46]

This design combines the three components of a TCS: heat collection, heat transfer, and heat rejection, into a single integrated unit for mass and volume savings [46]. A CubeSat sublimator will be the most similar to a SDC. The SDC enabled mass savings of up to 25% when applied to the Altair lunar lander [20, 45]. Both the CIS and SDC designs completed varying levels of testing with test results supporting their proposed benefits including feedwater utilization of nearly 100%, meaning that all the feedwater was used [20, 45, 47]. Other than the integrated nature of the design, the SDC is unique in that the porous medium is shaped into a hollow cylinder with the center of the cylinder exposed to vacuum to improve the heat flux uniformity [45]. The sources listed in this paragraph describe multiple varia-

tions of the SDC, such as the Integrated-SDC with avionics bolted directly to the back of the sublimator frame with various configurations of avionics/cold plate/sublimators integration. This research effort was halted due to budget cuts in the 2000s. There is also a sublimator on the Boeing CST-100 Starliner, but publicly available information on this technology is very limited [48].

Chinese National Space Agency (CNSA)

In the last two decades, the Chinese National Space Administration (CNSA) has performed extensive sublimator research and implemented sublimators on their lunar lander, the Chang'E-5, and their spacesuits [25].

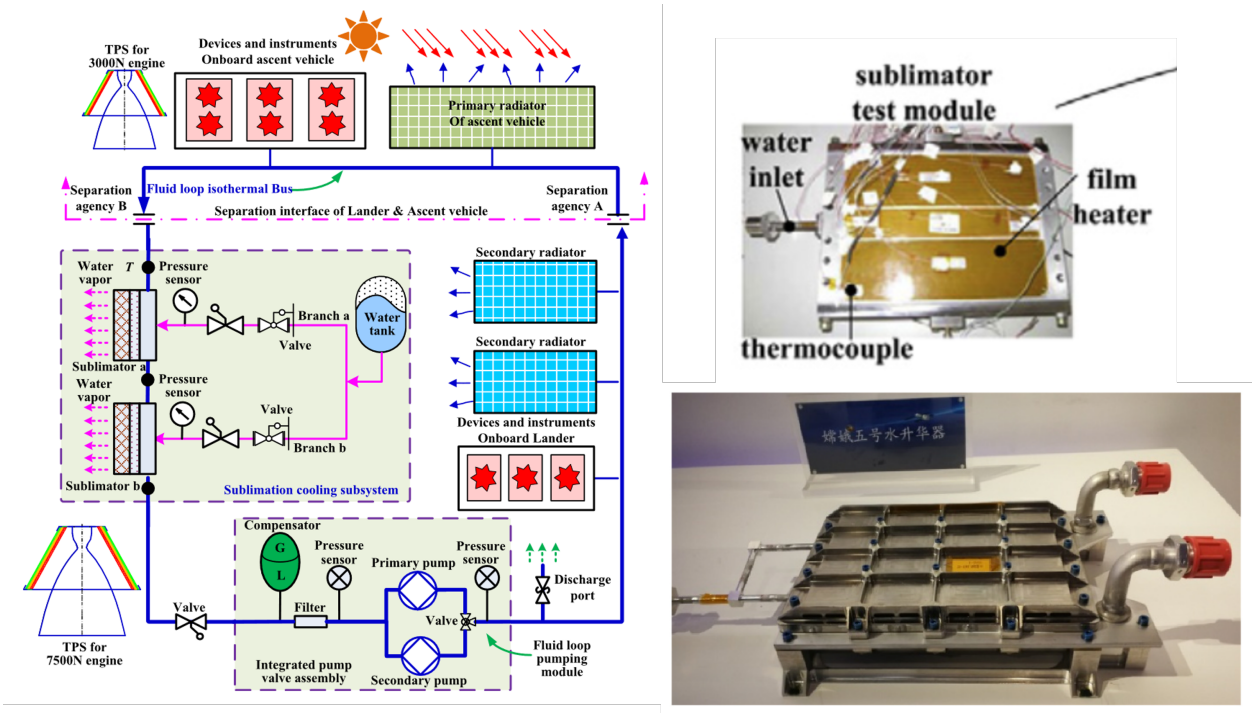

Figure 2.9: CNSA's Chang'E-5 thermal control system schematic [49] and images of sublimator test beds [50].

The Chang'E-5 thermal control system includes a sublimator, shown in Figure 2.9, with a mechanically pumped fluid loop, similar to the Apollo lunar lander and the cancelled Altair lunar vehicle. There are two sublimators on-board, each with a 400W heat rejection capacity, which are able to operate independently or together depending on the waste heat generated in each mission phase. The main purpose of the sublimator(s) is to "guarantee low temperature for the (ascent vehicle) before launching" from the moon, although the specific details of this

are not divulged. The sublimators have the capability of operating in a high temperature lunar environment and they can start-up at $40°C$, hotter than is typical [13]. The Chang'E-5 sublimator performance is detailed in [49]: one sublimator operated for 13.1 hours and the other operated for 7.56 hours with a total water utilization of 5.25 kg over that time period. Leading up to the use of sublimators on the Chang'E-5, there was extensive modeling and ground-based experimentation for the CNSA. Some of the work includes numerical modeling of the complex phase change heat transfer processes which occur within the porous medium [13, 50–53], and other work takes an analytical approach modeled after the Apollo work [25]. This thesis research avoids a CFD approach to modeling the sublimator, but some of the assumptions and boundary conditions used in numerical modeling are addressed in Section 4.4.

2.4 Summary

Over the last 60 years, the sublimator has evolved via a gradual and iterative process. Improvements have been made in material choice, manufacturing methods, and maintenance procedures to increase heat rejection capacity, extend the life, and reduce the chance of anomalies in a sublimator. Despite the sublimators being used successfully for many decades, there is still not a comprehensive and undisputed understanding of the specific heat transfer and thermodynamic mechanisms of sublimation in the porous medium. There is agreement of a general understanding of why they work, as described in Chapter 1.3, and how they break. The EMU is the most-studied sublimator and has the most flight data, but other programs have shown the transferable nature of the sublimator technology to other spacecraft and missions. After the EMU, several years of work were performed at NASA Johnson Space Center to improve the sublimator for other applications, none of which came to fruition. The Chang'E-5 sublimator has been the focus of recent attention, especially pertaining to numerical methods as a means of modeling the sublimator operation. Table 2.1 summarizes the specifications and notable aspects of the main sublimators reviewed in this chapter: the Apollo EMU [15, 26, 27, 29, 31, 33], the Shuttle/ISS EMU [16, 19, 38], the Orlan [39, 40], the X-38 [14, 42], the CIS [20, 37], the SDC [45–47], and the Chang'E-5 sublimator [13,

25, 49]. It should be noted that the columns for "Heat Rejection Range" and "Feedwater Utilization" cannot necessarily be used as comparison for sublimator performance because the porous medium area over which sublimation occurred are varied. These two columns are meant to illustrate the relative scale of the sublimator, its heat rejection capabilities, and its feedwater use. Among all the publicly available test and flight data, the average feedwater flow rate was found to be approximately 0.005 $kg/s/m^2$ and this value will be used for comparison in the model and model validation, Chapters 4 and 6, respectively.

Chapter 3

CubeSat Thermal Control System

The focus of this research is a sublimator rather than an entire thermal control system (TCS) for a CubeSat. For added context, however, Section 3.1 briefly reviews the other components of a CubeSat TCS which enables the sublimator to reject waste heat. Section 3.2 steps through the process to size a sublimator based on mission requirements and Section 3.3 discusses a number of non-thermal related effects caused by a sublimator.

3.1 TCS Components

The term "sublimator" is often used to refer to the feedwater gap and porous medium where the phase change heat transfer process occurs, but a full sublimator assembly includes a number of other components, shown in Figures 3.1 and 3.2.

Sublimator "stack": The primary layers that comprise a sublimator are the thin, flat porous component exposed to vacuum on the outside of the CubeSat and the feedwater gap "behind" the porous component. The feedwater gap is just that—a thin gap through which the feedwater spreads before it enters the porous component. These two layers are surrounded by a thermally conductive and lightweight frame, often aluminum. The porous component and frame are welded, brazed, or fastened together to minimize feedwater leakage around the edges.

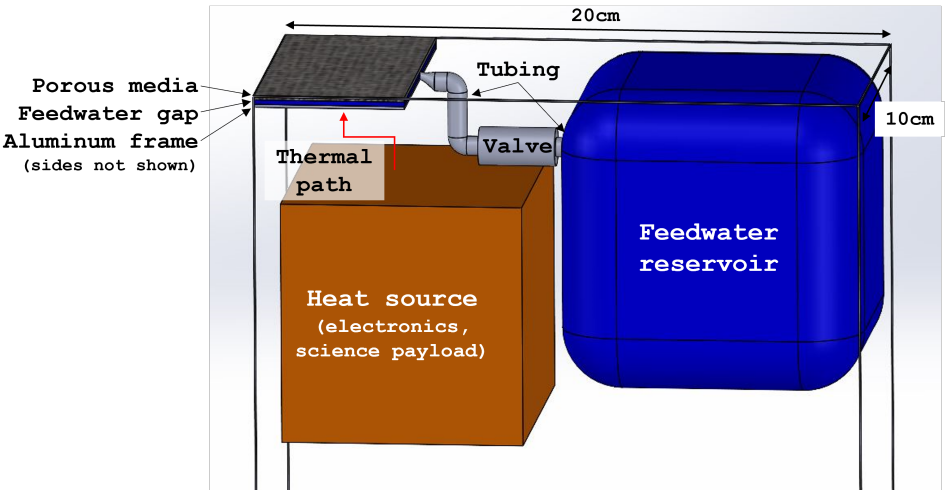

Figure 3.1: CAD visualization of a 6U CubeSat with a sublimator thermal control system. Courtesy Katie Ricketts/ UC Davis 2024.

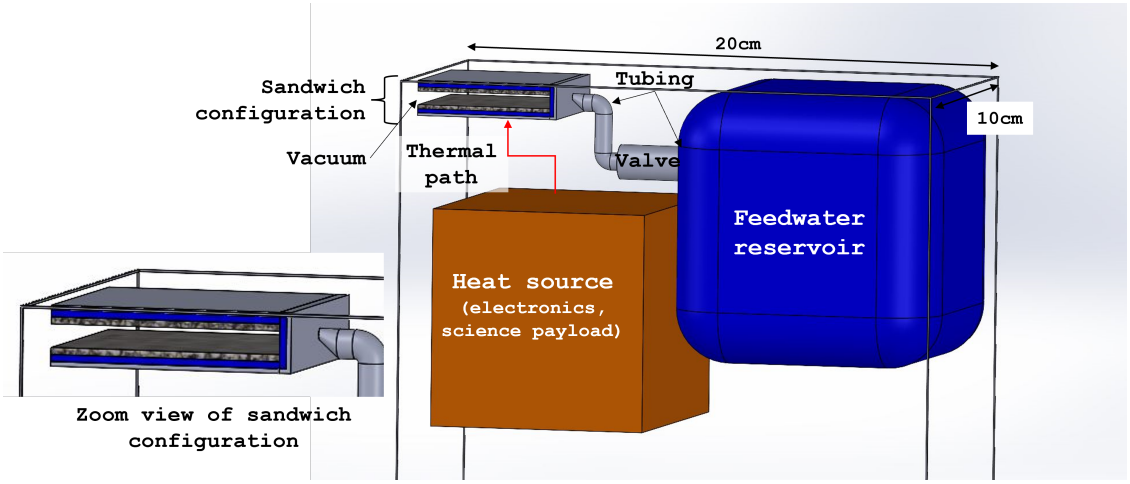

Figure 3.2: CAD visualization of a 6U CubeSat with a sublimator thermal control system in the sandwich configuration. Courtesy Katie Ricketts/ UC Davis 2024.

The aluminum frame is not shown in Figures 3.1 and 3.2. These figures show two different sublimator configurations: first the exposed stack and second the sandwiched stack. Historically, sublimators are designed to be *within* the spacecraft or spacesuit and not on an outer surface. Some designs include a sandwiched scenario while others rolled into a tube-shape and vent water into a tube [16, 27, 37, 45]. The CubeSat is not pressurized internally so any configuration and orientation of the sublimator would expose the porous medium to vacuum.

With the CubeSat sublimator, however, there may be an opportunity for variation in this configuration. In the sandwich configuration (Figure 3.2), solar radiation discussed in Section 3.3.2 is not relevant because the porous surface is not directly exposed to the sun. The sandwich configuration may cause a build-up of water vapor in the vacuum space between the layers, but the build-up is thought to be minimal and does not significantly effect the sublimation behavior. There is room for additional research to explore the specific thermal control system configuration, sublimator integration with the CubeSat, and any affects the sublimator arrangement may have on the sublimation process itself. For simplicity and ease of manufacturing, the author suggests an initial use of the exposed configuration in Figure 3.1.

The feedwater reservoir: water (the consumable) is launched on the CubeSat and enters into the feedwater gap in liquid form. The feedwater may be stored in a flexible bladder made of a material such as Neoprene or Fluorel like that of the EMU (depending on the decade) [16]. Alternatively, the feedwater reservoir may consist of a hard-shell casing with an internal piston or baffles containing a pressurized gas which will expand and push the feedwater out of the reservoir and into the tubing toward the feedwater gap.

Figure 3.3: EMU feedwater bladder [16].

Tubing and Valve: Piping is required to connect the feedwater reservoir to the feedwater gap in the sublimator. The specific hardware required for this part of the sublimator is not within the scope of this research, but a visualization of it is shown in Figure 3.1. The feedwater gap is only a few millimeters thick so it is difficult to connect the tubing directly with the feedwater gap. Instead, a **feedwater channel** is added as as groove in the

aluminum base as shown in Figure 3.4 and the tubing is connected to one end of this groove.

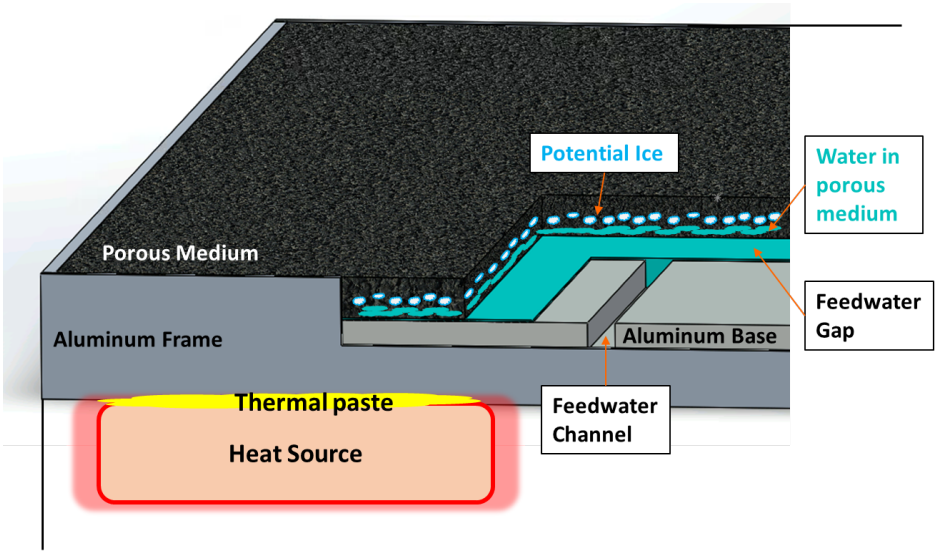

Figure 3.4: Cut-away visualization of a CubeSat sublimator with hardware contacted directly to inner surface of sublimator via thermal paste.

There is an on-off valve which separates the feedwater reservoir and the rest of the sublimator. Typically, this is the only part of the sublimator TCS which requires power. Once the valve is open and sublimation begins, there must be a minimum supply of heat so that the ice layer does not grow outside of the porous medium volume, as explored in Chapter 4 (modeling) and Section 6.5 (design realizability). During sublimator operation, the valve can be closed, but sources do not identify if or when this occurs throughout a mission and what type of control system performs this action. Any control system for opening/closing the valve would measure temperature of the heat source and pressure of the feedwater before it enters the porous component. There are no sensors embedded within the sublimator stack due to volume constraints.

If the sublimator will be in use throughout the entire mission duration, such as an EVA (as opposed to only being utilized during peak heat loads on larger spacecraft), then the valve need only be powered on a single occasion to open for sublimator start-up. While identifying the specifications and requirements for a feedwater valve was not in the scope of this research, there is some historical data to suggest examples of creative low-power solutions. For example, a latching solenoid valve may be used with a low-power solution from the EMU: "...an integral switching system that will effectively turn itself off after the

valve opens or closes" [16]. While a sublimator is generally considered to be a passive approach to heat rejection, it still requires a small amount of power for a short period of time to initiate the flow of feedwater for the sublimation process.

Conductive thermal path: This is required to transfer the waste heat from avionics and payloads to the sublimator. If the sublimator is treated as a cold plate, the heat source may be fastened directly to the inside surface of the encased feedwater gap/porous component stack, shown in Figure 3.4. Thermal conductivity can be enhanced with a thermal paste (Nusil [54]) or interface pads (Laird Tflex sheets [55]).

If the CubeSat cannot be configured such that the heat source is in direct contact with the sublimator, heat pipes or thermal straps may be used [2]. A heat pipe, in Figure 3.5, is a passive device containing an encased liquid and wick which enables one-way heat transfer. The end of the heat pipe connected to the heat source will increase in temperature and vaporize the liquid which travels toward the cold end of the heat pipe, connected to the sublimator. The gas will then condense and travel up the wick via capillary action back to the hot end of the heat pipe and the process repeats [17]. Alternatively, a thermal strap is a flexible highly conductive connection between the heat source and heat sink. For example, a thermal strap can be a series of thin aluminum sheets stacked together or braided copper wire with brackets on both ends [2, 17], as in Figure 3.5.

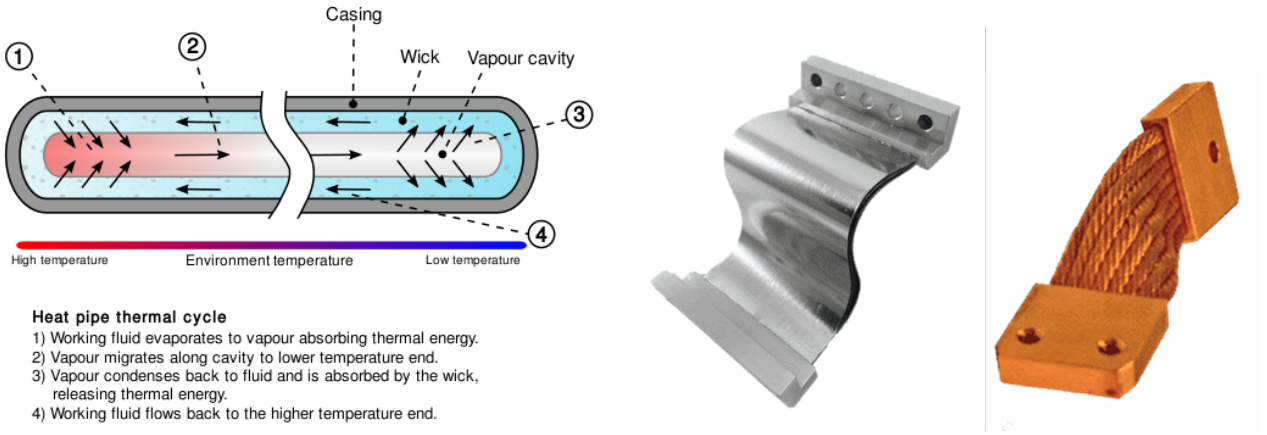

Figure 3.5: Left: Heat pipe mechanism [56]. Right: aluminum ribbons and braided copper thermal strap examples [57].

Additional components: the feedwater pressure regulator is used to ensure the feed-

water does not exert too much pressure on the porous component and cause it to flex or bend, as has been observed in the past, would be considered an additional power consumption device [16]. A CubeSat sublimator will be less than half the surface area of the EMU sublimator so bowing of the porous component is less likely and a feedwater pressure regulator is likely not required. During a future technology demonstration mission, additional sensors may be added to measure temperature at the porous medium, gathering data that has as-yet not been collected on-orbit and is critical to better understanding sublimator effectiveness. Lastly, the sublimator stack of the porous component and aluminum base (with the feedwater gap in-between) is encased in a highly conductive aluminum frame. It is common to weld or braze the outer edges of the porous component to the frame to ensure no feedwater leakage or ice expansion through the edges occurs. These added components are taken into account in the sublimator sizing procedure with a 20% increase in the predicted mass.

3.2 Sizing a Sublimator

In order to gain a general sense of the scale of a CubeSat sublimator, an initial sizing procedure is enumerated below. As with any spacecraft thermal design, this process is iterative in that it requires an approximation of the available resources for a thermal control system, and these approximations should be revisited after the initial sublimator sizing is complete. The sublimator size is driven by the CubeSat configuration, such as the available "real-estate" for sublimator surface area exposed to vacuum and the amount of thermal energy which must be rejected.

Let us consider a 6U CubeSat (1U is a 10cm x 10cm x 10cm volume) on a short duration mission (a few days) during which the sublimator must reject 50W of waste heat for a total of 15 hours. We assume that the CubeSat has half of the surface area of one side of a 1U (1/2 x 10cm x 10cm) available for sublimator exposure to vacuum - this is the assumed sublimation area.

1. Using the mission requirements, compute the **heat flux** which must be rejected by the

sublimator:

$$q" = \frac{q}{A} = \frac{50\ W}{0.005\ m^2} = 10\ kW/m^2$$

$q" = 10kW/m^2$ is within an appropriate range based on sublimator heat rejection requirements with flight heritage, $6 - 12\ kW/m^2$ [44, 45].

2. Calculate the amount of **feedwater required** for the sublimator.

   - Equation 1.4 is used to determine the mass flow rate, given the heat load and assuming an enthalpy of vaporization at $0°C$ [18]:

   $$\dot{m} = \frac{q}{h_{lv}} = \frac{50\ W}{2.5009 * 10^6\ J/kg} = 2.0 * 10^{-5}\ kg/s \quad \text{or} \quad 72\ grams/hr$$

   - A 15-hour sublimation duration at the calculated sublimation rate yields **1.08 kg of feedwater** which occupies a volume slightly greater than 1U.

3. Using historical sublimator parameters, calculate the required sublimator **volume and dry mass**.

   - The stainless steel porous component is 1.5mm thick, the feedwater gap is 1mm thick, and the aluminum frame is 1mm thick. The cross-sectional area of the sublimator is 5cm x 10cm. The volume of the sublimator, excluding the feedwater bladder and tubing, is **17.5** cm^3.
   - Use the densities of 316L stainless steel (8000 kg/m^3 [17]) and aluminum (2720 kg/m^3 [17]) to calculate the sublimator dry mass. Add 20% to account for an additional mass from a frame, feedwater tubing, and fasteners/welds. The dry mass of the sublimator assembly is **88 g** (0.194 lb).

4. Add the dry mass and feedwater mass to obtain the total sublimator assembly mass: **1.17 kg**. Add the volume of the sublimator stack and the feedwater to obtain the total sublimator assembly volume: **1098 cm^3**, slightly larger than a 1-U CubeSat volume.

The sublimator sizing process is summarized in Table 3.1. The greatest constraint is mass and volume required for the feedwater consumable. For a short-duration CubeSat mission with power dense electronics or payloads, the shortcomings of a sublimator may be

acceptable. As mentioned in the introduction, sublimators can handle a wide range of heat input (waste heat) while maintaining the heat source in an acceptable temperature range, so the advantages of the sublimator outweigh the drawbacks.

Table 3.1: Summary of CubeSat sublimator specifications.

Parameter	Value
CubeSat size	6U
Waste heat	50 W
Heat rejection duration	15 hours
Available surface area	50 cm^2
Heat flux	10 kW/m^2
Feedwater mass	1.08 kg
Total volume (approx)	10.3 x 10.3 x 10.3 cm^3
Total mass	1.125 kg

For comparison, astronauts on EVAs generally produce 150 – 400 W of heat which needs to be rejected from the EMU. The EMU sublimator surface area is about 230 cm^2 and has a dry mass of 1.6 kg [16] and a feedwater mass of 3.62 kg [35]. Perhaps a better comparison is an active CubeSat thermal control technology. Table 3.2 compares the specifications from the initial sublimator sizing procedure to the requirements set forth in the Active CryoCubeSat mission [6]. The sublimator requirements are comparable to the MiniCryoCooler technology.

Table 3.2: Comparison of thermal cooling systems.

Requirements	Mini CryoCooler	Example CubeSat Sublimator
Thermal Load	>30 W	50 W
Power	<4 W	0 W[1]
Mass	<2 kg	1.125 kg
Volume	<1U	1.08 U

[1]see discussion in beginning of this chapter

In the future, when a full sublimator TCS for a CubeSat is tested, its success can be measured with a number of parameters such as efficiency ratios (waste heat rejected per unit mass or per unit volume), versatility (range of waste heat rejection capability), and feedwater utilization (%), or how much of the on-board feedwater was used.

3.3 CubeSat Systems Considerations

3.3.1 Thrust from Sublimator

One of the concerns of a sublimator on a CubeSat is the thrust the vented water vapor may impart on the small spacecraft. This phenomena has never been explicitly observed, but there are reports that sublimator venting was a possible concern in attitude control during the Apollo 13 mishap and during some EVAs [58, 59]. Assuming steady-state operation of the sublimator, the equation for linear momentum is used: $p = mV$, to compute the thrust due to sublimation. Note that p here is momentum ($kg \cdot m/s$), v is velocity (m/s), and m is mass (kg) [60]. The time-derivative of linear momentum is taken to yield an equation for force, written here in unidirectional scalar form:

$$\frac{dp}{dt} = \frac{d}{dt}(mV) \quad \rightarrow \quad \frac{dp}{dt} = v\frac{dm}{dt} \quad \rightarrow \quad F = \dot{m}v_e \tag{3.1}$$

where v_e denotes exit velocity in m/s and $\dot{m}$ is the mass flow rate - in this case the sublimation rate in kg/s. Equation 3.1 can be rewritten in terms of thrust, $\mathbf{T} = \dot{m}v_e$. Chapters 2 and 6, specifically Tables 2.1 and 6.3, show the historical mass flux rates ($\dot{m}$ per unit area). These values were applied to the CubeSat sublimator area and the average was taken as $\dot{m} = 3.55 * 10^{-5}\ kg/s$. The minimum velocity of the venting water vapor is obtained from

$$v_e = \frac{\dot{m}}{\rho A} \quad \text{where} \quad \rho = \frac{pM_{H_2O}}{RT}$$

where the pressure (p) and temperature (T) are the triple point of water and the universal gas constant (R) and molar mass of water (M_{H_2O}) are physical constants. Computed from the average $\dot{m}$ above, the vented water vapor velocity from literature is $v_e = 3.59\ m/s$. The minimum thrust imparted on the CubeSat by the sublimator is $\mathbf{T} = 1.27{*}10^{-4}\ N$. Assuming the 6U CubeSat weighs 1 kg per U, the acceleration can be calculated by

$$a = \frac{\mathbf{T}}{m} = \frac{1.27 * 10^{-4} N}{6\ kg} \ = \ 2.124 * 10^{-5} m/s^2 \tag{3.2}$$

which is equivalent to 2.16 μG. The upper limit for the velocity of the water vapor molecules exiting the sublimator is calculated by the root mean square speed from the Kinetic Theory

of Gases [23]:

$$v_{rms} = \sqrt{\frac{3RT}{M_{h_2O}}} \quad = \quad v_{rms} = 615 m/s \tag{3.3}$$

Using Equation 3.1, the thrust is calculated to be $F = \mathbf{T} = 0.0218\ N$ and the acceleration due to this thrust upper limit is

$$a = \frac{\mathbf{T}}{m} = \frac{0.0218N}{6\ kg} \ = \ 3.63 * 10^{-3} m/s^2 \tag{3.4}$$

which is equivalent to 0.370 Gs. The velocity and mass flow rates were calculated/taken from historical data and not from the experimental data in Chapter 5 because that water vapor is superheated and near saturation, as discussed in that chapter. Note that molecules exit the sublimator in a whole variety of directions and it is highly unlikely that all, or even some, of the exiting water vapor molecules will impart a thrust of the upper limit magnitude on the CubeSat.

Figure 3.6 plots the contribution of various external disturbances to a spacecraft orbiting Earth [61]. The x-axis is spacecraft altitude and the y-axis is spacecraft acceleration as a result of an external force. The most common ones are emphasized, such as J2 perturbations (perturbations from Earth's oblate nature), solar radiation pressure (SRP), and atmospheric drag. The water vapor vented from the sublimator, in between the two red lines, would cause a 6U CubeSat to accelerate (or decelerate, depending on the orientation) at the same magnitude as other common forces in the orbital environment.

While acceleration due to sublimator venting is not negligible, it can be mitigated and accounted for in a similar manner to aerodynamic drag (i.e. orbital boosts, station-keeping, or acceptance of decreased altitude over time). In fact, the sublimator orientation may even be used to counteract some of these other disturbances or boost the CubeSat's orbit if need be. If there is a CubeSat in low altitude orbit with a sublimator used to cool an IR camera which produces significant waste heat, the sublimator can be used for waste heat rejection as well as propulsion. The concept of operations for this type of mission would be challenging to execute because it would require the cycling of the sublimator according to propulsion needs, not just thermal requirements. Alternatively, a sublimator may be configured such

that there are two porous components on opposite sides of the CubeSat to counteract each other.

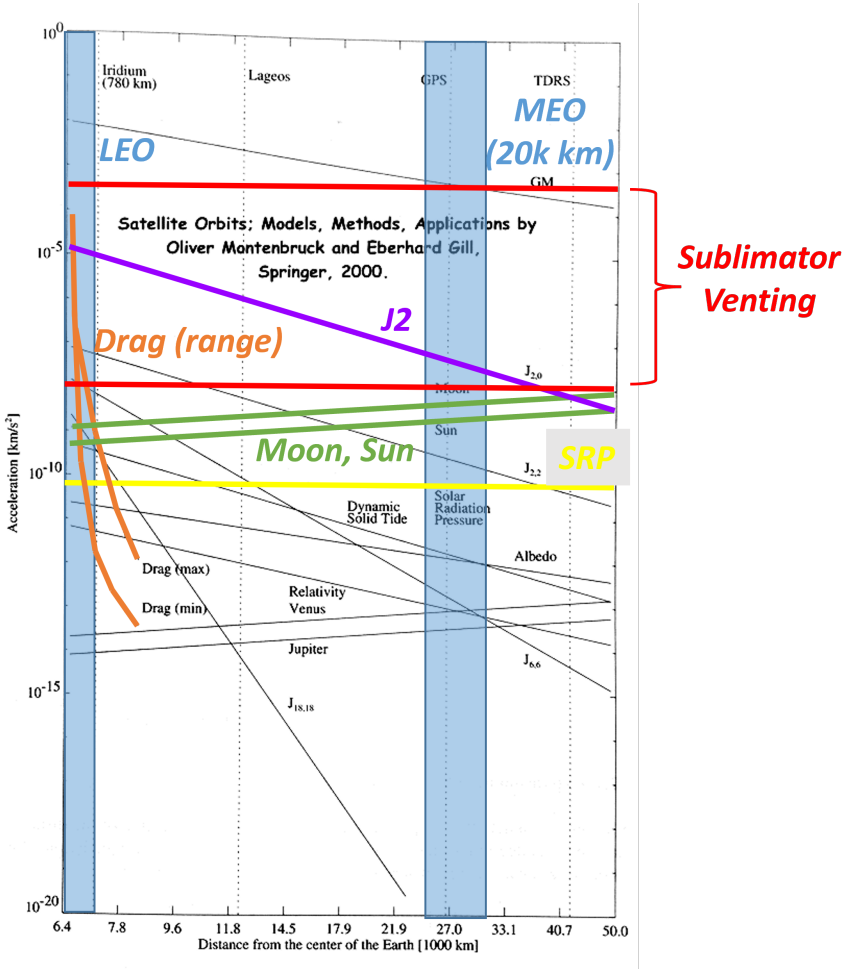

Figure 3.6: Contribution of disturbances to satellites in earth orbit. Courtesy Adam Zufall [61].

3.3.2 Solar Radiation Heating

A sublimator is advantageous because it functions the same way independent of its orientation, unlike a radiator which rejects heat as a function of its orientation relative to the sun, Earth, and deep space. One of the designs for the CubeSat sublimator places the porous medium on the outer surface of the CubeSat, directly exposed to the thermal environment of space, as in Figure 3.1. In this exposed configuration, the sublimator must reject the thermal load generated by the heat source *and* the thermal load from the sun. Using the first law of thermodynamics, from Equation 1.1, a zeroth order approximation energy balance is

performed for the CubeSat:

$$q_{in} = q_{out} \tag{3.5a}$$

$$q_{sol} + q_{gen} = q_{sub} + q_{rad} \tag{3.5b}$$

The thermal loads on the CubeSat are from solar radiation, $q_{sol} = A_{sol} S\alpha$, and the on-board heat source, q_{gen}. The heat rejected by the CubeSat sublimator is due to sublimation (as designed), q_{sub}, and radiation from the exposed porous medium, $q_{rad} = \sigma A_{rad} \epsilon (T_{sc}^4 - T_\infty^4)$. q_{sol} and q_{rad} from Equation 3.5 are rewritten as

$$A_{sol} S\alpha + q_{gen} = q_{sub} + \sigma A_{rad} \epsilon (T_{sc}^4 - T_\infty^4) \tag{3.6}$$

where A_{sol} is the area exposed to solar radiation and A_{rad} is the radiating area, in this case they are the same. S is heat flux from the sun, an average solar constant of 1367 W/m^2 for LEO. $\alpha = 0.44$ is the absorptivity of a stainless steel surface, assumed to be a smooth plane (no roughness from pores), and $\epsilon = 0.14$ is its emissivity [17]. When using optical properties, the cut-off for applying the α and ϵ values of a smooth surface to an imperfect surface is $5\mu m$, within range of the pore size in a sublimator. The pores can be treated as a *hohlraum*, a cavity with near-perfect absorptivity ($\alpha = 1$) and emissivity ($\epsilon = 1$). Thus, the optical properties of the porous medium are calculated using a weighted average:

$$\alpha_{sub} = \phi \alpha_{pore} + (1 - \phi)\alpha_{SS} \quad \rightarrow \quad \alpha_{sub} = 0.1 * 1 + 0.9 * 0.44 \quad \rightarrow \quad \alpha_{sub} = 0.496 \tag{3.7}$$

and

$$\epsilon_{sub} = \phi \epsilon_{pore} + (1 - \phi)\epsilon_{SS} \quad \rightarrow \quad \epsilon_{sub} = 0.1 * 1 + 0.9 * 0.14 \quad \rightarrow \quad \epsilon_{sub} = 0.226 \tag{3.8}$$

σ is the Stefan-Boltzman constant, $5.67 * 10^{-8} W/m^2 K^4$, T_{sc} is the spacecraft temperature, in this case assumed to be the temperature of the sublimator, about 273 K, and T_∞ is the temperature of space, 4K. The heat generated by the CubeSat is $q_{gen} = 50\ W$, taken from Section 3.2. The heat load from solar radiation is calculated to be $q_{sol} = 3.39\ W$, about 7% of the heat generated by the CubeSat, and the amount of heat the sublimator radiates is $q_{rad} = 0.35\ W$. Thus, the heat load the sublimator must reject is

$$q_{sub} = q_{sol} + q_{gen} - q_{rad}$$
$$q_{sub} = 3.39 + 50 - 0.35 \approx 53\ W \tag{3.9}$$

This heat rejection requirement for the sublimator yields a heat flux of

$$q" = \frac{q_{sub}}{A_{sub}} = \frac{53\ W}{0.005\ m^2} = 10.6\ kW/m^2 \tag{3.10}$$

which is within an appropriate historical heat flux range of $6 - 12\ kW/m^2$ for sublimators. When an energy balance is performed which accounts for the sublimator's intended function, then the thermal load from the space environment is not overwhelming. For comparison, if the sublimator was not operating and instead treated as an insulated plate in direct sunlight, then its temperature would be well above freezing [60]. Using Equation 3.6 and ignoring q_{sub} and q_{gen}, the temperature of the sublimator (and spacecraft) can be solved for using only radiation heating:

$$T_{sc} = \sqrt[4]{S\left(\frac{\alpha}{\epsilon}\right)\left(\frac{A_{sol}}{A_{rad}}\right)/\sigma} \tag{3.11}$$

Using the same values as before, this yields a temperature of a whopping $T_{sc} = 260°C$. This exceedingly hot sublimator surface temperature is from the high α/ϵ ratio of stainless steel which does not have the optical properties chosen for spacecraft [17]. For a radiating surface, a low absorptivity and high emissivity is desired, ideally a ratio < 1, but that is not necessarily a requirement when the sublimator is rejecting heat via phase change heat transfer rather than via radiation.

3.3.3 Miscellaneous Considerations

Another consideration for a CubeSat with a sublimator is the changing center of mass and moments of inertia as feedwater is consumed. This requires more research and close collaboration with mass properties and attitude determination and control engineers. The center of mass could be maintained throughout the mission if the feedwater reservoir is placed strategically in the CubeSat, but that may not always be an option. In addition, if the CubeSat payload includes highly sensitive instruments such as an IR camera, there may be

a requirement to place the sublimator as far from the cameras as possible to avoid any water vapor condensation on important sensing surfaces. Another unexpected and slightly unusual consideration occurred during the Apollo 13 aborted mission is the reflection of the sunlight off the sublimator surface which made it difficult for the crewmembers to identify stars for navigation purposes [58]. This is not expected to be a concern during nominal operations, but more exploration may be required, especially if the sublimator surfaces will be in the field of view of a highly sensitive camera.

This chapter briefly reviewed the various components of an integrated sublimator thermal control system and stepped through an initial sizing procedure. The next chapter delves deeper into the phase change heat transfer phenomena in the porous medium in order to better understand how to choose an appropriate porous component for the CubeSat sublimator.

Chapter 4

Sublimator Model

4.1 Goals of the Model

The model discussed in this section describes and predicts the heat transfer and thermodynamic processes which occur within a sublimator to reject waste heat via sublimation (and sometimes evaporation). First, this chapter will review the shortcomings and knowledge gaps mentioned in the literature review as well as any assumptions and their ramifications. Next, with the assumptions in mind, two parts of the model are developed to predict CubeSat sublimator operations: (1) the overall sublimator is modeled as a thermal resistance network with a focus on conductive heat transfer; and (2), a mass flow model which includes phase change heat transfer and rarefied flow (diffusion) through porous media. After that, unique approaches are taken to describe the evaporation case. Finally, the conduction and rarefied diffusion models are combined to show the temperature and pressure distribution through a sublimator and how they relate back to the temperature of, and heat flux from, the heat source.

The overall inputs of the model are:

- Waste heat (heat flux). This includes, but is not limited to, thermal energy generated from electronics such as computers and IR cameras as well as the maintenance and sensing key parameters of biological payloads.
- Mission duration and percentage of time the sublimator is expected to be used. This

information was used in Section 3.2 in the initial sizing procedure for the CubeSat TCS.

The ultimate outputs of the model include:

- Sublimator surface area, obtained from the initial sublimator sizing procedure.
- Mass of feedwater required, obtained from the initial sublimator sizing procedure.
- Sublimator geometry: average pore size and range of pore sizes, porosity, and thickness of the porous medium. The realizability plots in Section 6.5 expand on these model outputs.
- Conditions under which anomalies may occur. This information will be evident after the modeling approach is understood.

In Chapter 6, the model will be validated with the following inputs taken into account:

- Operating and survival temperature ranges. This information is not used in the model per se, but it would be used to check if the proposed sublimator design meets these requirements.
- Reference data and historical data to compare with experimental data and results from model predictions.

4.2 Shortcomings & Knowledge Gaps

The literature review in Chapter 2 covers sublimator work over the last 60 years. This section reviews the specific gaps in knowledge and shortcomings apparent in various sublimator models, many of which are addressed in this research. Some of the assumptions made in historical models are:

1. The sublimator **porous medium temperature** is at the triple point temperature of water, $0°C$ and 611.65 Pa [16, 31, 43, 62]. Sections 4.5 and 4.6 show why this assumption is reasonable.

2. Ice sublimation temperature: the **ice sublimates at a temperature** just below the triple point of water, rather than at any temperature lower than $0°C$. In contrast, there are unvalidated claims made by Apollo-era subject matter experts at Hamilton Sundstrand about the sublimator porous plate temperatures being "very, very cold". Sections 4.5 and 4.6 show why the former assumption is appropriate.

3. The **ice-vapor interface** moves glacially upstream or downstream depending on the heat flux [15]. This phenomena has been touched on in historical models, and is expanded upon in the vapor diffusion model discussion, Sections 4.6.2.3 and 4.8.

4. The **location of the ice** is a function of the pressure drop across the porous medium [31, 42] and the thickness of the ice layer is a function of the heat flux into the porous medium [14, 15, 53]. This is explored in Sections 4.5 and 4.6.

5. There is a **cyclical nature** of sublimation (until the ice layer is gone) and evaporation (until the liquid water is cold enough to freeze again). This process is briefly mentioned in Section 1.3 and it is similar to the transient sublimator start-up process discussed in Section 1.4.

6. There have been a variety of claims as to the **location of ice formation** without experimental data to support these notions. The ice in the porous medium has not been observed or measured experimentally [50]. There is no plausible sensing technique because of the low-porosity nature of the solid, the micro-size pores, and the potential that accessing/sensing the phase change process could potentially disturb and affect the sublimation process itself. Figure 4.1 shows the possible locations of ice hypothesized by different authors. Seven distinct sources assert that ice is formed somewhere within the porous medium, while a few other sources have alternate understandings. This research will demonstrate where ice is formed in the porous medium and how heavily it depends on the heat loads. The ramifications of the location of ice is discussed in Section 4.8.

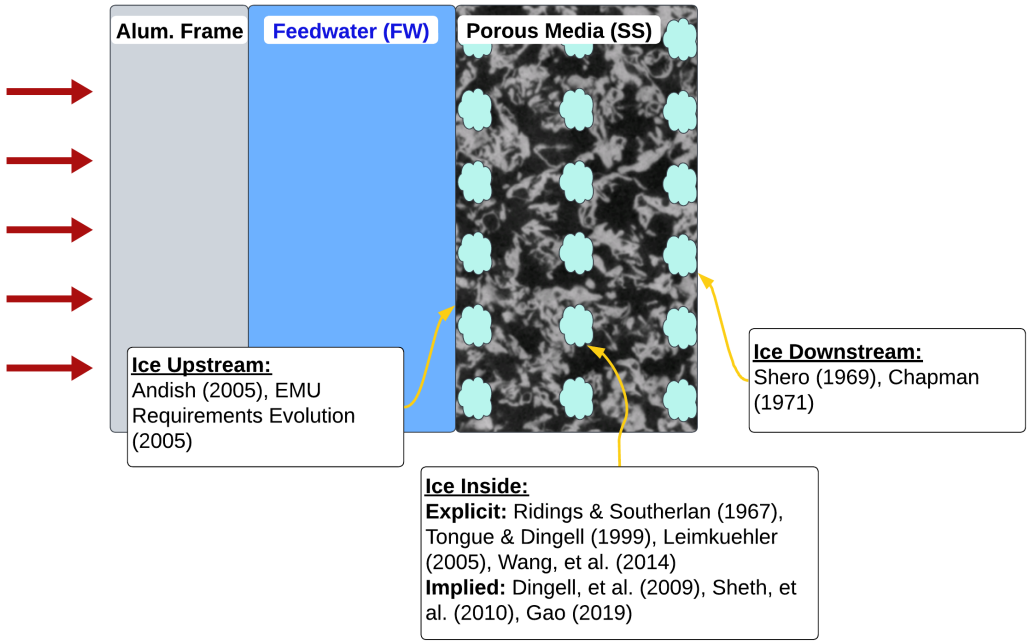

Figure 4.1: Side view visualization of a sublimator indicating locations of assumed ice formation.

4.3 Thermal Resistance Circuit

Figure 4.2 shows the "layers" of a sublimator, beginning with the heat source on the left and moving toward the vacuum of space on the right of the image, modeled as a thermal resistance circuit in Figure 4.3. The variables defined in this figure are used in developing a series of conduction equations to obtain the temperature gradient and other unknowns. These solutions are coupled with the Weber Equation for rarefied flow (Section 4.6) to obtain a full picture of the micro-scale heat and mass transfer phenomena.

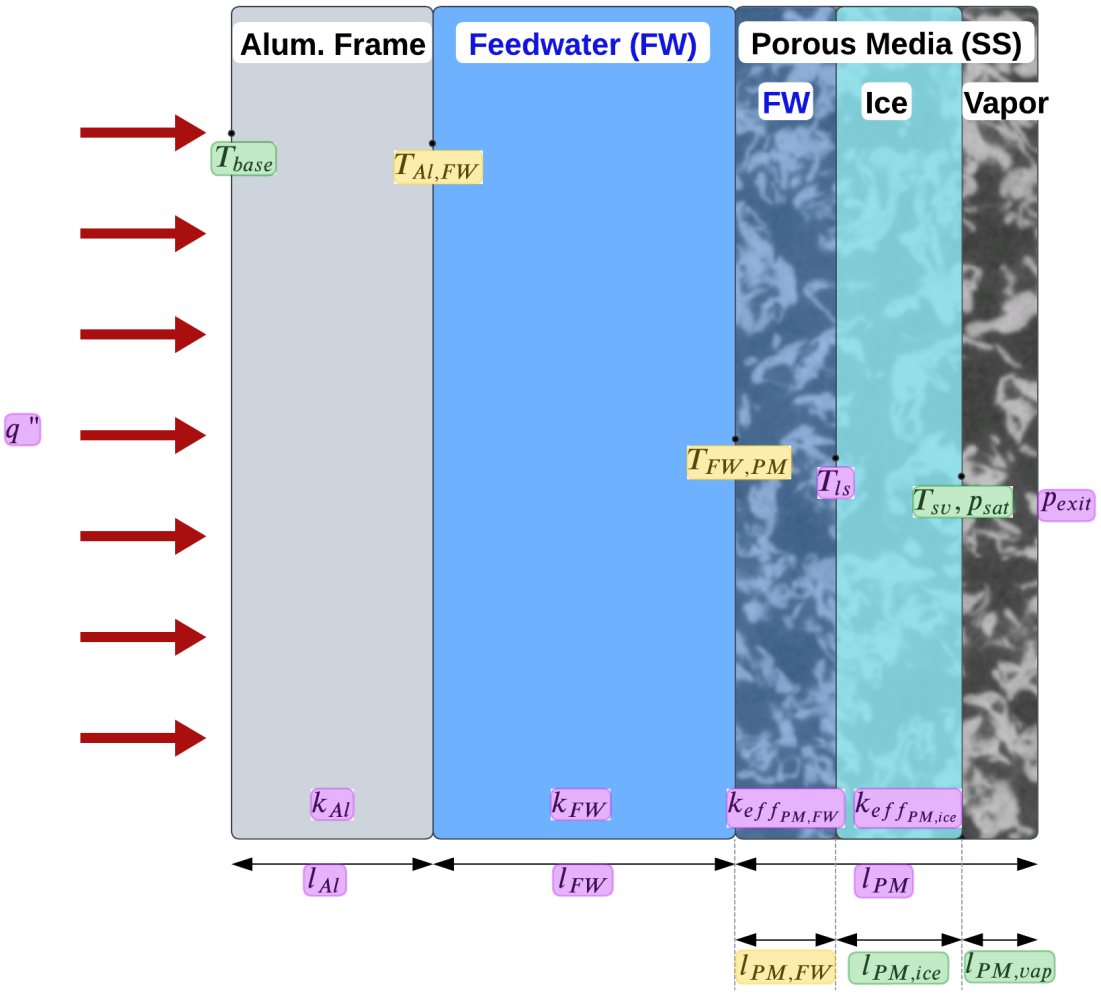

Figure 4.2: The "layers" of a sublimator oriented with the heat source to the left of the figure and the vacuum of space to the right of the figure.

The purple variables are known/user defined, the yellow variables can be solved for via one-dimensional, steady-state conduction and require sublimator design parameter inputs, and the green variables are solved for with a combination of conduction and mass diffusion equations and also require sublimator design parameter inputs. The temperatures and thermal conductivity values in Figure 4.2 are represented in the thermal resistance circuit in Figure 4.3. Note that the last resistor is denoted as R_{flow} to represent the resistance to flow posed by the porous medium and the nodes on either side represent pressures. The $1/k$ values represent the inverse relationship between thermal *resistance* and heat transfer (i.e. low thermal conductivity = high resistance to heat transfer = less heat conduction).

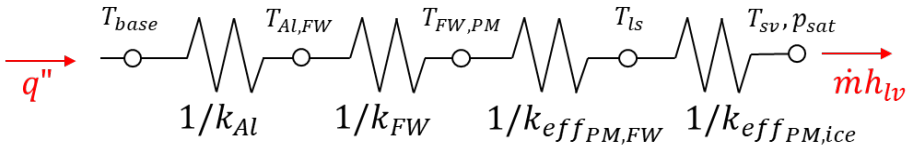

Figure 4.3: The "layers" of a sublimator oriented with the heat source to the left of the figure and the vacuum of space to the right of the figure, represented as a thermal resistance network.

4.4 Assumptions

While this research aims to address many of the assumptions and shortcomings from previous sublimator research (Section 4.2), there are other assumptions made to simplify the analytical model. Some of the assumptions in this section are shown to be accurate, while others are accepted with the understanding that future research may lead to the relaxation of these assumptions.

1. Steady-state & one-dimensional heat and mass transfer: The transient start-up process for a sublimator is described conceptually in Section 1.4, but is not the focus of the model. With a better understanding of the quantitative relationships between heat/mass transfer and temperature/pressure during steady-state operation, the transient case can be revisited. In addition, the sublimator porous medium is a complex geometry so the one-dimensional assumption was made to simplify the model and analysis. This assumption means that spatial differences throughout the porous medium volume are not captured, which would help characterize two anomalies during sublimator operation: feedwater or ice leakage around the edges and "hot spots" which may lead to feedwater breakthrough [16, 19, 38]. That being said, there is some exploration of the tortuosity of a porous media (the degree of "twists and turns" of the diffusing gas) which accounts for some three-dimensional flow effects, discussed in Sections 4.6.2.3 (model) and 5.1.1 (experiment).

2. Temperature of the water or ice in the porous medium: When modeling the temperature gradient in the sublimator, heat conduction through porous media must be considered, not just conduction through the feedwater gap. The porous medium is approxi-

mated as a solid metal. The importance of the transient response is negligible because the temperature of the water or ice in the porous structure will rapidly equilibrate to the surrounding metal structure. The transient heat transfer analysis of a spherical drop of water surrounded by stainless steel is shown below in Figure 4.4 [24]. In this visualization, the sphere represents water surrounded by metal (not shown) with a spatial and temporal temperature gradient. While the general model assumes steady-state conditions, the transient response of the water/ice within the pores is used to support the assumption described here. The calculations below solve for the time it takes for the center of the "water sphere" to reach 90% of the surrounding metal temperature (a conservative, yet somewhat arbitrary, percentage).

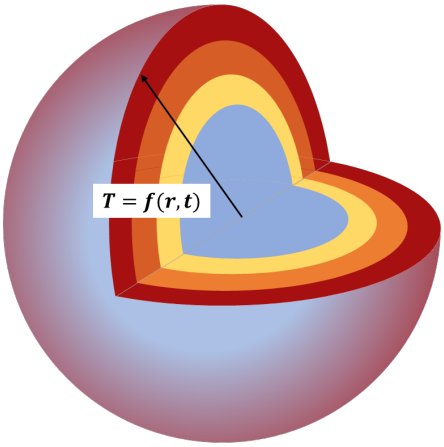

Figure 4.4: Visualization of water/ice sphere in transient heat transfer problem.

The Biot number is a dimensionless number defined as

$$Bi = \frac{hr}{k} \tag{4.1}$$

where h is the heat transfer coefficient ($h = \infty$ for a fixed center temperature), r is the characteristic length (pore radius, m), and k is the thermal conductivity of water or ice (W/mK). The inverse, Bi^{-1} is taken and used in the Heisler Chart in Figure 4.5 to find the Fourier Number, Fo. Bi^{-1} is zero because the convective heat transfer coefficient is infinity. At the boundary where the water/ice sphere comes in contact with an infinite thermal mass (the metal structure), there is a step-change and thus $h = \infty$ and $Bi^{-1} = 0$. On the Heisler chart, the y-axis is determined by the expression below:

$$\theta_0^* = \frac{\theta_0}{\theta_i} = \frac{T_0 - T_\infty}{T_i - T_\infty} \tag{4.2}$$

Θ_0 is the ΔT between the center of the sphere and the surrounding metal. Θ_i is the ΔT between the initial uniform temperature of the sphere and the surrounding metal. When the temperature of the center of the sphere, T_0, is 90% the temperature of the surrounding metal substrate, T_∞, θ_0^* is approximately 0.1. On the Heisler chart, where $\theta_0^* = 0.1$, $Fo = 0.4$.

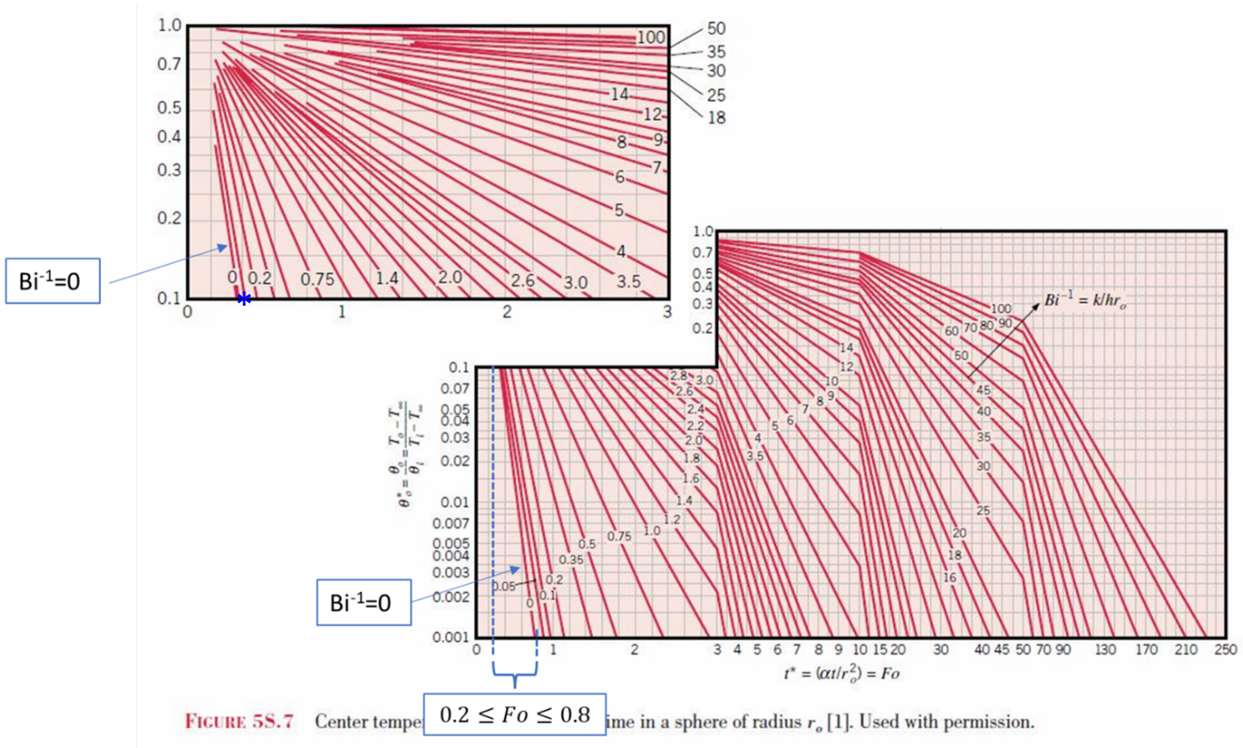

FIGURE 5S.7 Center tempe ime in a sphere of radius r_o [1]. Used with permission.

Figure 4.5: Heisler chart for transient conduction for a sphere [24].

Next, the Fourier number is used to find the time it would take for the center of the sphere to reach 90% of the surrounding metal temperature:

$$Fo = \frac{\alpha t}{r^2} \quad \rightarrow \quad t = \frac{For^2}{\alpha} \tag{4.3}$$

where α is the thermal diffusivity of water ($0.132 * 10^{-6}$ m/s at $10°C$) or ice ($1.18 * 10^{-6} m/s$ at $0°C$) [24]. Solving for time yields

$$t_{ice} = 3.5\mu s \qquad t_{water} = 27\mu s$$

As a qualitative check, note that ice has a greater thermal diffusivity (lower specific heat capacity) and conductivity than water, so the ice in the pores does not take as long as liquid water to equilibrate with the surrounding metal substrate ($3.5\mu s$ compared to $27\mu s$). Without any phase change heat transfer, *the temperature of the water or ice can be assumed to be equal to the temperature of the surrounding porous media.* On the time scale of sublimator operations, the time constants calculated here are much less than the sublimator's transient period. At the phase change interface, the saturation pressure becomes more influential, as discussed in Section 4.6.2.3. Even though heat transfer between the water/ice and the metal structure is ignored, the effective thermal conductivity values ($k_{eff_{PM,FW}}$ and $k_{eff_{PM,ice}}$) are still used in the conduction model for the porous medium.

3. Thermal mass of the water vapor: this assumption posits that the thermal mass of the water vapor in the porous medium is negligible compared to the thermal mass of the liquid water or ice in the porous medium. This is supported by comparing the mass of water vapor and liquid water if each of those phases were to occupy the entire porous media void space. Using the ideal gas law (the validity of which is shown in Section 4.6.2.3), the mass of the water vapor is

$$m = \frac{pVM_{H_2O}}{RT} \;=\; 3.53 * 10^{-8}\ kg \;=\; 0.0353\ mg \tag{4.4}$$

where T is the temperature of water vapor (say $10°C$ for a conservatively high vapor pressure) and p is the water vapor pressure which assumes a saturation pressure of $1.227\ kPa$. M_{H_2O} is the molar mass of water ($0.01805\ kg/mol$), R is the universal gas constant ($8.3145\ K/molK$), and V is the volume occupied by the water vapor. If the entire void space of the porous medium is occupied by the water vapor and the sublimator size is taken from Section 3.2 with porosity of $\phi = 50\%$ (not a realistic porosity; sublimators are typically much less porous), then $V = 10cm \;*\; 5cm \;*\; 1.5mm \;*\; 0.5 \;=\; 3.75\ cm^3$.

By comparison, the liquid water mass required to completely fill the porous medium is

$$m = \rho V \;=\; \left(998\frac{kg}{m^3}\right)\left(3.75 * 10^{-6}\ m^3\right) = 3.74\ g$$

The mass of liquid water, if it occupies the same volume in the porous medium as the water vapor, is almost 10^5 times greater. The calculation for ice is similar because the density of ice is close to that of liquid water, 917 kg/m^3. Thus, the thermal mass of the water vapor is negligible and any changes associated with sensible heat (temperature change) can be ignored. The thermal energy the water vapor molecules impart on upon collision with the porous structure may be ignored because its mass is negligible compared to the liquid water mass.

The sensible heat transfer from a decrease in temperature of the feedwater from the reservoir (around room temperature) down to the triple point, is small compared to heat transfer via phase change. The change in specific sensible heat (per unit mass) is calculated by

$$q_{sens} = c_p \Delta T \tag{4.5}$$

where cp is the specific heat capacity of liquid water, 4.2 $kJ/kg - K$ and $\Delta T = 20K$, so $q_{sens} = 84\ kJ/kg$. The latent heat of vaporization is 2500 kJ/kg [18], so any sensible heat transfer is small compared to heat transfer via phase change and is neglected.

4. Conductive heat transfer through the feedwater gap: the next assumption posits that the heat transfer through the feedwater gap is via conduction, not advection. Historically, the feedwater is flowing through the feedwater gap at an average rate of $\dot{m} = 0.005\ kg/s$ [15, 16, 43, 45, 47, 52, 63] which equates to a flow rate of 0.001 m/s using the feedwater gap area from Section 3.2. The Reynolds number is defined as

$$Re = \frac{\rho v L}{\mu} = 1.5 \tag{4.6}$$

where v is the feedwater flow rate calculated from historical mass flow rates using the continuity equation:

$$v = \frac{\dot{m}}{\rho A} = \frac{0.005\ kg/s}{998/kg/m^3 * 0.005/m^3} \approx 0.001 m/s$$

and ρ is the density of the feedwater (998 kg/m^3), μ is the viscosity of water (assumed to be 0.001 $Pa \cdot s$), and L is the characteristic length (1.5 mm), in this case the thickness of the feedwater gap. After the transient start-up period when the feedwater spreads through the whole area of the feedwater gap, the feedwater is moving across its thickness (not its length or width). With a Reynolds number of 1.5, the feedwater is creeping rather than flowing and the feedwater gap can be treated as another conductive "layer" of the sublimator. It should be noted that, based on conversations with thermo-fluid engineers at NASA Johnson Space Center and partner organizations, capillary actions is not typically used to describe the feedwater flow through the gap and porous media. It is thought that pressure-driven flow (feedwater pressure versus vacuum) has a greater impact on the flow than capillary action [64, 65]. During start-up, capillarity may play a role but not during steady-state sublimator operations because there is no free surface - the porous medium is full of liquid water up until the ice barrier.

The next two sections are concerned with the two modeling approaches: (1) conduction (the "inside-out" perspective) and (2) rarefied diffusion through porous media (the "outside-in" perspective), both of which are required to obtain realizable ranges for ice thickness and location. The ice thickness and formation location are determined from both the "inside-out"— because the ice thickness depends on heat flux from the source and conduction through the sublimator structure, and from the "outside-in"— because the location of ice depends on pressure drop in the vapor space.

4.5 Conduction Model (Temperature)

As discussed in Section 1.3, the heat flux determines the sublimation rate (Equation 1.4) and the sublimation rate is used to determine the pressure drop. The heat flux and conduction through the sublimator structure determines the limits of the ice thickness layer from the "inside-out". Figure 4.2 is shown again for reference.

Steady-state, one-dimensional conduction through ice embedded in porous media is:

$$q" = \frac{k_{eff_{PM,ice}}}{l_{ice}} (T_{ls} - T_{sv}) \tag{4.7}$$

where q" is the heat flux from the heat source (W/m^2), $k_{eff_{PM,ice}}$ is the effective thermal conductivity of the combined ice/porous media ($W/m°C$), l_{ice} is the ice layer thickness (m), T_{ls} is the liquid-ice interface temperature ($0°C$), and T_{sv} is the solid-vapor interface temperature ($°C$).

A first order approximation of the effective thermal conductivity is used [66, 67]:

$$k_{eff_{PM,ice}} = \phi k_{ice} + (1 - \phi) k_{ss} \tag{4.8}$$

where ϕ is porosity, $k_{ice} = 2.22\ W/m°C$ is the thermal conductivity of ice at $0°C$ and $k_{ss} = 16.3\ W/m°C$ is the thermal conductivity of 316L stainless steel [17].

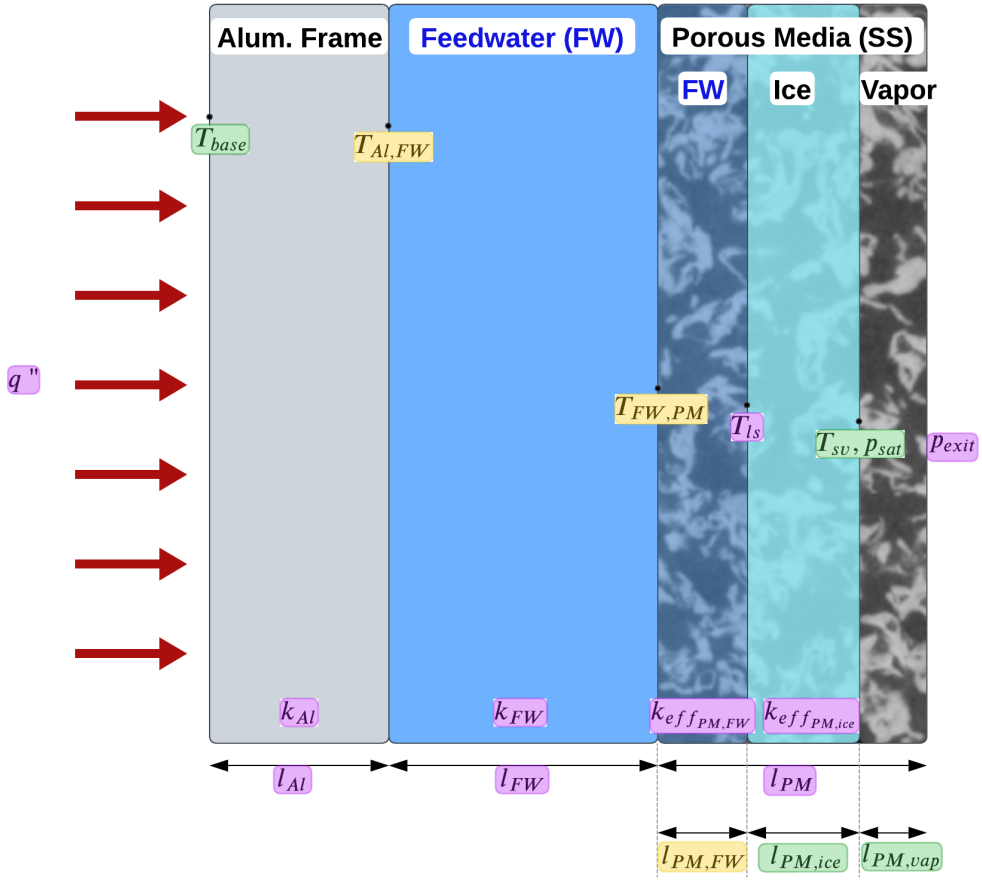

Figure 4.2: The "layers" of a sublimator oriented with the heat source to the left of the figure and the vacuum of space to the right of the figure.

Section 5.1.1 discusses the effective thermal conductivity computed using a numerical analysis software, Porous Microstructure Analysis (PuMA) to estimate the effective thermal

conductivity with greater accuracy, but those values are not yet validated. From Equation 4.7, it is evident that the higher the heat flux, the smaller the ice layer thickness and the colder the sublimation interface must be to maintain a non-zero ice layer thickness. Figure 4.7 is a graphical representation of the relationship presented in Equation 4.7. Sublimation interface temperature, T_{sv} is a funciton of both the ice layer thickness and heat flux. Note that the ice layer thickness input is limited by the overall thickness of the porous medium (1.5mm).

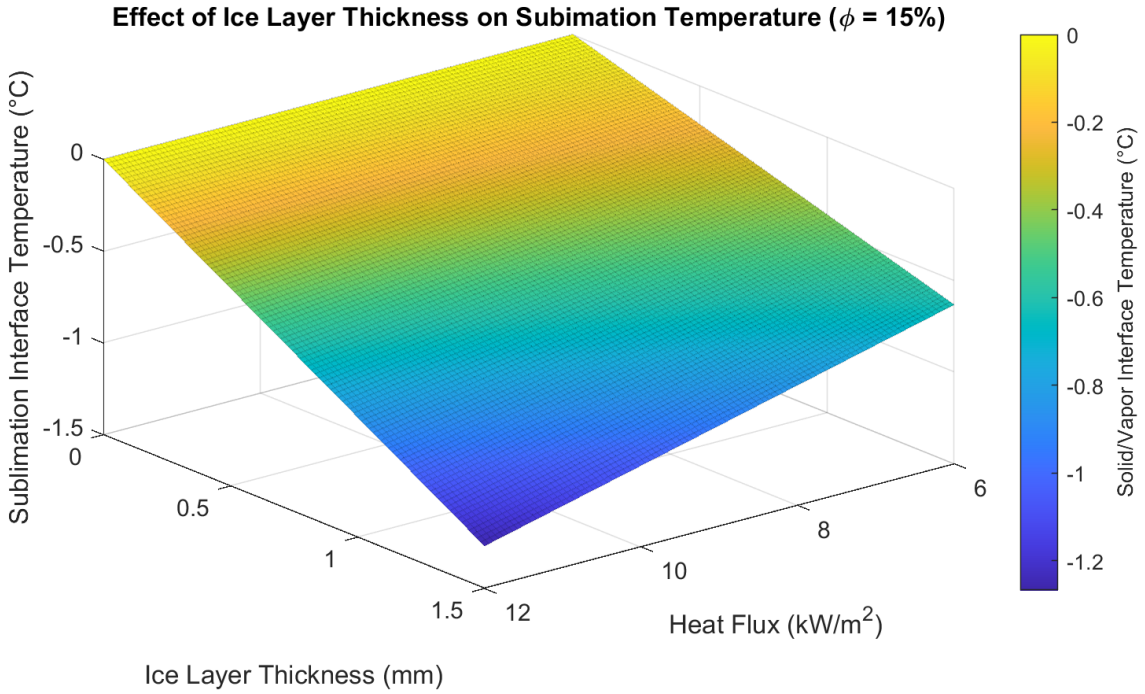

Figure 4.7: Relationship between ice layer thickness, heat flux from the source, and solid-vapor interface temperature for sublimation in a porous media with 15% porosity.

For the sublimation case (excluding evaporation), the **plausible temperature range for the solid-vapor interface is small**. Even if $\phi = 50\%$, the sublimation temperature range is $-2°C \leq T_{sv} \leq 0°C$. If the sublimation temperature drops any lower, the ice thickness would surpass the thickness of the porous medium. In Section 4.2, the second historical assumption about the sublimation temperature of ice is correct (the ice sublimates at a temperature just below the triple point of water). Rather than solving for all the unknown variables simultaneously, the equations are solved sequentially with T_{sv} chosen within this plausible range.

Equation 4.7 is re-written to solve for the ice thickness based on incoming heat flux:

$$l_{PM,ice} = \frac{k_{eff_{PM,ice}}}{q"} (T_{ls} - T_{sv}) \tag{4.9}$$

The thickness of the feedwater region within the porous medium (before the freezing interface) is solved using $l_{PM,ice}$ in:

$$l_{PM,FW} = l_{PM} - l_{PM,ice} - l_{PM,vap} \tag{4.10}$$

where l_{PM} is the chosen porous component thickness and $l_{PM,vap}$ is solved for using the Weber equation introduced in Section 4.6.2.3. The temperature of the feedwater gap/porous media interface is solved using $l_{pm,FW}$ in:

$$T_{FW,PM} = T_{ls} + \frac{q"l_{PM,FW}}{k_{eff_{PM,FW}}} \tag{4.11}$$

which in turn is used to determine the temperature of the aluminum frame/feedwater gap interface with

$$T_{Al,FW} = T_{FW,PM} + \frac{q"l_{FW}}{k_{FW}} \tag{4.12}$$

Lastly, the temperature of the heat source, assumed to be the temperature of the outer edge of the aluminum base (leftmost edge in Figure 4.2) is

$$T_{base} = T_{Al,FW} + \frac{q"l_{Al}}{k_{Al}} \tag{4.13}$$

A larger heat flux decreases the chance of ice forming and being maintained in the porous medium. Section 1.3 provided more details about the conditions in which ice may be present. It is widely accepted that the feedwater gap is above freezing, or else the *entire* feedwater gap would turn to ice, expand, and break the sublimator hardware [16, 19]. If the feedwater gap is above freezing, then the temperature gradient through the sublimator "layers" *must* yield *above-freezing* temperatures in the feedwater gap and *just below-freezing* temperatures within the porous medium when ice is present. The sublimation process helps cool the solid/vapor interface to maintain the ice layer while the feedwater gap remains liquid water.

4.6 Mass Flow Model (Pressure)

Conduction through the porous medium is part of the picture, and describing the water vapor diffusion through the porous medium completes the model. A model of this type of flow, also referred to as self-diffusion, will determine the "thickness" of the vapor layer (i.e. the location of the sublimation or evaporation interface) from the "outside-in".

4.6.1 Evaporation/Sublimation Rate Limit

Before a detailed model of vapor diffusion through a porous media is developed, sublimation in general, as well as the mechanisms which drive sublimation rate, should be understood. For phase change within the sublimator (liquid-solid-vapor), heat transfer rate, (q, W) is expressed as Equation 1.4:

$$q = \dot{m} h_{lv}$$

where $\dot{m}$ is the mass flow in kg/s and h_{lv} is the latent heat of vaporization for water in J/kg. Simply put, "sublimation occurs at a rate proportional to the heat load" [26]. The heat load is known from the waste heat generation of the CubeSat, so the water vapor mass flow may be obtained if this process occurs under constant pressure such as the vacuum of space. *However, since the sublimation process occurs within the porous medium, the pressure at the sublimation interface may not be constant nor a perfect vacuum due to vapor flow resistance near the phase change interface.* The porous medium restricts the vapor flow and the sublimation rate. In addition, the temperature of the porous medium dictates the temperature of the water within the pores, as demonstrated in Section 4.4, so the phase change process may not occur precisely at the triple point temperature. Similar to the processes in which ice sublimates on comets and moves through porous rock, the Hertz-Knudsen equation is used here as a baseline sublimation rate, in units of mass flux rate ($kg/s/m^2$) [68]:

$$\frac{\dot{m}}{A} = \alpha \sqrt{\frac{M_{H_2O}}{2\pi RT}} * (p_{sat} - p) \tag{4.14}$$

where α is the "sticking coefficient", an empirical term first added by Knudsen to correlate Equation 4.14 with experimental data [68, 69], M_{H_2O} is the molar mass of water (0.01801 kg/mol), R is the universal gas constant (8.3145 $J/mol/K$), and T and p are the temperature (K) and pressure (Pa), respectively, at the sublimation surface. p_{sat} is the saturation pressure (Pa) as a function of T according to the Clausius-Clapeyron equation [23]:

$$p_{sat} = p_{tp} * exp\left[-\frac{h_{lv} M_{H_2O}}{R}\left(\frac{1}{T} - \frac{1}{T_{tp}}\right)\right] \tag{4.15}$$

where p_{tp} and T_{tp} are the triple point reference pressure (Pa) and temperature (K), respectively. As Equations 4.14 and 4.15 indicate, the mass flux rate is dependent on both the temperature and pressure at the phase change interface which are independently varied in Figure 4.8. Note that the units of temperature used in this plot are Celsius and not Kelvin to make the graph more intuitive. As the temperature at the sublimation interface increases, so does p_{sat} and so does the sublimation rate limit. The Hertz-Knudsen equation also describes the exothermic phase change processes (condensation or deposition), indicated by the section of the surface plot below the flat plane in Figure 4.8. Even though Equation 4.14 serves as a baseline, the temperature-mass flux connection provides a mathematical relationship for this widely accepted explanation: as the heat flux into the sublimator increases, mass flux rate increases. This helps maintain a relatively stable and self-regulating temperature at the heat source, causing the sublimator to function as a robust means of heat rejection across a range of heat fluxes. Note that the baseline sublimation rate in Equation 4.14 is independent of the ice layer thickness.

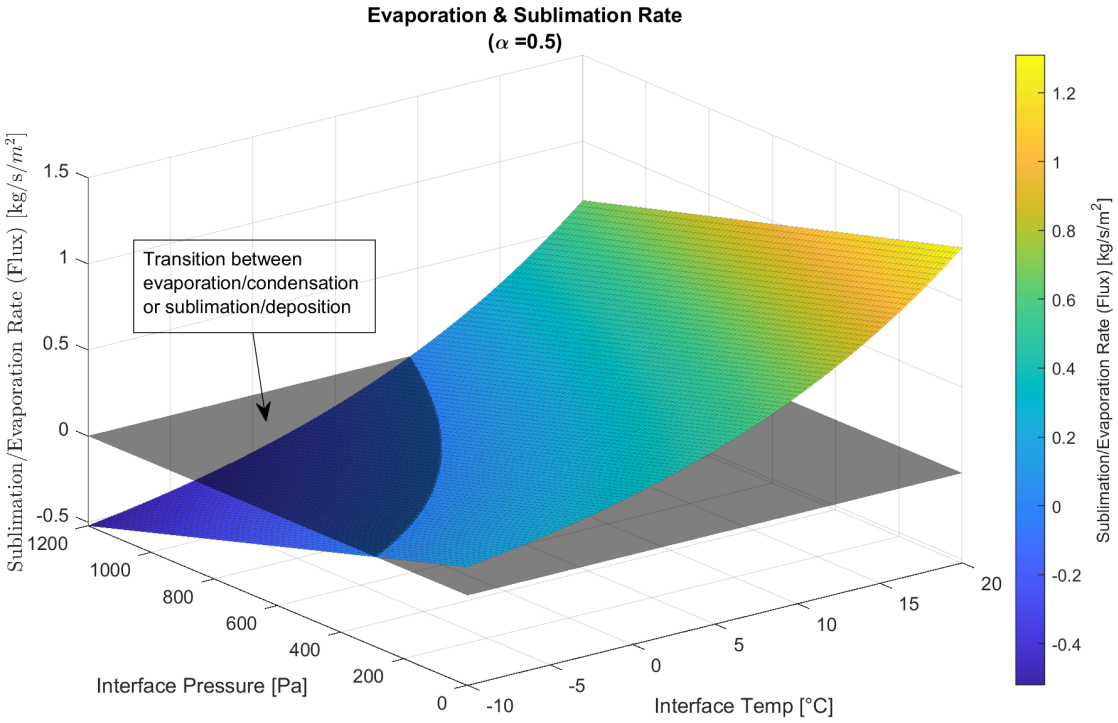

Figure 4.8: Sublimation/evaporation rate using the Hertz-Knudsen equation and based on interface temperature and pressure.

To create continuity between the historical sublimator models/experiments and the current work, the sublimation mass flux from a number of sources was compared to the Hertz-Knudsen equation in Figure 4.9. It should be noted that most models and experiments assume the sublimation interface is just below the triple point temperature of water, so all data points were plotted at $0°C$. The sticking coefficient used here was $\alpha = 0.15$ [68]. This exercise verifies that the Hertz-Knudsen equation is reasonable for a baseline of temperature-dependent sublimation rate and helps visualize past sublimation rate data for comparison to future model results. Most of the historical values were below the Hertz-Knudsen equation prediction, which implies that there is some other factor causing a reduced sublimation/evaporation rate (i.e. flow resistance in the porous medium). There are two explanations for the data points above the Hertz-Knudsen line: first, the choice of sticking coefficient is still an active area of research so it may be closer to unity in some cases, yielding a Hertz-Knudsen line above *all* of the data. And second, the porosity was often assumed to be $\phi = 0.07$ if this parameter was not available so there may be some porous media with

a more compact microporous structure which would yield a lower mass flux than estimated here.

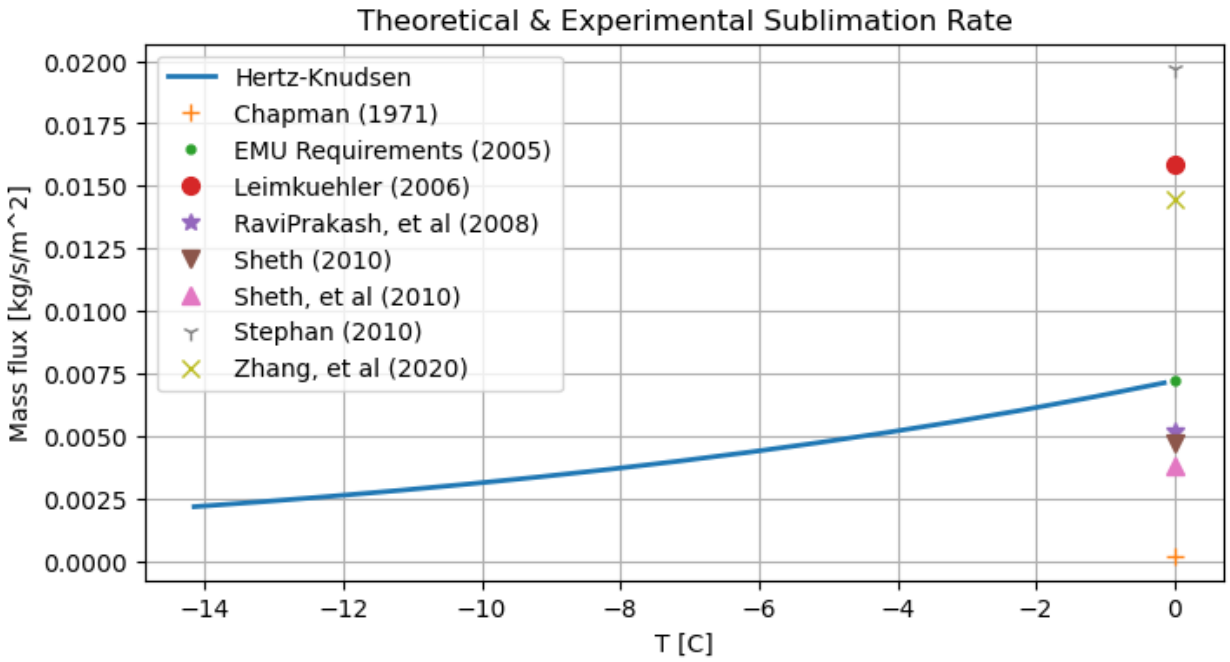

Figure 4.9: Historical sublimation (mass flux) compared to the Hertz-Knudsen equation.

A more realistic sublimation rate must incorporate the effect of the porous medium on the water vapor behavior. The reduced sublimation rate depends on the water vapor pressure at the ice/vapor interface which is dictated by rarefication effects and the permeability of the porous medium to vapor flow.

4.6.2 Scaling of Evaporation/Sublimation Rate

The evaporation/sublimation rate is scaled down from the Hertz-Knudzen equation because the water vapor must travel through porous media before exiting the sublimator to vacuum. In order to understand how the sublimation rate is scaled, porous media is described using physical characteristics, then a brief overview of flow regimes and their classification is discussed and finally, flow through porous media is modeled.

4.6.2.1 Porous Media

Common examples of porous media include dish washing sponges, soil, filters, and even human skin and hair. The porous medium in a sublimator is sintered stainless steel which does not absorb or adsorb any fluid. In the sintering process, metal "powder" or flakes are heated and compressed together. Bonds are formed between the particles but they are not heated to the point of liquification. The geometry of the porous component in a sublimator is described by a number of physical parameters, called the porous microstructure because the pores are on the micro-scale. Figure 4.10 shows a 3D model of the scanned porous samples used in this research via the Dragonfly software for 3D x-ray image analysis and the Porous Microstructure Analyzer (PuMA) software; see Section 5.1 for more details [70, 71]. In this figure it is quite evident how tortuous the porous microstructure appears: there is a wide range of the size of pores and connections between pores. The smooth appearance of the sides of the sample are from the cropped 3D image, they are not a physical feature.

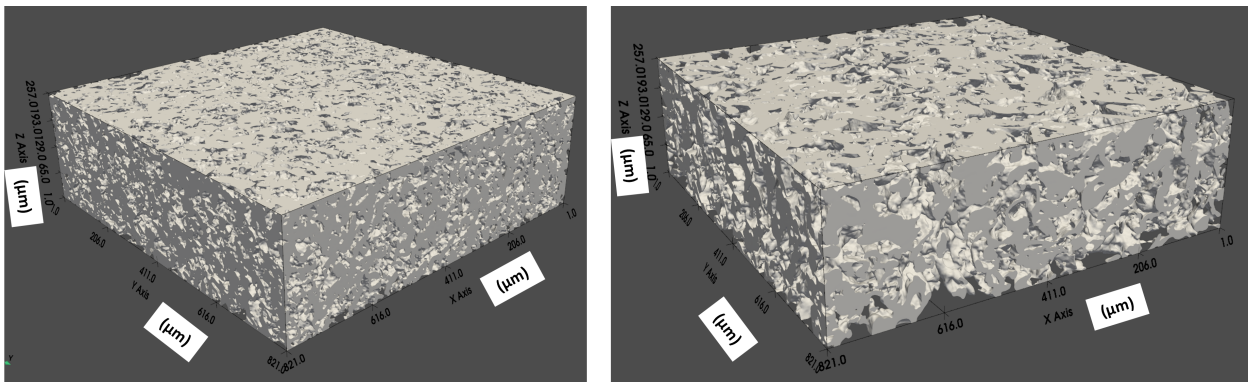

Figure 4.10: 3D Rendering of X-ray tomography scan of porous samples from Mott Corp using Dragonfly and PuMA software with reported pore sizes of 40 μm (left) and 100 μm (right) [70–72].

Porosity (ϕ): the fraction of void space in a porous media volume. For example if a porous component has $\phi = 15\%$, then 85% of the volume is occupied by the solid material and 15% is empty space through which a substance may flow. During the sintering process, porosity is loosely controlled by the amount of compression applied to the metal flakes, as well as their individual size, and is straightforward to measure after manufacturing is complete.

Pore Size (r, d): the radius or diameter of the pores influences the flow and heat

transfer phenomena. Pore size is not directly measured; in a sintered metal porous media it is controlled by the size of the flakes/metal particulate. The bubble point test is an indirect measurement of pore size. The porous medium is wetted with a wetting fluid such as isopropyl alcohol and as gas is flowed from one side, bubbles begin to form. The relationship between pressure required to form the first bubble and pore size is given by the Young-Laplace Equation: $p = \frac{4K\sigma cos\theta}{d}$ where p is the pressure applied through the filter (from the gas flow), K is a shape correction factor, σ is surface tension, θ is the liquid-solid contact angle, and d is the pore diameter. This equation is not used again in this thesis so further discussion can be found in Carey's textbook [73] and in Scott's Handbook [74]. The location and size of the *largest* pore are obtained from this test and manufacturers report either the largest pore size or a range of pore sizes based on the size of metal particulate used [72, 75]. Section 5.1 discusses discrepancies between reported and estimated pore size in more detail.

Thermal Conductivity (k_{eff}): the porous medium's effective thermal conductivity is a function of the metal's conductivity and, in the case when the void space is filled with a substance, the conductivity of the filling substance. The thermal conductivity thus depends on porosity, pore size, and tortuosity and its calculation is discussed at length in Sections 4.4 and 5.1.1.

Hydrophobicity/Hydrophilicity: hydrophobicity is a material's aversion to water and hydrophilicity is a material's affinity to water. These characteristics were not the focus of this research, but the movement of the liquid water through the porous medium, especially during transient start-up, could be improved by a hydrophilic coating, if need be. Most researchers assert that the porous medium plays a role in restraining the liquid water via surface tension [15, 21], although some disagree because the contact angle between metal and water is close to 90° [73]. This phenomena has not been explicitly studied and published.

Isotropicity: the porous medium in question is isotropic in that it is not patterned in any specific direction so each of its physical values are direction-independent. Because the porous medium is isotropic, vapor will exhibit the same diffusive behavior in every direction. Diffusion in only the z-direction (through the depth of the porous medium) will be modeled.

Tortuosity (η): the path a single molecules takes to get from one side of the porous medium to the other is longer than a straight-line path. Tortuosity cannot be directly

measured and depends on the microstrucutre of the porous medium and the flow regime, discussed in the next section. There are three types of tortuosity: geometric, hydraulic, and diffusion [76, 77]. Geometric tortuosity is the "ratio between the shortest path length through the porous medium and the straight-line path" [78]. It is defined as

$$\eta = \frac{L_{eff}}{L_{ref}} \tag{4.16}$$

where L_{eff} is the length of the path traveled by a molecule (m) and L_{ref} is the length of a straight flow path (i.e. thickness of porous media, m). Hydraulic tortuosity is the ratio of the length of the flow path and the straight-line path and is not easily defined for flow in the rarefied regime [76]. Diffusive tortuosity (which is also used to describe conductive tortuosity) is conceptualized as the degree to which a porous media is resistant to diffusion or conduction [78]:

$$\eta = \phi \left(\frac{D_{ref}}{D_{eff}} \right) \tag{4.17}$$

where D_{ref} is the diffusion coefficient, (in this case in m^2/s) if the porous medium consisted of straight flow paths D_{eff} is the real diffusion coefficient of the tortuous porous media in m^2/s. Some research has suggested that Equations 4.16 and 4.17 are interchangeable [79] because the relationship between mean-squared displacement (MSD), path length, and diffusion is $MSD = 2Dt$ and represented graphically as the blue line in Figure 4.11. An increase in diffusion is characterized by an increase in particle displacement, so in this regard geometric and diffusive tortuosity may be interchangeable. In Equation 4.16, the ratio between the effective and reference lengths is proportional to the *inverse ratio* between the effective and reference diffusion coefficients in Equation 4.17. The more tortuous the porous medium, the smaller the diffusion coefficient because the substance faces increased resistance. The calculations for diffusion depend on flow regime and are discussed in detail in Section 4.7.1.

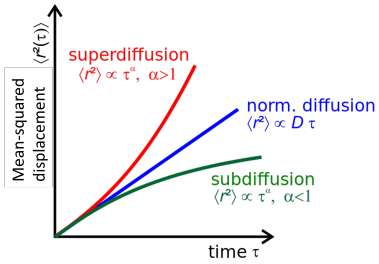

Figure 4.11: Relationship between mean-squared displacement (MSD) and the diffusion coefficient [80]

Other researchers, however, state that the geometric and diffusive tortuosity values are not interchangeable and are, in fact, separate concepts altogether [78, 81]. More specifically, diffusive tortuosity can be four times greater than geometric tortuosity for porous media with low porosity ($< 15\%$) [77, 81]. The geometric and diffusive tortuosity definitions grow closer in value as porosity increases. Geometric, hydraulic, and diffusional tortuosity characteristics may be related semi-empirically but not analytically. The tortuosity obtained using PuMA software is calculated from the diffusion coefficients and is discussed more in Section 5.1.1. While the diffusion tortuosity values from PuMA cannot be used directly in place of geometric tortuosity, an approximate substitution will be used for the tube length variable, l, in the Weber equation (Eqs. 4.20-4.23) and discussed further in the following pages.

4.6.2.2 Flow Regimes

Flow regime is determined by Knudsen number:

$$Kn = \frac{\lambda}{r} \tag{4.18}$$

where r is the characteristic length, which is not standardized - it can be either the pore radius or pore diameter. The pore radius or diameter in a porous medium often varies widely; sometimes the average value is used and at other times the largest pore size is used. In this research, characteristic length is treated as the average pore radius ($1 - 5\ \mu m$). λ is the mean free path (MFP) of a water molecule, or the average distance a molecule will travel before changing direction due to collision with another molecule. The MFP is defined as

$$\lambda = \frac{k_B T}{\sqrt{2}\pi d_{H_2O}^2 \, p} \tag{4.19}$$

where k_B is the Boltzmann Constant ($1.38 * 10^{-23} J/K/molec$) [82], T is the temperature of the molecule (K), d_{H_2O} is the diameter of a water molecule (m). p is the pressure which, in the porous medium, is the average between the inlet and outlet pressure of the vapor space. The larger the Knudsen number, the more rarefied the flow because there is a smaller concentration of molecules in a given volume. Rarefied flow is associated with a lower pressure, as in the case of water vapor in the sublimator porous media exposed to vacuum. Figure 4.12 and Table 4.1 show the categorization of Knudsen number and flow regime; these values are a general guideline but not a strict law. In rarefied, or free molecular flow, the molecules are more likely to collide with a pore wall than with another molecule.

Table 4.1: Knudsen Number and flow regimes [83].

Knudsen Number	Flow Regime
$Kn \leq 0.001$	Continuum
$0.001 < Kn \leq 0.1$	Slip
$0.1 < Kn \leq 10$	Transition
$10 < Kn$	Free Molecular/Rarefied

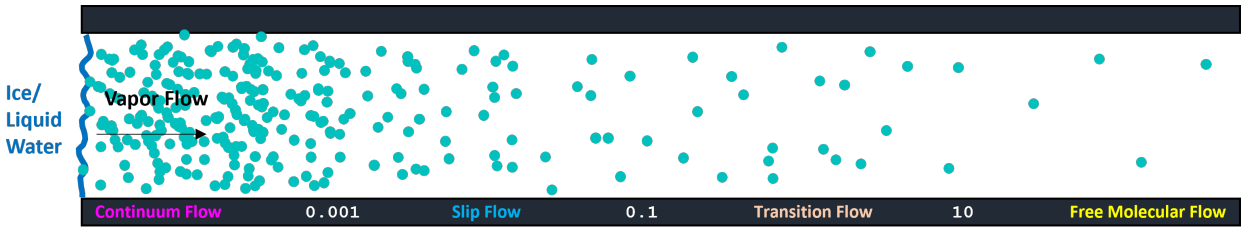

Figure 4.12: Knudsen Number flow regime and visualization (not to scale).

According to the Knudsen number definition, the larger the characteristic length, the smaller the Knudsen number and the more viscous the flow, and vice versa. In general, the larger the temperature, the larger the Knudsen number (the more rarefied the flow), but categorizing the water vapor flow in a sublimator is a unique scenario. In the MFP calculation, the temperature and pressure are intertwined because the upstream side of the flow is at saturation conditions (either sublimation or evaporation). When the saturation temperature – in the numerator of Equation 4.19 – increases, the saturation pressure – in

the denominator – decreases. Temperature and pressure are related in a nonlinear way via the Clausius-Clapeyron equation, Eq. 4.15. Figure 4.13 shows how the Knudsen number increases with a *decrease* in both pressure and pore radius. For example, if the sublimation interface is at $T_{sat} = 0°C$ and $p_{sat} = 611\ Pa$, the mean free path of the water vapor will be $\lambda = 20\ \mu m$, which yields a Knudsen number range of $4 < Kn < 20$ for a pore radius range in $1 < r < 5\ \mu m$.

The water vapor flow will be in the transition regime only in the case of evaporation where the saturation pressure is $\geq 1kPa$ and the pores are relatively large. In all other instances, the flow is in the rarefied/molecular regime. In Figure 4.13, the transition/rarefied flow regime is differentiated by the horizontal plane. Even though Figure 4.13 shows a distinct separation between the transition and rarefied regimes, it is generally not this clear. The Weber equation discussed in the next section can help model water vapor behavior, especially near the limits of one or the other flow regime.

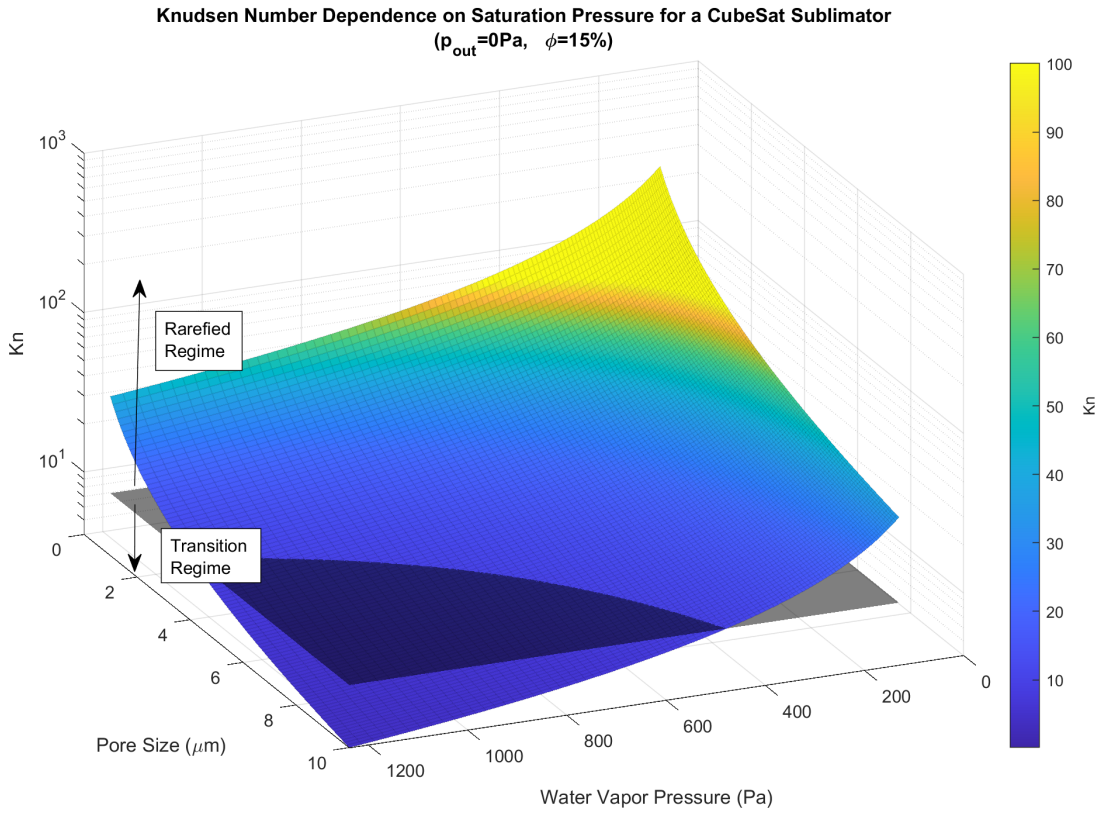

Figure 4.13: Relationship between Knudsen number, pore radius, and pressure for an example CubeSat sublimator porous media. The grey plane represents the boundary between the rarefied and transition flow regimes.

4.6.2.3 Modeling Flow through Porous Media

When a flow is no longer in the continuum regime, as in flow through micro-porous media with large Knudsen numbers, the transition or rarefied regime may be modeled numerically via stochastic models such as direct simulation Monte Carlo (DSMC) or via deterministic approaches such as molecular dynamics [83]. Another approach is the Dusty Gas Model (DGM) in which the porous medium is modeled as another very large molecule, "dust", held in physical space by an invisible external force and the diffusing gas moves around the large particles [84, 85]. The DGM incorporates physical parameters for the porous medium such as porosity and tortuosity [86]. Each of these approaches to modeling rarefied flow (diffusion) in porous media are extensive stand-alone research topics, so they are not the focus of this thesis.

Flow through porous media can also be idealized by treating the porous medium as a bundle of capillary tubes , as shown in Figure 4.14. This approach was first used to describe capillary imbibition of a slow-moving liquid in soils [87] and was extended to rarefied flow [25, 88–90]. The treatment of a porous media as a bundle of long, thin capillary tubes is used to analyze the relationship between pressure drop and mass flow rate.

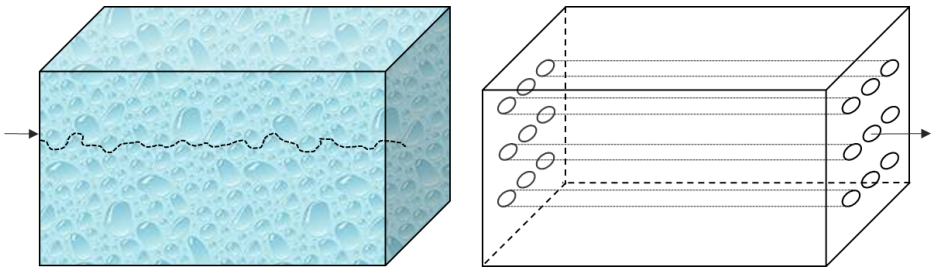

Figure 4.14: Visualization of porous media (left) as a bundle of capillary tubes (right).

When porous media is modeled as a bundle of capillary tubes, the Weber equation is used to model the molecular flow rate "normalized" by the pressure drop for a vapor through a capillary tube at *any* flow regime over the full range of Knudsen numbers [91]. This analytical relationship has been validated with data over all Knudsen numbers in past experimental tests [90–92]. The Weber equation assumes that the substance is an ideal gas (explored at length in Section 5.2.4.1) and that there is no adsorption into the porous structure. The Weber equation will be used in this research and validated with experimental data (see

Chapter 5) to analytically show the relationship between mass flow rate, pressure drop, absolute pressure, pore size, and temperature. The Weber equation is:

$$\frac{\dot{n}}{\Delta p} = \frac{4}{3}\sqrt{\frac{2\pi}{m_{H_2O}k_BT}} * \frac{r^3}{l\tau}\left[\frac{3\pi}{128}\left(\frac{2r}{\lambda}\right) + \frac{\pi}{4}\left(\frac{2r/\lambda}{1+2r/\lambda}\right) + \left(\frac{1}{1+2r/\lambda}\right)\right] \tag{4.20}$$

Where $\dot{n}$ is the molecular flow rate (molec/s), Δp is the pressure drop across the tube (Pa), m_{H_2O} is the molecular mass of water (kg/molec), k_B is the Boltzmann Constant previously defined, T is the temperature of the gas (K), r is the radius of the tube (m), also assumed to be the radius of a pore, and l is the tube length which may also incorporate geometric tortuosity scaling (m). The tube length was scaled by a tortuosity factor of $\tau = 2$, as described in Section 5.1. The last three terms of Equation 4.20 incorporate the inverse Knudsen number (r/λ) and can be re-written as

$$\frac{\dot{n}}{\Delta p} = \frac{4}{3}\sqrt{\frac{2\pi}{m_{H_2O}k_BT}} * \frac{r^3}{l\tau}\left[N_1 + N_2 + N_3\right] \tag{4.21}$$

where N_1, N_2, N_3 can be thought of as weights designated for three distinct flow regimes (the weights do not sum to 1) [91, 92]. N_1 is representative of continuum flow and is derived from Poiseuille flow through a long tube [22]. N_2 is representative of slip flow, or the phenomena first explored by Navier in which the non-continuum gas molecules have a non-zero velocity at the wall [93]. N_2 is derived from Maxwell's mathematical model of the slip condition for rarefied gases via the kinetic theory of gases [22, 94]. N_3 is representative of rarefied flow, or the contribution from self-diffusion (also referred to as Knudsen diffusion), derived from the kinetic theory of gases [94]. The transition regime does not have a designated coefficient; its weight is incorporated in both N_2 and N_3.

Because the water vapor diffusion through the sublimator porous media is almost entirely in the rarefied regime, the N_3 coefficient is close to 1, N_2 is close to 0.1, and N_1 is near 0.01. Equations 4.20 and 4.21 show the *molecular* flow rate for a *single capillary tube*, but they can be modified to show the *mass* flow rate for the entire cross-sectional area of porous media by multiplying the equation by the molecular mass of water m_{H_2O} and multiplying the mass flow rate by the number of capillary tubes used to approximate the porous medium:

$$\eta_{tubes} = \frac{A_{tot}\phi}{\pi r^2} \tag{4.22}$$

where $A_{tot}\phi$ is the *open* cross-sectional flow area (m^2) and πr^2 is the cross-sectional flow area of a single capillary tube (m^2). The Weber equation then becomes

$$\frac{\dot{m}}{\Delta p} = \frac{4}{3}\sqrt{\frac{2m_{H_2O}}{\pi k_B T}} * \frac{r}{l\tau} A_{tot}\phi \left[N_1 + N_2 + N_3\right] \tag{4.23}$$

Figure 4.15 shows the relationship between Knudsen number and the mass flow rate ratio. The Weber equation does not capture the Knudsen paradox in which the mass flow rate at $Kn > 0.8$ increases *slightly* with a decrease in pressure (increased rarification). This is explored at length in Section 4.7.1. The Knudsen paradox can be captured numerically and experimentally, but not analytically with the Weber equation. It is observed or numerically reproduced at scales which could not be captured or detected experimentally in this research.

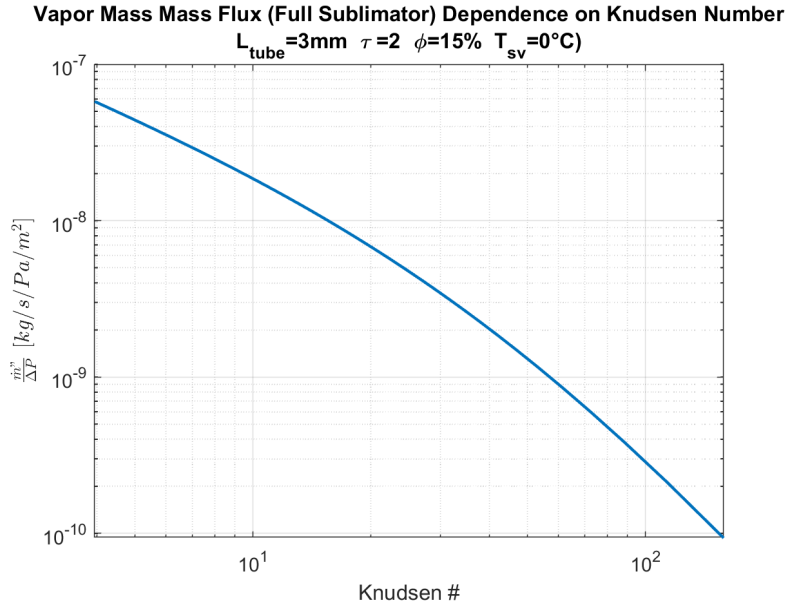

Figure 4.15: Relationship between Knudsen number and mass flow rate normalized by pressure drop and area, based on the Weber equation for molecular and transition flow.

For both the sublimation and evaporation modes, the Weber equation is used to predict the thickness of the vapor region in the porous medium using Equation 4.20 rearranged to solve for vapor diffusion distance:

$$l = \frac{1}{\tau}\frac{\Delta p}{\dot{m}} * \frac{4}{3}\sqrt{\frac{2m_{H_2O}}{\pi k_B T}} * rA_{tot}\phi \left[\frac{3\pi}{128}\left(\frac{2r}{\lambda}\right) + \frac{\pi}{4}\left(\frac{2r/\lambda}{1+2r/\lambda}\right) + \left(\frac{1}{1+2r/\lambda}\right)\right] \tag{4.24}$$

In Figure 4.16, the vertical plane shows the minimum realizable sublimation interface temperature ($T_{sv} = -2°C$) from Section 4.5 and each of the four surface plots represents a different heat flux. The outlet pressure was a vacuum and the inlet pressure was determined by the saturation temperature. The range of pore sizes and heat fluxes were chosen based on historical data in the literature review, and the mass flow rate was calculated from the heat fluxes using the phase change heat transfer equation (Eq. 1.4). In the realizable sublimation temperature range, the vapor region thickness is dependent on both T_{sv} and r. This thickness becomes more dependent on temperature with an increase in pore size.

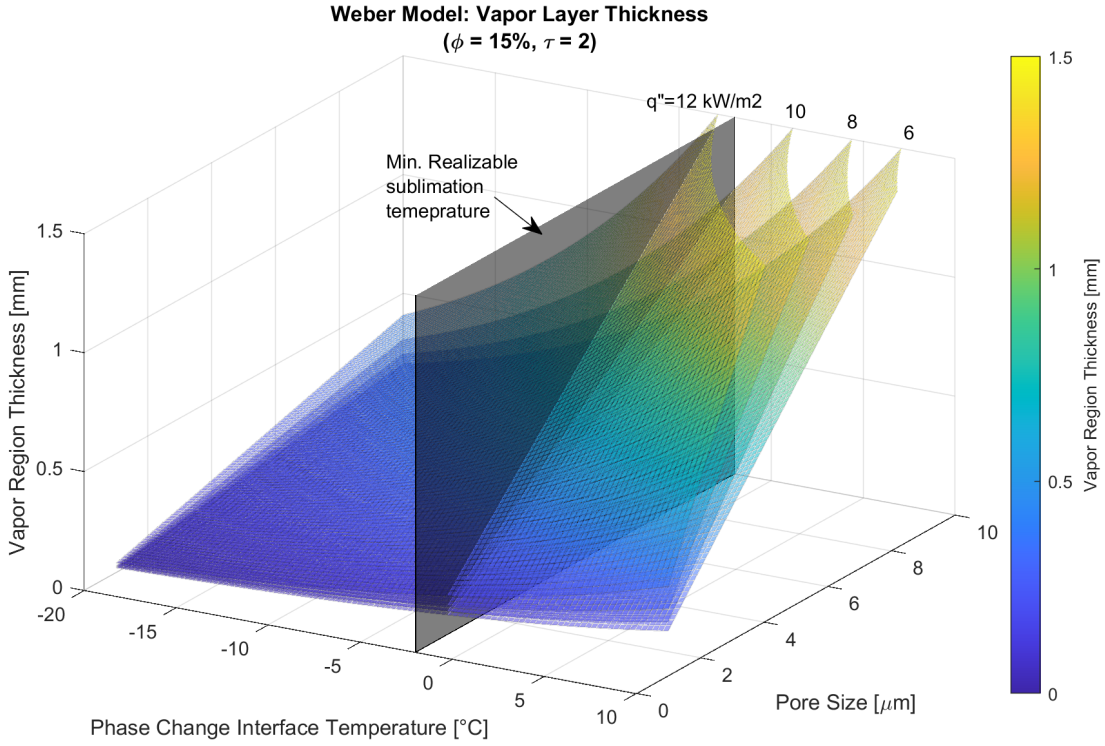

Figure 4.16: Relationship between vapor region thickness, phase change interface temperature, pore size, and heat flux for a porous media with $\phi = 15\%$. The four surfaces represent four different heat fluxes, from top to bottom: $q" = 12,\ 10,\ 8,\ 6\ kW/m^2$.

In Section 4.8, the Weber equation will be combined with the conduction equations to produce a temperature and pressure prediction for a sublimator based on a series of inputs.

4.7 Evaporation in the Sublimator

4.7.1 Evaporation Mode

If the temperature of the porous medium is always above freezing and the rate phase change of the liquid/vapor is never high enough to cool the interface below freezing, then evaporation may occur. In the evaporation mode, the same amount of heat as in the sublimation mode may be transferred via the phase change heat transfer equation, as discussed in Section 1.3. Without the presence of an ice layer, there is a continuous pressure drop through the liquid water and the water vapor within the porous medium. In the porous medium, the connection between the $\Delta p - \dot{m}$ relationship in the liquid region and the $\Delta p - \dot{m}$ relationship in the vapor region indicates the evaporation location. This location is a determining factor in realizable design parameters for the sublimator, such as porous media thickness, pore size, and porosity. There are two approaches used in this section to illustrate the relationship between the liquid feedwater entering the porous medium and the water vapor exiting into the vacuum of space. The first approach inspects the **pressure** exerted on the liquid feedwater by the newly evaporated water vapor. The second approach qualitatively and quantitatively compares the **permeability** coefficients of the porous medium to liquid water and water vapor.

4.7.1.1 Comparison of Pressures

It is widely accepted that the porous medium contributes to resistance to flow by (1) holding back the liquid water during the sublimator start-up stage, (2) providing a microstructure in which ice may form and (3) providing a microstructure in which water vapor lingers. The level to which lingering water vapor contributes to resistance to flow is explored by comparing the pressure of the incoming feedwater to the water vapor pressure at the evaporation interface. The water vapor pressure immediately downstream of the feedwater in the porous medium is non-zero (i.e. not at a complete vacuum). It is near saturation pressure, as determined by the temperature of the porous medium structure (see Section 4.4). Feedwater pressure ranges from $7 - 28\ kPa$ $(1 - 4\ psia)$ [16, 42, 43, 45, 46]. Table 4.2 quantitatively compares sample feedwater and water vapor pressures to demonstrate the degree to which lingering

water vapor restricts feedwater flow.

Table 4.2: Percentage reduction in pressure-driven nature of flow due to water vapor pressure.

T_{PM} [°C]	p_{vap}=p_{sat} [Pa]	% of p_{FW} [7 kPa]	% of p_{FW} [14 kPa]	% of p_{FW} [21 kPa]	% of p_{FW} [28 kPa]
0	0.613	9%	4%	3%	2%
2	0.707	10%	5%	3%	3%
4	0.813	12%	6%	4%	3%
6	0.935	13%	7%	4%	3%
8	1.072	15%	8%	5%	4%
10	1.227	18%	9%	6%	4%
12	1.402	20%	10%	7%	5%
14	1.598	23%	11%	8%	6%
16	1.818	26%	13%	9%	6%
18	2.065	30%	15%	10%	7%
20	2.340	33%	17%	11%	8%

In Table 4.2, the colored columns represent sample feedwater pressures based on the historical range from $7 - 28$ kPa. Each row designates a possible saturation temperature/pressure combination at the evaporation interface as indicated in columns 1 and 2. Column 2 assumes the water vapor downstream of the evaporation interface is at saturation pressure (i.e. it *just* evaporated). For example, if incoming feedwater is at 21 kPa (column 5), the evaporation interface is at $T_{PM} = 2°C$ (row 3), and the vapor pressure at the phase change interface is 0.707 kPa, then the water vapor "pushes" against the incoming feedwater with 3% of the feedwater pressure.

Sublimators, in the evaporation mode, are still expected to function near the triple point of water, so the most realistic cases are for $T_{PM} < 6°C$ where the water vapor pressure restricts the pressure drop experienced by the feedwater by up to 12%. This table illustrates that the **water vapor does not contribute a significant pressure resistance to flow of the liquid feedwater**. Using only a pressure comparison, one could argue that the evaporation interface is near the outer edge of the porous medium because the feedwater is not "held back" by the water vapor in any meaningful way. A comparison of the liquid and vapor pressures is not indicative of a resistance to flow, but it should be noted that the porous medium does play a role in restraining the liquid water via surface tension and

viscous friction, although the level to which this occurs is not quantified in this research [15, 21]. A comparison of the permeability coefficients of water and vapor is a better indicator of the relationship between the liquid water and water vapor in the porous medium because Δp is compared instead of absolute pressure values from this section.

4.7.1.2 Comparison of Permeability Coefficients

Permeability, often used in Earth sciences as a characteristic of soil and in textile science as a characteristic of fabric breathability, refers to the ability of a liquid or gas to flow through a porous medium. The permeability coefficient, $\mathscr{K}$, is expressed in units of area (m^2) which is akin to the void space in a porous material's cross section taken perpendicular to the direction of flow [95]. Another common unit for permeability is the darcy (d) or millidarcy (md) and 1 darcy is $9.869 * 10^{-13} m^2$. A larger permeability coefficient is indicative of a small pressure drop because there is less resistance to molecules moving through the permeable medium. A less permeable porous media indicates a higher vapor pressure because vapor molecules build-up at the liquid/vapor evaporation interface, which in turn decreases the evaporation rate according to the Hertz-Knudsen Equation (Eq. 4.14). The pressure of the liquid water region (continuum regime) is determined by the porous medium's permeability to liquid water using Darcy's law [95]:

$$Q" = -\frac{\mathscr{K}_l}{\mu}\frac{\Delta p}{L} \tag{4.25}$$

where $\mathscr{K}_l$ is the liquid permeability coefficient, also called the intrinsic permeability because it is only a function of the porous structure itself and not of the characteristics of the flow. $Q"$ is volumetric flux rate ($m^3/s/m^2$ or m/s), μ is dynamic viscosity ($Pa \cdot s$), L is flow distance, i.e. porous media thickness (m), and ΔP is the pressure drop over the flow distance (Pa). The negative sign indicates flow from a high to low pressure.

While the general concept of permeability described by Darcy's law may be intuitive, the comparison between liquid and gas permeability is not. Some have found that porous media is more permeable to liquid than to gas in the continuum regime [72], while others have asserted that there is no significant difference in permeability when compressibility effects are taken into account [96]. However, the water vapor in a CubeSat sublimator is not in

the continuum flow regime. As shown in Figure 4.13, the Knudsen number of the flow at a variety of temperature/pressures and pore sizes places the flow in the transition and rarefied regimes. It is well understood that in non-continuum gas, **porous media permeability is greater for a gas than for a liquid** (discussed in the following pages), which yields a larger pressure drop in the liquid phase compared to the gas phase. This implies that the phase change interface will be closer to the inner edge (upstream side) of the porous medium, such as in Figure 4.18.

The permeability of a porous media to flow of a gas is dependent on the flow itself, not just the physical structure; this is especially true for non-continuum gases [97, 98]. $\mathscr{K}_g$ becomes a function of the mean free path of the gas (which determines its flow regime), and the mean free path of the gas depends on temperature, pressure, and the molecular diameter of the gas. As such, Darcy's law does not hold for non-continuum flow. Knudsen found what is widely known and accepted as the Knudsen paradox or Knudsen minimum: traditionally, as in continuum flow modeled by the Navier-Stokes equation and Darcy's Law, mass flux decreases with a decrease in pressure (and increase in Knudsen number). However, there is an observed minimum mass flux at $Kn = 0.8$, after which the mass flux *increases* with a further *decrease* in pressure (increased rarification) [99, 100]. This phenomena is due to the presence of the slip condition at the walls of the structure through which the non-continuum gas flows. The slip condition, in which the gas flowing along a solid wall has a non-zero velocity with respect to the wall, is not captured in Poiseuille flow theory. The wall slip increases the gas flow through the medium, thus increasing the overall permeability coefficient [97].

Klinkenberg found that the permeability coefficient for a non-continuum gas does not depend on the pressure drop (Δp), rather it depends on the average absolute pressure of the vapor in the porous medium, $\bar{p}_g$. The relationship between a gas' degree of rarefication, its mass flux, and a porous media's permeability to that gas is not intuitive so qualitative conclusions cannot be drawn. The permeability coefficients for porous media with non-continuum flow must be inspected quantitatively. If the flow is in the slip-regime ($0.001 < Kn < 0.1$), the Klinkenberg correction factor can be used to capture the effects of slip on the increased permeability coefficient [97, 98, 100]. Because the sublimator water vapor is

in the transition and rarefied regime, the Knudsen correction factor, fc, is used instead to find the permeability coefficient [101]:

$$\mathscr{K}_g = fc\mathscr{K}_l \tag{4.26}$$

where $\mathscr{K}_l$ is the intrinsic permeability coefficient for a liquid. The Knudsen Correction factor (fc) has been explored both theoretically and experimentally and is reviewed at length in other sources [101, 102]. The theoretical definition is [103]:

$$fc = 1 + \frac{A}{\bar{p_g} + B/\bar{p}_g^2}$$

where $\bar{p}_g$ is the average pressure of the vapor in the porous medium (Pa) and

$$A = C_1 \left(8\mu/d\right)\sqrt{\frac{\pi R}{T}} \qquad B = C_2 \left(8\pi RT\right)\left(\mu d\right)^2$$

where μ is the dynamic viscosity of the vapor ($Pa \cdot s$), d is the diameter of a pore (m), R is the gas constant for water (J/kgK), and T is the vapor temperature in Kelvin. C_1 and C_2 are identified in Tang, *et al.* [103].

Table 4.3: Pressure drop and permeability values for porous media samples of varying pore size and porosity at $T = 0°C$.

Max Pore Size [μm]	$\mathscr{K}_l$ [m^2]	$\mathscr{K}_g$ [m^2]	$\mathscr{K}_g/\mathscr{K}_l$
0.2	9.62e-14	1.39e-11	144.95
0.5	3.13e-13	2.49e-11	79.81
2	1.67e-12	4.19e-11	25.15
5	2.00e-12	2.22e-11	11.12
10	5.56e-12	3.41e-11	6.14
20	5.43e-12	1.95e-11	3.59
40	7.81e-12	1.80e-11	2.30
100	4.17e-11	6.34e-11	1.52

Table 4.3 shows the gas permeability values calculated at $T = 0°C$ for each of the porous samples from Mott Corporation alongside their published liquid permeability values [72]. $\mathscr{K}_l$ was obtained by the manufacturer at room temperature which is within the feedwater

temperature range in a sublimator. The mass flow rates used by Mott Corporation in computing $\mathscr{K}_l$ are greater than the mass flow rates found in a sublimator. Table 4.3 and Figure 4.17 can still be used to illustrate the relationship between liquid and vapor permeability and the evaporation location. The last column of Table 4.3 shows the ratios of gas to liquid permeability coefficients, which are proportional to the ratios of pressure drop in the gas and liquid regions. In Figure 4.17, the Knudsen correction factor for the gas permeability coefficient was computed for all eight pore sizes over a range of saturation conditions from $0°C < T < 10°C$ (Table 4.3 only shows a single saturation condition). The Knudsen correction factor is used in Equation 4.26 and the $\mathscr{K}_g/\mathscr{K}_l$ ratio is computed. As the Knudsen number increases and the vapor gets more rarefied (lower pressures and smaller pores), the highly dependent ratio of the vapor to liquid permeability coefficient increases.

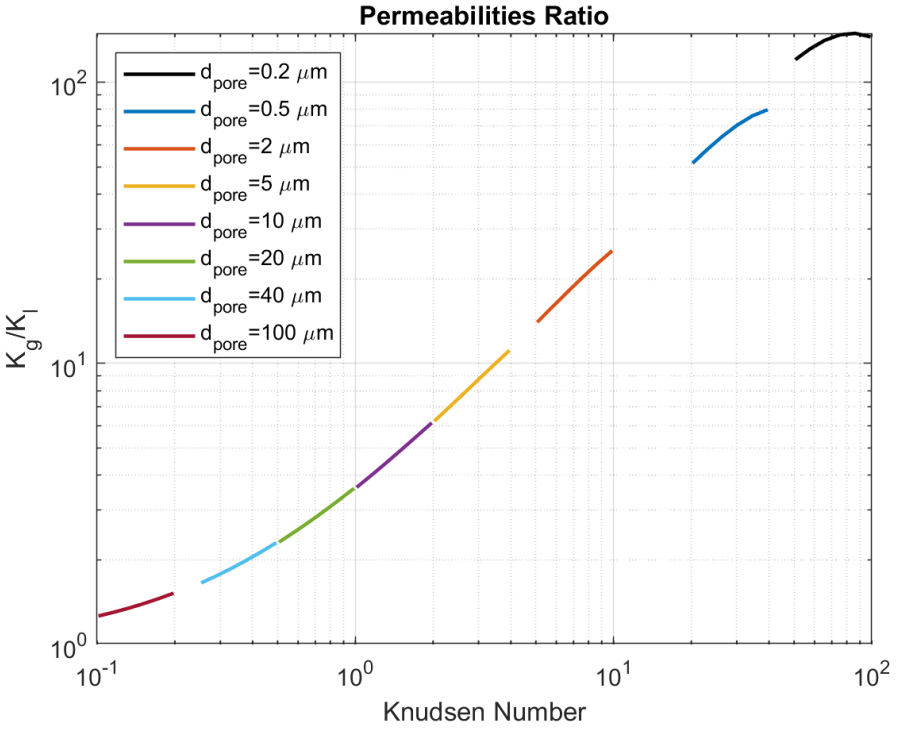

Figure 4.17: Ratio of permeability coefficients compared to Knudsen number Note the transition regime is $10^{-1} < Kn < 10$ and rarefied regime is $10 \leq Kn$.

Note that the values for the lowest Knudsen numbers in the dataset are in the slip flow regime which requires the Klinkenberg correction factor, not the Knudsen correction factor. The highest Knudsen number dataset is very rarefied and further work is required to

determine why the black curve decreases on the rightmost part of the plot. The ratio of the permeability coefficients is an indicator of the evaporation phase change location. If both the liquid and vapor permeability coefficients depended on $\Delta p/L$, then the exact evaporation location could be found with a slope comparison to find their intersection point. However, the exact interface location cannot be found in this scenario because $\mathscr{K}_l$ depends on $\Delta p/L$ and $\mathscr{K}_g$ depends on the average pressure. Every single Knudsen number configuration (pore size, temperature, and pressure) yields a ratio of gas to liquid permeability > 1 because the porous medium is more permeable to gas than to liquid. If $\mathscr{K}_g/\mathscr{K}_l$ is exactly equal to 1, then the evaporation interface would be at the halfway depth of the porous medium. Because $\mathscr{K}_g/\mathscr{K}_l > 1$ for our CubeSat sublimator design, the evaporation interface is upstream toward the inner edge of the porous medium, as represented in Figure 4.18.

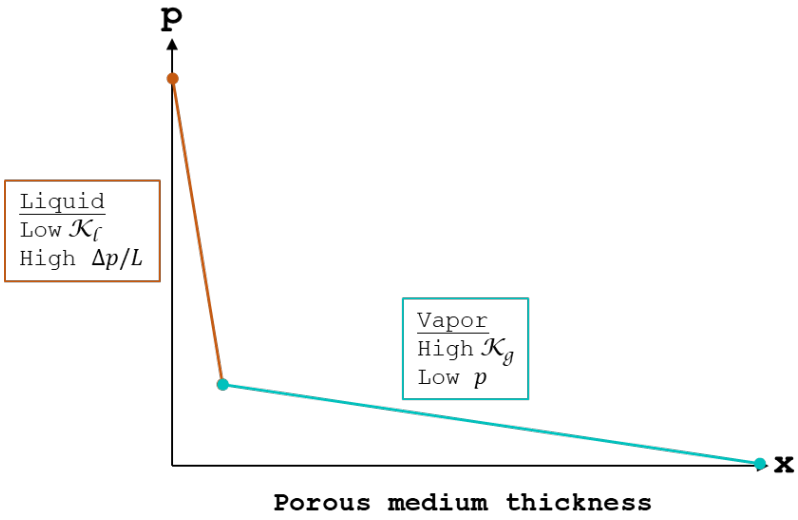

Figure 4.18: Representation of evaporaiton location based on relative permeability coefficients for liquid water and water vapor.

When the Weber equation is related to the ratio of permeability coefficients, some discrepancies are noted. For example, at a pore size of $d_{pore} = 5\ \mu m$ and vapor temperature of $1°C$, $Kn \approx 4$ so the flow is in the transition regime which corresponds to the right end of the yellow line in Figure 4.17. In this case, $\mathscr{K}_g/\mathscr{K}_l$ is approximately 12. This means that the porous medium is about twelve times more permeable to water vapor than to liquid water. This is reflected in the vapor region thickness calculation using the Weber equation in Figure 4.16. The vapor region occupies almost all of the porous medium (depending on the applied

heat flux). Discrepancies are found because the ratio of permeability coefficients is never less than one, which implies that the evaporation phase change interface can never be in the upstream half of the porous medium. This is not supported by the Weber equation calculations, where the vapor region thickness spans almost the entire porous media from 0.25mm up to 1.5mm, depending on the evaporation temperature/pressure and pore size. While both the permeability comparison and Weber equation provide different ways of understanding how the evaporation location can be obtained, the knowledge gaps are especially evident because the transition regime is the most difficult to model. Moving forward, the Weber Equation discussed in Section 4.6.2.3 is used to find the vapor region thickness in the evaporation and sublimation modes. In the evaporation mode, the temperature and pressures will be higher and Figures 4.8, 4.13, and 4.16, include a range of temperatures/pressures which cover both the sublimation ($T < 0°C$) and evaporation ($T > 0°C$) conditions.

4.8 Combining Models

The conduction equations and the Weber equation are combined to develop a new model, resulting in a plot showing the temperature at key interfaces, the location of the freezing interface if applicable, and the location of the sublimation or evaporation interface. As previously mentioned, both the conduction analysis (the "inside-out" perspective) and the rarefied flow through porous media (the "outside-in" perspective) are used to obtain the depth to which the feedwater penetrates the porous medium, the location of the ice formation, the ice thickness, and the phase change interface location.

Figure 4.19 is a zoomed-in look at Figure 4.20 to show the significance of each point on the plot. In the section labeled "Porous Media", the leftmost dot (at the feedwater gap-porous media interface) represents the location where the feedwater enters the porous medium. The second dot represents the location where the temperature reaches $0°C$ and ice forms, and the third dot represents the location where the ice sublimates. The empty space to the right of each curve indicates the vapor space. The slope of the temperature curve in the feedwater/porous media and ice/porous media are different because those two sections have different effective thermal conductivity values.

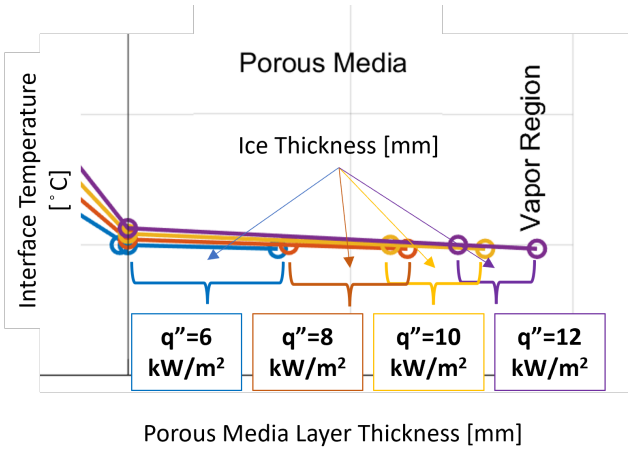

Figure 4.19: Zoom-in of temperature profile in Figures 4.20 - 4.23 to point out the meaning of each point.

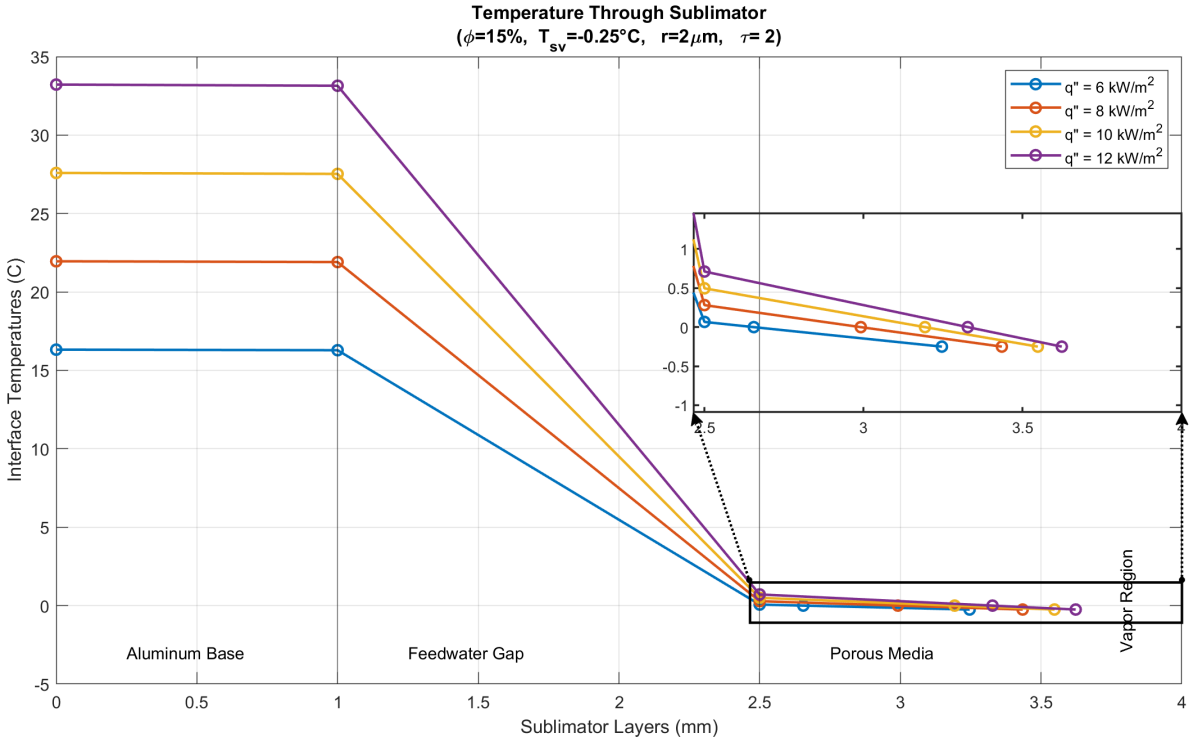

Figure 4.20: Temperature profile within sublimator which incorporates both the solution to the conduction equations and the Weber equation.

However, because $\phi = 15\%$ and most of the porous medium is the same metal structure, it is hard to visually discern the two different slopes. Figure 4.20 shows a scenario in which the porosity is $\phi = 15\%$, the average pore radius is $r = 2\ \mu m$, and the phase change interface is $T_{sv} = -0.25°C$. The temperature of the heat source can be maintained between $15°C$

and $35°C$ while rejecting anywhere between 6 and 12 kW/m^2 of waste heat. The sublimator sizing in Chapter 3 with 50 W waste heat and a surface area of 50 cm^2 yieldsd a heat flux of 10 kW/m^2, which is within the range used here. **The larger the heat flux, the smaller the ice thickness and the farther downstream the ice is formed.**

Figure 4.21 shows a relative visualization of each sublimator layer for the case of maximum heat flux ($q" = 12\ kW/m^2$) from the temperature distribution plot in Figure 4.20. This visualization emphasizes the thin ice and vapor layers which exist so that the heat source can maintain an operating temperature using a sublimator.

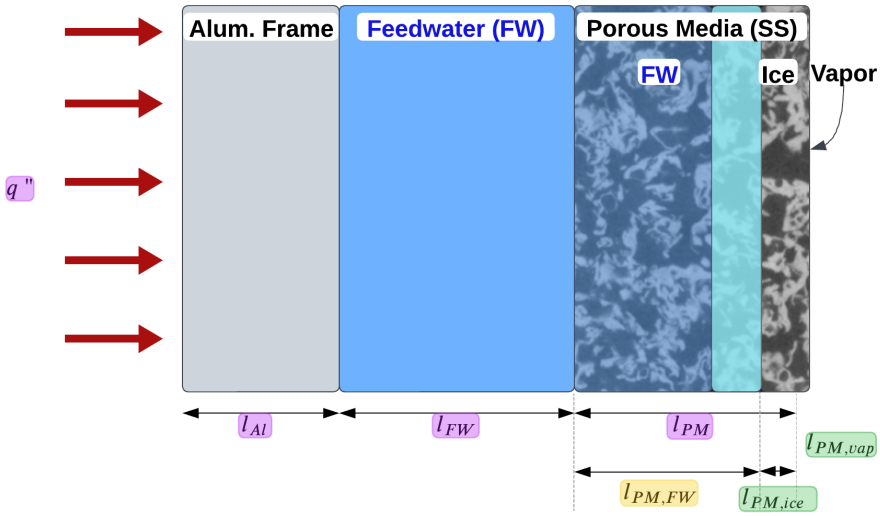

Figure 4.21: Visualization of sublimator with $q" = 12\ kW/m^2$, $\phi = 15\%$, $T_{sv} = -0.15°C$, $r = 1.56\ \mu m$

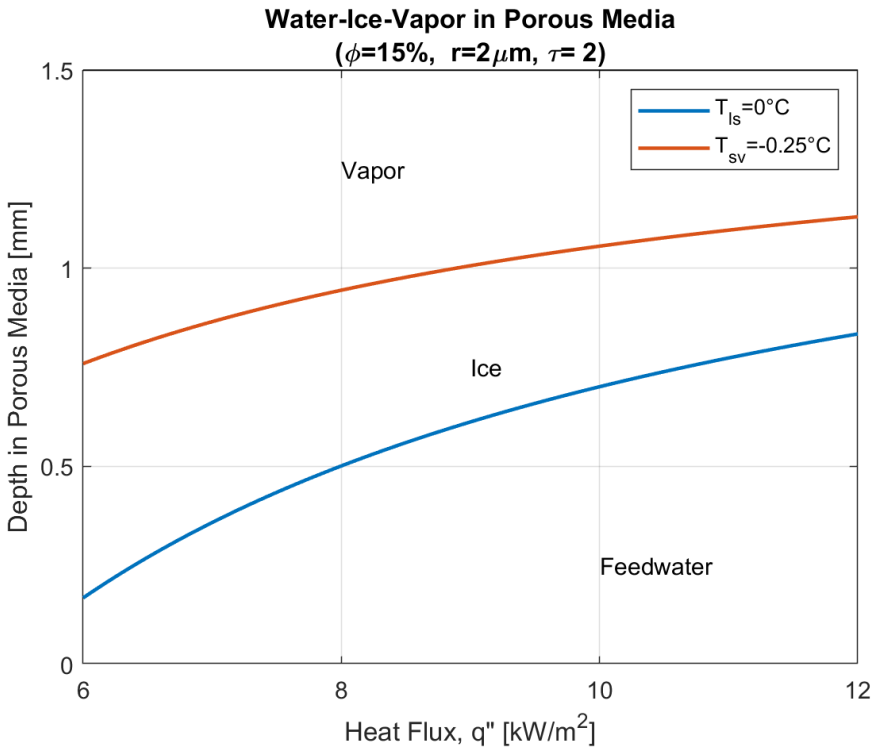

Figure 4.22: Heat flux versus phase change location. Sublimater "layers" are rotated 90°.

Figure 4.22 shows another way to visualize the distribution of feedwater, ice, and vapor within the porous medium as a function of the applied heat flux. While Figure 4.20 shows a snapshot of the various phases within the porous medium for four distinct heat fluxes, Figure 4.22 shows a similar relationship with the sublimator layers oriented bottom-to-top instead of left-to-right. Over a continuous heat flux range on the x-axis, the ice and vapor layers decrease with an increase in heat flux as discussed in Sections 4.5 and 4.6.2.3. Once again, an increase in heat flux pushes out the freezing interface and causes a thinner ice layer.

Figure 4.23 shows an evaporation-only scenario in which the porosity is $\phi = 15\%$, the average pore radius is $r \approx 2\ \mu m$, and the phase change interface is $T_{sv} = 1.5°C$. The temperature of the heat source can be maintained between $15°C$ and $35°C$ while producing anywhere between 6 and 12 kW/m^2 of waste heat. If the pore size, porosity, or heat rejection requirement were to be changed to a design that is *not* physically feasible, the plots would reflect that, as seen in the Realizability discussion in Section 6.5. Changing the porous medium design space, namely the porosity and pore size, affects the feasibility of waste heat rejection while maintaining a temperature within operating limits. The same is true for the

sublimation scenarios as well.

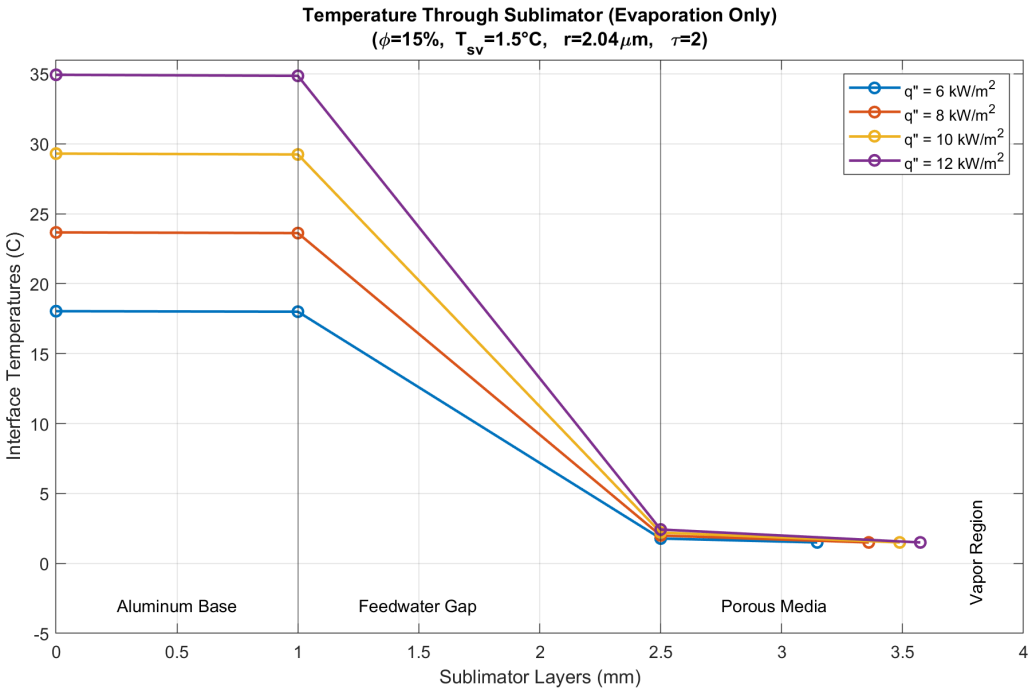

Figure 4.23: Temperature profile within sublimator which incorporates both the solution to the conduction equations and the Weber equation for the evaporation case [104].

Since we have focused on post-startup, steady-state operation, the evaporation mode was not the focus of this research, and more exploration is required to determine the conditions under which evaporation may occur. More specifically, it is expected that small differences in sublimator manufacturing and the porous medium microstructure could lead to spatial differences in temperature throughout the volume of the sublimator. This would likely lead to certain areas of the porous medium in which ice forms and sublimation occurs, and other areas in which only evaporation occurs. Temporal differences may be found as the heat flux fluctuates throughout a mission, leading to a combination of sublimation and evaporation depending on the waste heat output from the heat source. In addition, there may be a cyclical nature of alternating evaporation/sublimation, even after the transient start-up period and even with a constant heat flux applied to the sublimator. This alternating evaporation/sublimation cycle was introduced in Section 1.3 but merits additional exploration and modeling. As previously mentioned, there has been no experimental observation of the presence of ice, nor its location or thickness. As shown in the temperature distribution plots,

there are a number of possibilities for the location and thickness of ice formation, each each with their own thermodynamic implications:

- If ice forms on the upstream side of the porous medium, then the geometry of the porous medium significantly affects the vapor pressure drop through its depth. The vapor pressure drop contributes to the determination of pressure at the ice sublimation interface. This pressure is considered in determining the relationship between the sublimation rate, heat rejection rate, and design feasibility.
- If ice forms on the downstream side of the porous medium, then the porous component contributes to the heat rejection process by limiting water flow rate via surface tension during transient start-up. Here, porous media geometry is only a factor in liquid permeability calculations because there is minimal vapor flow through the pores.
- If ice forms somewhere within the porous medium, then the microstructure geometry affects the water vapor flow and pressure and, by extension, the sublimation rate and heat rejection rate. In addition, the temperature of the metal surrounding the pores influences the water/ice temperature, and thus the sublimation rate and heat rejection rate.

Regardless of the sublimator porous media design choices (i.e. material, pore size, porosity, tortuosity, and thickness), the sublimator may experience a full range of heat fluxes which would shift the ice location throughout the depth of the porous medium. As a result, the three bullets listed above are all applicable: the geometry of the porous medium affects both the liquid water and water vapor flow.

4.9 Summary

Inputs to the sublimator model proposed above include, but are not limited to, the surface area and thickness of the porous medium, the range in heat flux from waste heat, and the operating temperature limits for the payload. The sublimator outputs include the temperature distribution through the porous medium, the location of the ice formation and the sublimation interface, the saturation temperature/pressure, and the pressure gradient in the vapor

phase. This chapter demonstrates that the sublimator porous media temperature is very near the triple point of water, and the sublimation interface is at or below the triple point of water. The heat flux from the source and conduction through the sublimator structure determine the location of ice formation. Conduction through the sublimator, combined with the pressure drop in the vapor space, determine the location of the sublimation interface. This chapter also describes porous media, rarefied flow, and how the Weber equation is used to obtain the pressure drop in the vapor space, as well as some of the shortcomings of the Weber equation with respect to the Knudsen paradox. The evaporation case was explored both qualitatively and quantitatively, with a focus on the permeability relationships as insight into the connection between liquid and vapor pressures and evaporation location. Lastly, the conduction and flow models were combined to obtain a holistic look at the sublimator in terms of both temperature and pressure, which offers insight and a visual representation of the phase change processes within the porous medium. The next chapter discusses the sample porous components which were imaged as well as a rarefied flow experiment conducted using porous filters.

Chapter 5

Hardware Characterization & Experiment

The previous chapters discussed how the evaporation/sublimation process may occur within porous media. This chapter discusses the physical hardware used to explore the phenomena from Chapter 4. There are two main objectives for which porous medium samples are used. Table 5.1 below outlines the two objectives.

Table 5.1: Hardware Characterization & Experiment Goals

	Objective	Porous Medium	Approach	Desired Results
1	Compare theoretical descriptions of porous media to 3D sample scans and physical parameters.	Sample porous discs from Mott Corp. [72]	X-Ray Computed Tomography Scans & Post-Processing of 3D Images	porosity (ϕ) pore size (r) thermal conductivity (k) tortuosity (τ) permeability ($\mathscr{K}$)
2	Validate the Weber model with experimental data.	Filter from Swagelok (with a porous plug from Mott Corp [75])	Conduct rarefied water vapor flow experiment at NASA Goddard Space Flight Center	Relationship between mass flow rate ($\dot{m}$) & pressure drop (dp/dx)

The Swagelok filter's porous plug (Objective 2) could not be imaged in an X-Ray machine because it is encased in stainless steel. Both porous media used are sintered 316L Stainless Steel from Mott Corporation with pore size and porosity reported from the manufacturer, outlined in Table 5.2. 3D image scans were taken of sample discs with smaller pore size (0.2 μm up to 5 μm), but the X-Ray resolution was not fine enough to yield good quality images so they are not included.

Table 5.2: Description of Porous Medium Hardware from manufacturers [72, 75].

Porous Medium Type	Avg. Pore Diam. [μm]	Overall Thickness [mm]	Overall Diam. [mm]	Porosity
Sample Disc	10	1.57	25.4	44%
Sample Disc	20	1.57	25.4	47%
Sample Disc	40	1.98	25.4	50%
Sample Disc	100	2.36	25.4	54%
Swagelok Filter	0.5-2	6.35	6.35	27-36%

5.1 3D Imaging

The sample porous discs were taken to Dr. Douglas Rowland at the UC Davis Center for Molecular and Genomic Imaging (CMGI), who in turn partnered with Sigray [105] to obtain high-powered 3D images using X-Ray Computed Tomography (CT) scans. The scans are described as follows:

Table 5.3: X-Ray CT scanner configuration [105].

Parameter	Large Field of View	High Resolution
Voxel size	9.7 um	4.7 um
Voltage	150 kVp	150 kVp
Power	18.4 W	17.5 W
Number of views	3601	4801
Exposure time per view	2.0 sec	1.8 sec
Total exposure time	2 hrs	2.5 hrs
Field of view	28.5 mm x 22.3 mm	13.8 mm x 10.8 mm

The 3D images in this section were rendered using Dragonfly software, Version 2022.2 for Linux [70]. Regions of Interest (ROI) were created by cropping a volume of the image of a full disc and the ROIs were split using the Otsu threshold approach to represent the metal substrate ("foreground") and void space ("background"). The Otsu threshold categorizes each voxel (volumetric pixel) intensity in a manner which minimizes the variation in intensity within the foreground and background categories [106]. Dragonfly was then used to obtain the porosity of the sample porous discs for each ROI to compare with the values reported by the manufacturer, shown in Section 5.1.1, Table 5.4.

As previously discussed, it is common to model a porous medium as a bundle of capillary tubes, as was done in this research. The Dragonfly software screenshot in Figure 5.1

qualitatively illustrates the limitations of this approach: visually, it is difficult to identify a distinct pore volume and flow path. In the cross-sectional visualizations, the magenta areas are the solid stainless steel microstructure and the green areas are the void spaces. Note that this sample has much larger pores and a much greater porosity than the porous medium typically used in sublimators.

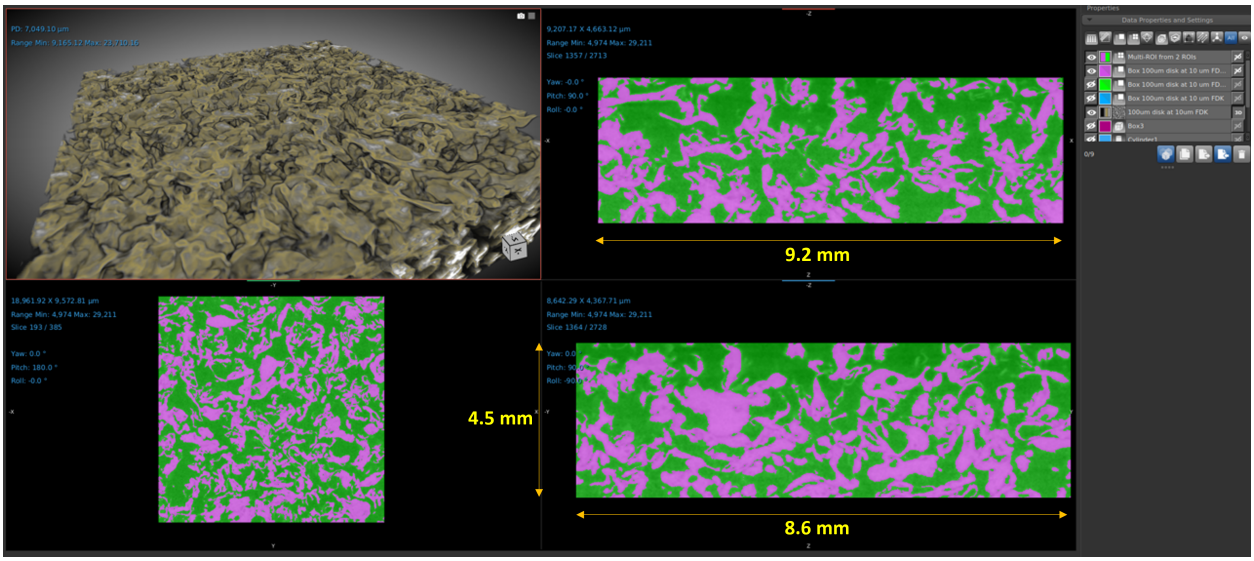

Figure 5.1: Screenshot of Dragonfly: X-Ray of 100 μm pore size, 10 μm voxel, FDK. The magenta areas are the solid stainless steel microstructure and the green areas are the void space.

5.1.1 PuMA

The 3D images from Dragonfly were imported into the Porous Microstructure Analysis (PuMA) software [71, 107]. PuMA was used to compute effective material properties of the sample discs, which can help to quantitatively illustrate the limits of the Weber model. PuMA computations were used to obtain tortuosity (τ), used in Equation 4.20 in Section 4.6.2.3. Appendix A provides more details of the settings used in PuMA to obtain these values. PuMA can also be used to compute the and thermal conductivity (k), the characteristic length (r), which in this case is comparable to the median pore diameter, and permeability ($\mathscr{K}$) but the computation for that is out of the scope of this research.

The different types of tortuosity were introduced in Section 4.6.2.1. The diffusion tortuosity computed in PuMA utilizes a particle-based solver which is appropriate for *any* flow

regime [78]. Based on a conversation with Dr. Joseph Ferguson, one of the creators of PuMA, it was deemed appropriate to use the particle-based computation method to solve for the tortuosity in the *continuum* flow regime. The diffusion tortuosity in the continuum regime could then be used in the Weber Equation (Eqs. 4.20-4.23) as a scaling factor to the capillary tube length as if it were the geometric tortuosity [108]. In the future, the thermal conductivity values could be used in the conduction equations in Chapter 4 after comparing these results to the thermal conductivity calculations from Equation 4.7 [66, 67].

When a 3D Tiff file is imported into PuMA, a range of intensity (1-255) must be input to differentiate between voice space (darker colors) and solid structure (lighter colors). The void space intensity range was chosen to yield a porosity that matched the porosity obtained in Dragonfly. Figure 4.10 shows a 3D rendering of two of the sample discs.

Table 5.4: Comparison of Manufacturer & Computed Specifications for Sample Discs.

Avg. Pore Diam., r $[\mu m]$	**Porosity** ϕ		**Tortuosity** τ	
Mott	Mott	Dragonfly	Continuum (Geometric)	Transition (Diffusive)
10	44%	39%	1.877	3.587
20	47%	39%	2.055	3.952
40	50%	40%	1.619	2.878
100	54%	54%	1.583	2.118

Table 5.4 shows some parameters used to describe porous media obtained from the manufacturer, from Dragonfly, and from PuMA. Note that the tortuosity was calculated using two mean free path values: one in the continuum flow regime with a very small mean free path, per Dr. Ferguson's suggestion, and one in the transition regime calculated at water's triple point temperature and pressure. There does not appear to be a relationship between the average pore diameter, porosity, and tortuosity. Further research is required to better understand the PuMA findings. The sample porous disks used in the Dragonfly and PuMA analysis are larger than the porous medium used in sublimators, and there is not a clear understanding as to how the information from *more* porous samples with *larger* pores translates to *less* porous components with *smaller* pores. Only a sampling was taken for Table 5.4 and Appendix A archives more data collected about the porous discs using PuMA. When the

porosity of a component is less than 50%, there are many twists, turns, and pockets in the structure with gaps that are much smaller than the reported average pore size. According to Dr. Ferguson, the characteristic length calculated from PuMA should be significantly smaller than the reported pore diameter. This expectation will be verified with research in the near future. The manufacturer's average pore size was used in calculations because more in-depth research is required to determine the accuracy of using the characteristic length from PuMA for other computations such as the Weber model. The use of Dragonfly and PuMA to help quantitatively characterize porous media was interesting and informative, but the author's current understanding limits the level to which these characterizations may be integrated with the Weber model for diffusion of rarefied vapor in porous media.

5.2 Water Vapor Flow Experiment

This section discusses the experimental validation of the Weber equation for modeling a concentration-driven vapor diffusion through porous media at any flow regime, including rarefied flow. This experiment was conducted at NASA Goddard Space Flight Center with the support of the Thermal Engineering Branch (Code 545), specifically the Thermal Technology Development and Demonstration (T2D2) Facility. The goal of this experiment is to validate the Weber equation by obtaining the relationship between mass flow rate ($\dot{m}$) and pressure drop (Δp) across a porous medium of rarefied water vapor.

5.2.1 Experimental Set-Up

In order to obtain the $\dot{m}/\Delta p$ relationship, deionized (DI) water vapor must flow through a porous filter in low-vacuum conditions. Figures 5.3 and 5.4 show the schematic and experimental set-up, the focal point of which is the Swagelok test filter with a porous plug described in Table 5.2. Figure 5.6 shows the filter assembly portion of the set-up. The water vapor is sourced from degassed liquid DI water inside a stainless steel reservoir, shown in Figure 5.5.

An experiment trial first begins when Valve 1 in Figure 5.3 is opened and the liquid water in the reservoir is exposed to vacuum via flow through the porous element/filter. The liquid

water begins to evaporate and its water vapor flows through the test apparatus, through the test filter, into the vacuum chamber, and out of the low vacuum pump. The temperature of the water, and thus the saturation temperature of the water (both vapor and liquid) is determined by the chiller bath in which the reservoir is fully submerged. The saturation temperature of the liquid water/water vapor determines its saturation pressure. Eleven experimental trails were completed with saturation temperatures ranging from -4°C to +5°C and each lasting approximately 3.5 hours. During the trials when the water temperature was sub-zero $°C$, the water in the reservoir would freeze. The reservoir was not completely filled with water to allow for vapor space and expansion during freezing. In order to prevent liquid droplets from creeping along the tubing and entering the porous plug, a long vertical tube section was placed between the water reservoir and the test filter. In addition, a small glass tube section was added for visual confirmation that there were no liquid water droplets in the flow during the experiment.

Mass flow rate is obtained by measuring the weight of the liquid water (and the water reservoir) before and after each experimental trial. While this approach may seem rudimentary, it is the most reliable and cost-effective means to obtain the water utilization. Section 5.2.2 shows the validity of this measurement approach in terms of steady-state assumptions and the effects of uncertainty.

The **temperature** of the entire test apparatus was maintained at or near room temperature to ensure the water vapor would be *superheated*, where its actual temperature is greater than its saturation temperature ($-4°C$ to $+5°C$ compared to $20 - 25°C$). Relatively warm equipment prevents condensation on any surfaces in the set-up, especially in the porous filter where the presence of liquid water could block pores and affect the results. Figure 5.2 shows the temperature and pressure configuration used in the experiment relative to the phase diagram of water.

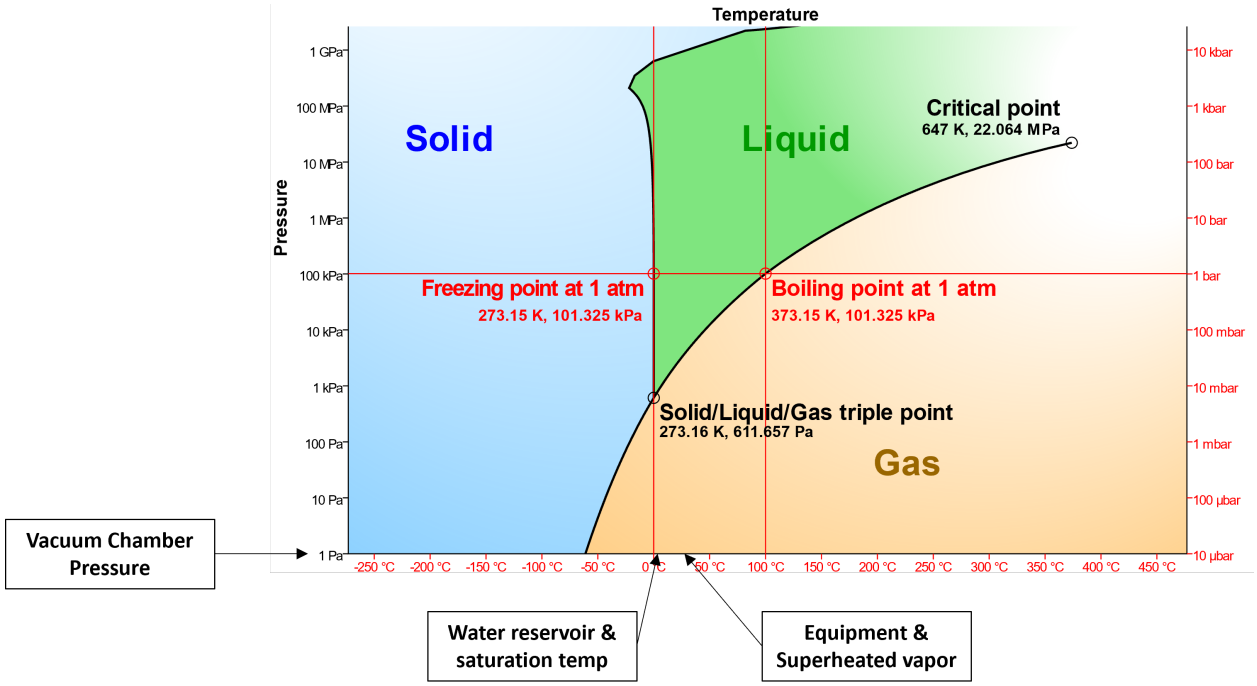

Figure 5.2: Phase diagram for water with experiment parameters.

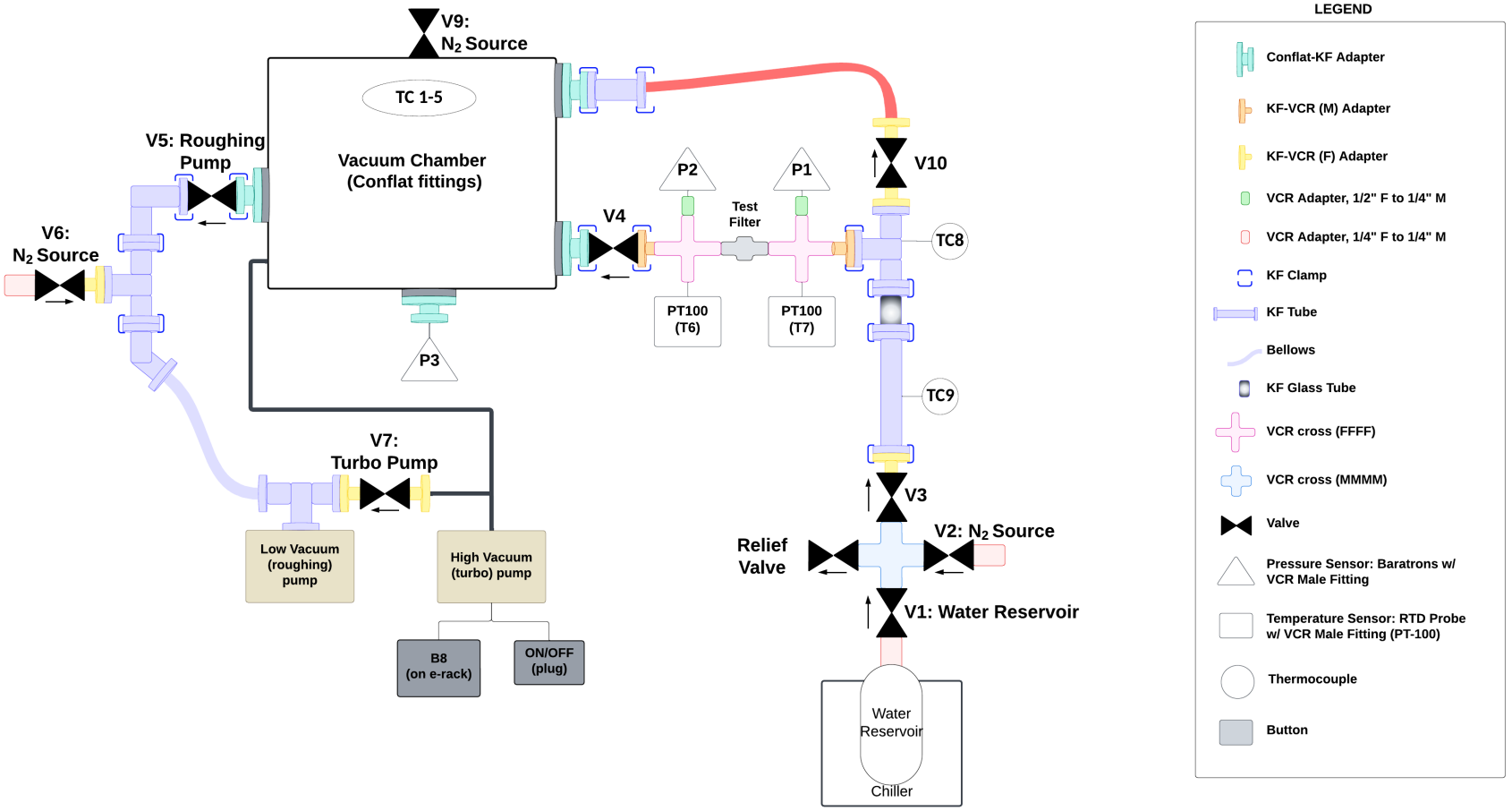

Figure 5.3: Experiment Schematic

In Figure 5.3, it should be noted that the section between Valve 10 and the vacuum chamber (the red-orange tube section) as well as the high vacuum turbo pump are only used for rapid pump down *in-between* experimental trials. In addition, nitrogen is flowed directly into the low vacuum roughing pump to prevent the condensation of water vapor in the pump *during* an experimental trial and the other N_2 sources are only utilized *in-between* trials.

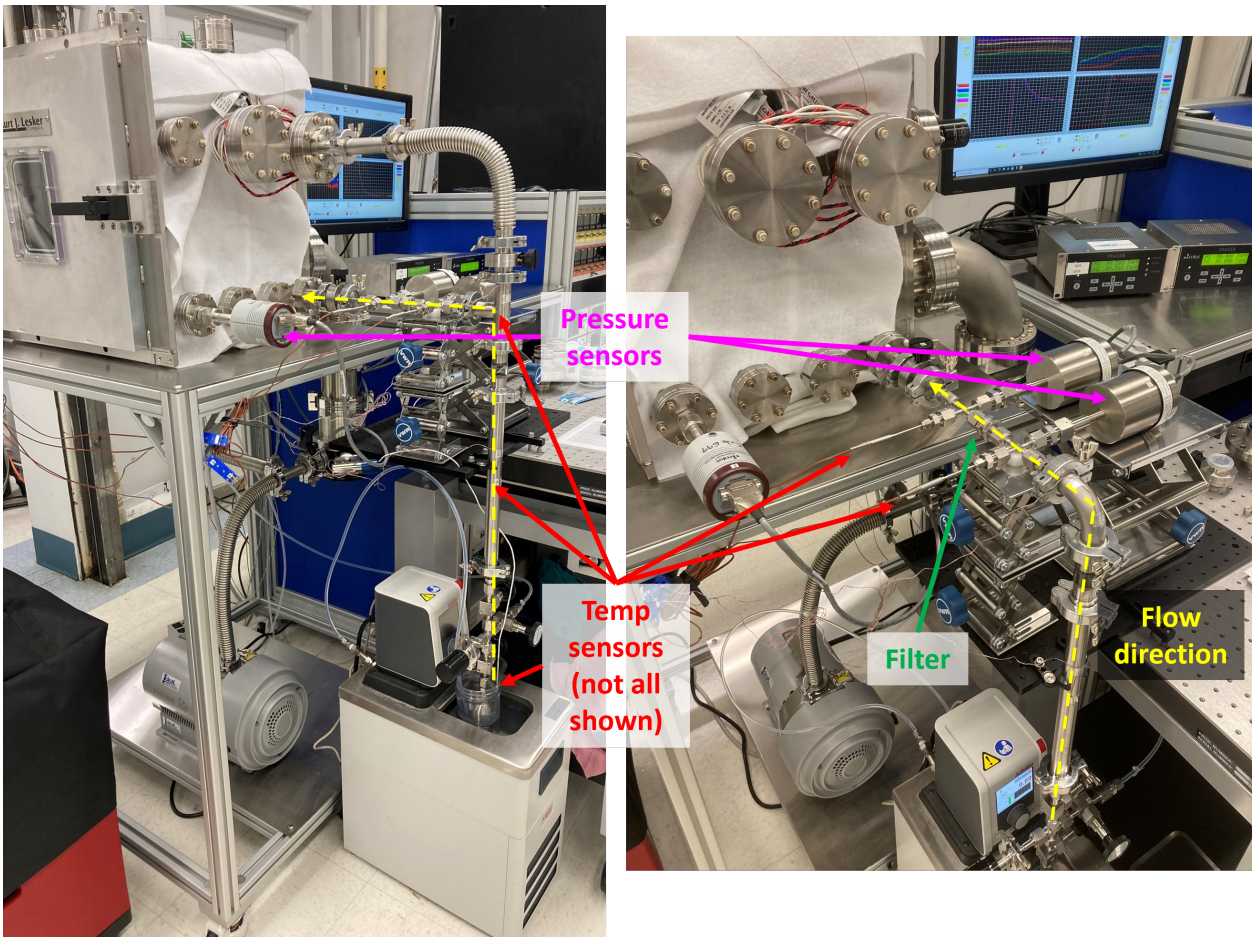

Figure 5.4: Full experimental set-up.

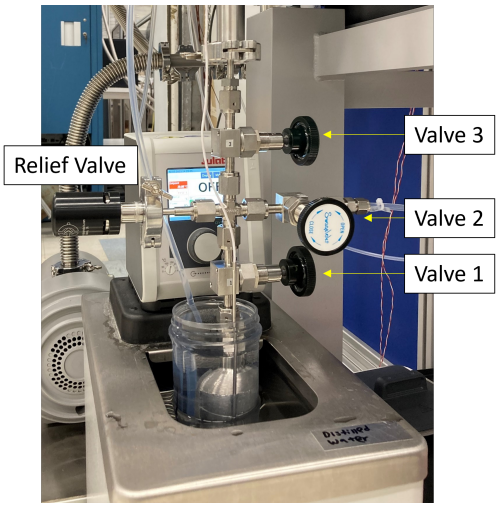

Figure 5.5: Water reservoir in chiller bath. PRT probe is taped to the outside of the stainless steel reservoir. Valves 1-3 and the relief valve are also visible and low vacuum pump is in the background.

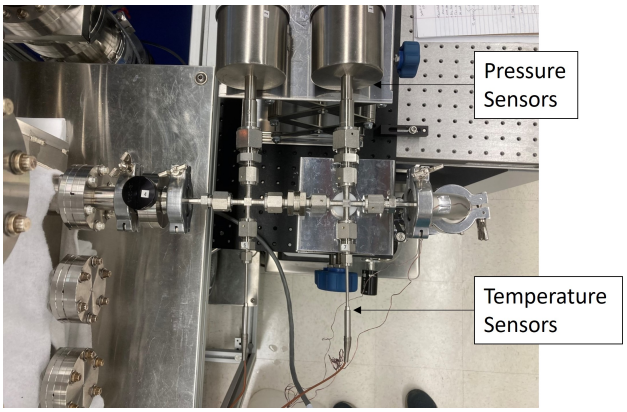

Figure 5.6: Test filter assembly, including pressure sensors (top) and temperature sensors (bottom). Water vapor flows from right to left in this image and entrance to vacuum chamber is seen on the left.

5.2.1.1 Sensors Suite

The two thermodynamic state variables measured were pressure and temperature. Table 5.5 lists the two pressure sensors, two temperature sensors, and associated data acquisition systems, including each item's accuracy and resolution data, if applicable. The pressure and temperature sensors in this table can also be found on the schematic (Figure 5.3) denoted by "P" (pressure), "PT100" and "TC" (temperature).

Table 5.5: Description of pressure, temperature, and mass sensors used in experiment.

Measurement	Description	Mfr.	Accuracy & Uncertainty
Pressure x2 (near filter)	Baratron, Capacitance Manometer, Absolute Pressure Transducer, 10 torr range, 0-10 VDC	MKS	Non-linearity, hysteresis, non-repeatability: $\pm 0.12\%$ of reading Confidence Level: 3σ Resolution: 1 mtorr
Pressure (in chamber)	Baratron, Capacitance Manometer, Absolute Pressure Transducer, 10 torr range, 0-10 VDC	MKS	Non-linearity, hysteresis, non-repeatability: $\pm 0.25\%$ of reading Confidence Level: 3σ Resolution: 1 mtorr
Pressure (filter, chamber)	Digital Multimeter (DMM) PXIe-4081, 7.5 digit, reads voltage	National Instruments	10.5 ppm of reading + 0.5 ppm of range
Pressure (filter, chamber)	Multiplexer PXIe-2527, reads voltage 0-10V scale	National Instruments	No uncertainty. (3 channels, sampling at 3.4 Hz and recording each channel at 1 Hz)
Temperature (reservoir)	Platinum Resistance Thermometer (PRT) probe, Resistance Thermometer Detector (RTD), PT-100	Omega Engineering	1/10 DIN = $\pm 1/10 * (0.3 + 0.005T)$ -3°C: $\pm 0.0285\Omega$ 1°C: $\pm 0.0305\Omega$ 5°C: $\pm 0.0325\Omega$
Temperature x2 (filter)	Thermocouple probe	Omega Engineering	Greater of 0.5°C or 0.4%
Temperature (reservoir)	DMM Keithley 6500, 6.5 digits, reads resistance	Tektronix	0.0075% of reading + 0.0020% of range Resolution: 100 $\mu\Omega$
Temperature (filter, external, chamber)	Multiplexer PXIe-4353, Temperature input module, reads voltage	National Instruments	$\pm 2\mu V$
Mass	VWR Balance 3002E	Avantor	Resolution: $0.001g$ Linearity: $\pm 0.03g$

5.2.2 Results: Flow Regime

The next section steps through the propagation of uncertainty for the pressure and temperature measurements taken during the experiment. There are a number of assumptions which were made so that the experimental data could be compared to the Weber model. The following pages review each assumption to show why the assumption is valid. First, it should be noted that the water vapor throughout the porous plug is well within the rarefied

regime, as depicted in Figure 5.7.

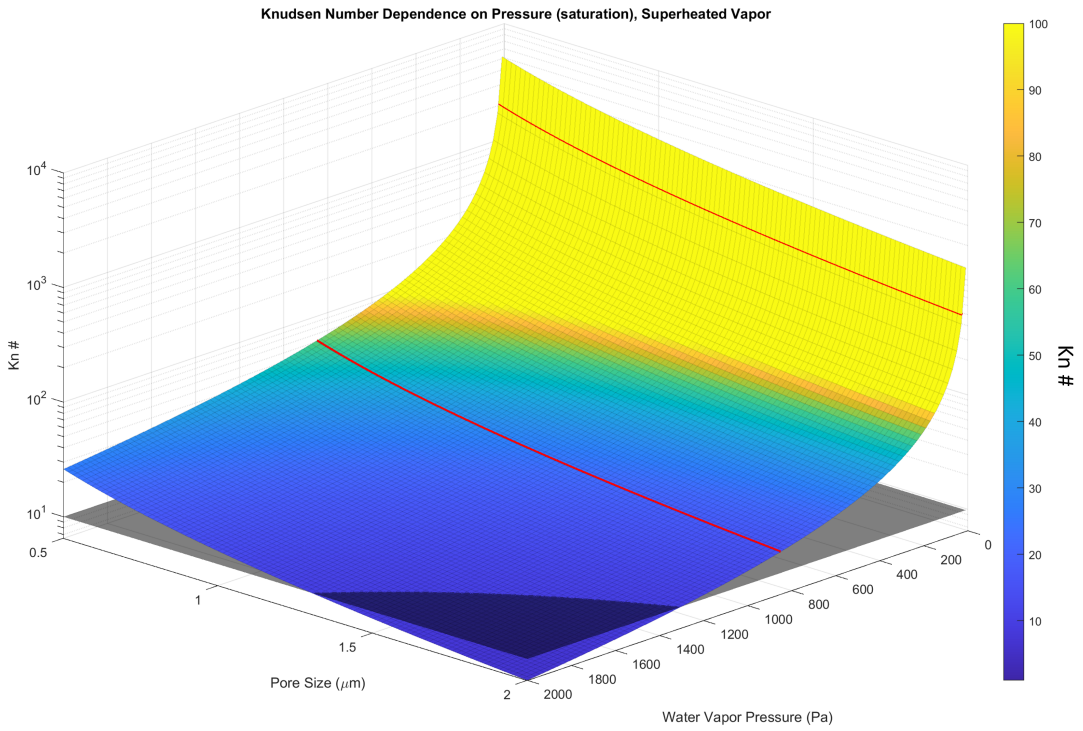

Figure 5.7: Knudsen number as determined by pore size and water vapor saturation pressure, where $T = 21°C$ (average superheated water vapor temperature). The horizontal plane divides the transition and rarefied regimes and the red lines show the vapor pressure range in the experiment.

5.2.3 Results: Uncertainty Analysis

The pressure and temperature measurement errors derived in this section are used for plotting purposes in the subsequent sections. A pictorial representation of the propagation of uncertainty in **pressure measurements** is shown in Figure 5.8.

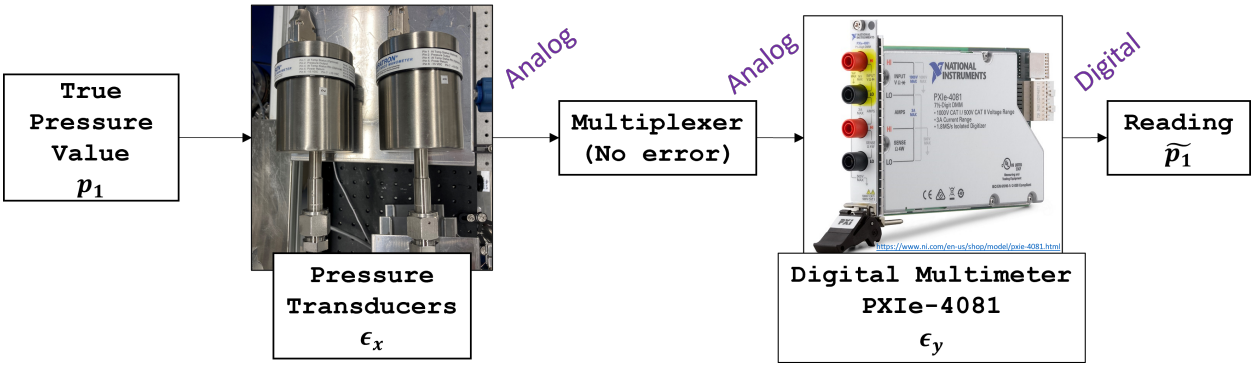

Figure 5.8: Propagation of uncertainty in pressure measurements.

The error in the pressure measurement is due to (1) the pressure transducer and (2) the digital multimeter. The pressure transducers upstream and downstream of the test filter are denoted P_1 and P_2, respectively, and have a linearity error $\epsilon_{p,x} = \pm 0.12\%$ of the voltage reading. The DMM has a linearity error of $\epsilon_{p,y_1} = 10.5ppm$ of the reading and a zero-error of $\epsilon_{p,y_2} = 0.5ppm$ of the range (10V); note that ADC sampling error is included in the reported errors. The total error is

$$\epsilon_P = \sqrt{(\epsilon_{Px} + \epsilon_{Py_1})^2 + (\epsilon_{Py_2})^2}$$

which is added to each pressure measurement as $\tilde{P} = P \pm \epsilon_P$. Note that ϵ_{Px} and ϵ_{Py_1} are both dependent on the reading so they are added together and ϵ_{Py_2} is independent of the reading so it is added in quadrature.

The error calculation for Δp is similar, where ϵ for each pressure measurement is independent so the errors are added in quadrature, where $\epsilon_{P_1} = \epsilon_{P_2}$:

$$\epsilon_{\Delta p} = \sqrt{(\epsilon_{P_1})^2 + (\epsilon_{P_2})^2}$$

A visual representation of the propagation of uncertainty in **temperature measurements** is shown in Figure 5.9.

Figure 5.9: Propagation of uncertainty in temperature measurements.

The error in the PRT measurement is due to (1) the PRT and (2) the DMM. The PRT probe has an accuracy of 1/10 DIN, which is $\epsilon_{Tx} = \pm 1/10 * (0.3 + 0.005T)$ where T is the target temperature being measured (T_{sat}). The DMM has a linearity error of $\epsilon_{Ty_1} = 0.0075\%$ of the resistance reading and a zero-error of $\epsilon_{Ty_2} = 0.0020\%$ of the range (100Ω). Similar to the pressure measurement error, the total error is

$$\epsilon_T = \sqrt{(\epsilon_{Tx} + \epsilon_{Ty_1})^2 + (\epsilon_{Ty_2})^2}$$

which is added to each PRT temperature measurement as $\tilde{\Omega} = \Omega \pm \epsilon_T$. The resistance reading is then converted to temperature according to published tables [109].

5.2.4 Results: Assumptions & Observations

There are four assumptions about the flow in this experiment: (1) ideal gas, (2) isothermal, (3) low mach number, and (4) steady-state. The first three assumptions are addressed below and the fifth assumption is addressed in Section 5.2.7. In addition, there are two observations of interest about this flow: (1) adiabatic and (2) isenthalpic. These assumptions must hold true so that the experimental data can be compared to the Weber equation. The two observations, while not independent requirements, are important to discuss nonetheless.

5.2.4.1 Assumption #1: Ideal Gas

The Weber model uses an ideal gas assumption. The pressure and temperature of the water vapor used in the experiment determine if the suprheated water vapor is close to an ideal

gas. There are two approaches, described below, to determining the validity of the ideal gas assumption.

The **compressibility factor**, Z, indicates how much a real gas has deviated from an ideal gas. It is defined as the ratio of molar volumes of a real gas compared to an ideal gas at the same temperature and pressure [23]. The closer to 1 the compressibility factor, the more like an ideal gas. Table 5.6 shows the compressibility factors computed for each experiment trial scenario of suprheated vapor and a saturation pressure (dictated by the liquid water reservoir temperature) [18]. In all cases, Z is very near 1 so the ideal gas assumption is valid.

The flow through a filter with a porous plug can be thought of as flow through an expansion nozzle. The **Joule-Thompson coefficient** is a measure of the change in temperature with respect to a change in pressure at constant enthalpy [23]:

$$\mu_J = \left(\frac{\partial T}{\partial p}\right)_h$$

Because μ_J is a function of three thermodynamic properties, it is also a state property. During the experiment, water vapor flows into the porous plug at T_1, p_1 and expands through the plug to a lower pressure, p_2. When the temperature at the outlet (T_2) is measured, the Joule-Thomson coefficient can be obtained. Gas expansion under these conditions is known as throttling. The state at the outlet, as determined by p_2 and T_2, has the same enthalpy as the inlet. On an isenthalpic curve (T-p diagram), the slope of each curve is the Joule-Thompson coefficient. There are three distinct conditions found on an isenthalpic curve on a T-p diagram and highlighted in Figure 5.10.

- Inversion State: $\mu_J = 0$, inlet conditions equal outlet conditions. This is the case for an ideal gas.
- Conditions to the right of the inversion state: $\mu_J < 0$, temperature increases with a decrease in outlet pressure.
- Conditions to the left of the inversion state: $\mu_J > 0$, temperature decreases with a decrease in outlet pressure.

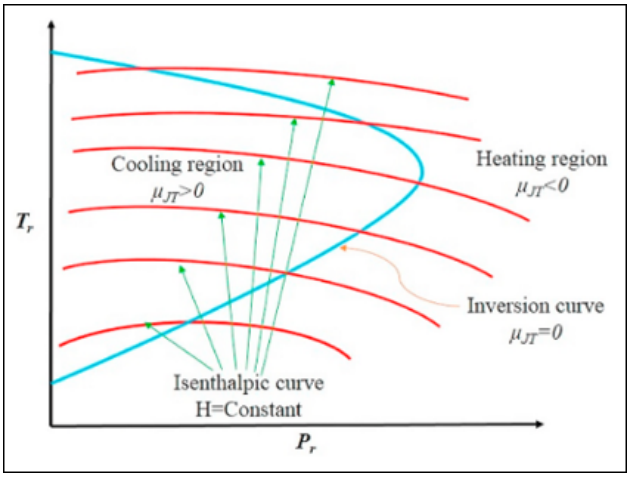

Figure 5.10: Isenthalpic curves on p-T diagram showing Joule-Thomson coefficient ranges [110].

Table 5.6 shows the Joule-Thomson coefficient computed for each experiment trial and in all cases, μ_J is very near zero so the ideal gas assumption is valid.

Table 5.6: Compressibility Factor and Joule-Thomson Coefficient for supreheated water vapor in experiment [18].

$T_{superheat}$ $[°C]$	T_{sat} $[°C]$	p_{sat} $[Pa]$	Z	μ_J $[°C/Pa]$
21	-4	437.45	0.99976	0.0002545
21	-3	476.04	0.99974	0.0002548
21	1	611.15	0.99967	0.0002563
21	0	657.09	0.99964	0.0002568
21	5	872.58	0.99952	0.0002600

The superheated vapor at the porous plug inlet can be characterized as an ideal gas. As the pressure decreases through the depth of the plug, the gas moves farther away from the vapor saturation line into the ideal gas region. Thus, the assumption is valid throughout the plug.

5.2.4.2 Assumption #2: Isothermal

The temperatures of the water vapor at the inlet and outlet of the porous plug are statistically the same, as seen in Figures 5.11 to 5.15. To further support this assumption, enthalpy is considered in Section 5.2.4.5. More specifically, in an ideal gas flow through an

expansion nozzle, enthalpy only depends on temperature. If the enthalpy is constant, then the temperature of a substance does not change and the flow is isothermal.

There is an apparent periodic nature of the temperature data which can be attributed to the lab environment. The heating, ventilation, and air conditioning (HVAC) system cycles about evey 20 minutes (1200 seconds). The experimental set-up is not isolated from the lab environment, so it is subject to HVAC cycles and resulting slight temperature fluctuations. It should also be noted that during the winter months (when this experiment was conducted), steam is flowed into the building to increase the humidity in the rooms. This helps the humans be more comfortable but is not ideal for equipment. The temperature range seen here is expected and reasonable. The more significant temperature information is related to the superheat: the measured temperatures during the experimental trials are at least $15°C$ greater than the saturation temperatures.

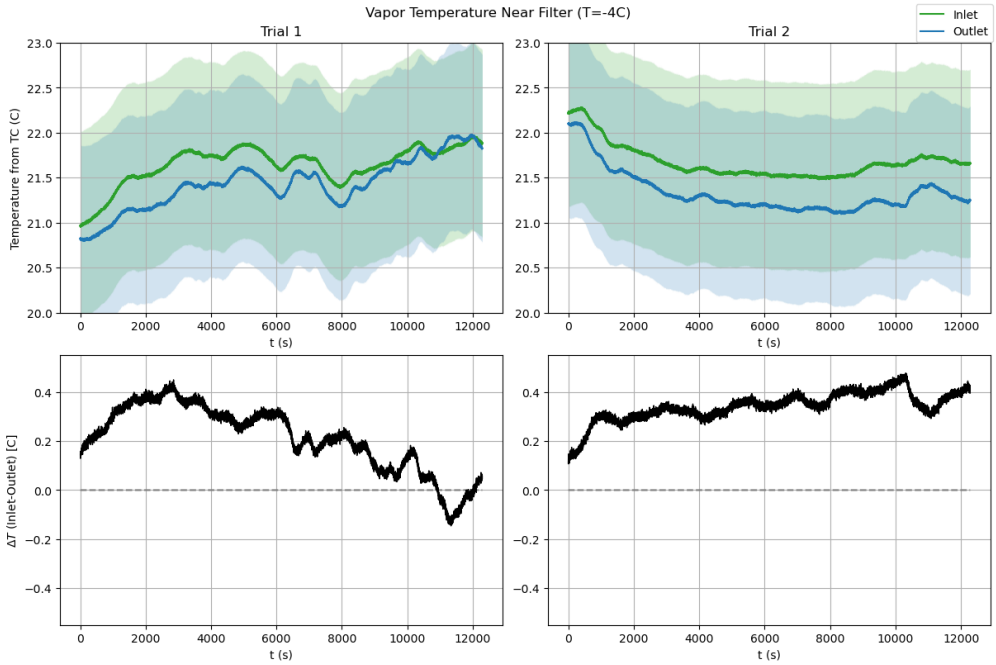

Figure 5.11: Temperature data across filter for $T = -4°C$.

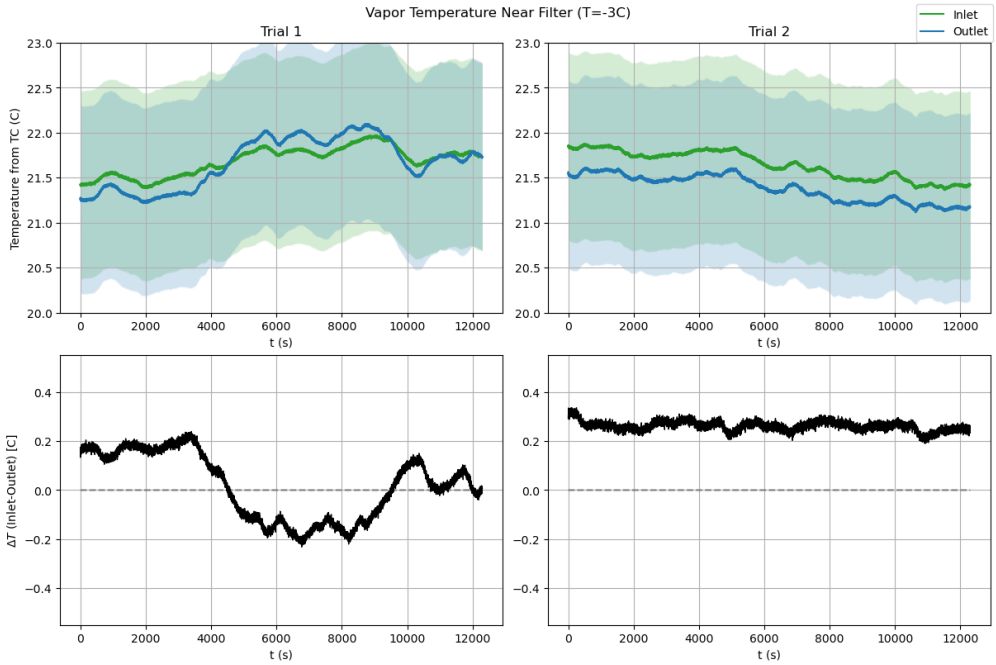

Figure 5.12: Temperature data across filter for $T = -3°C$.

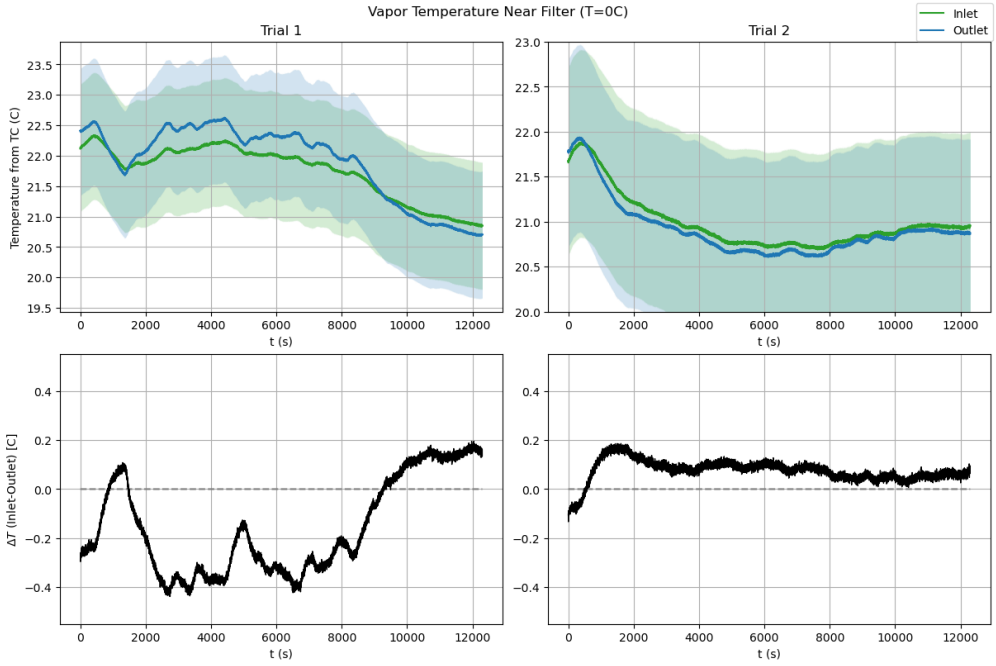

Figure 5.13: Temperature data across filter for $T = 0°C$.

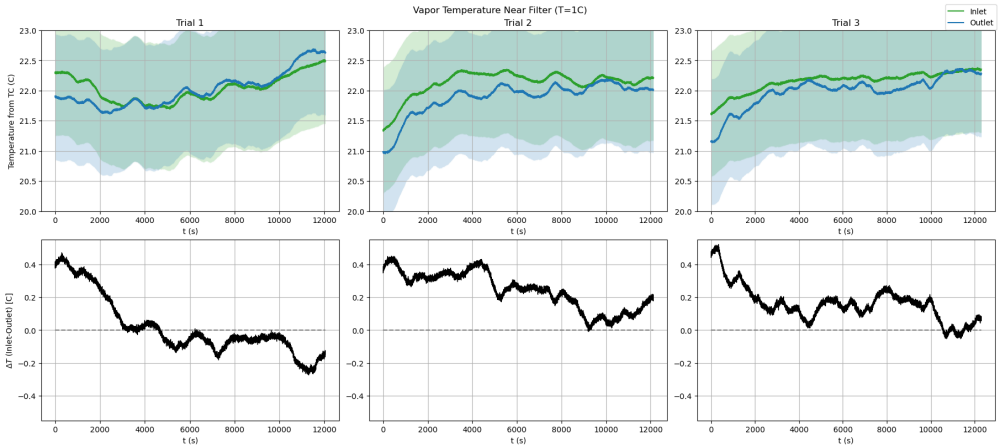

Figure 5.14: Temperature data across filter for $T = 1°C$.

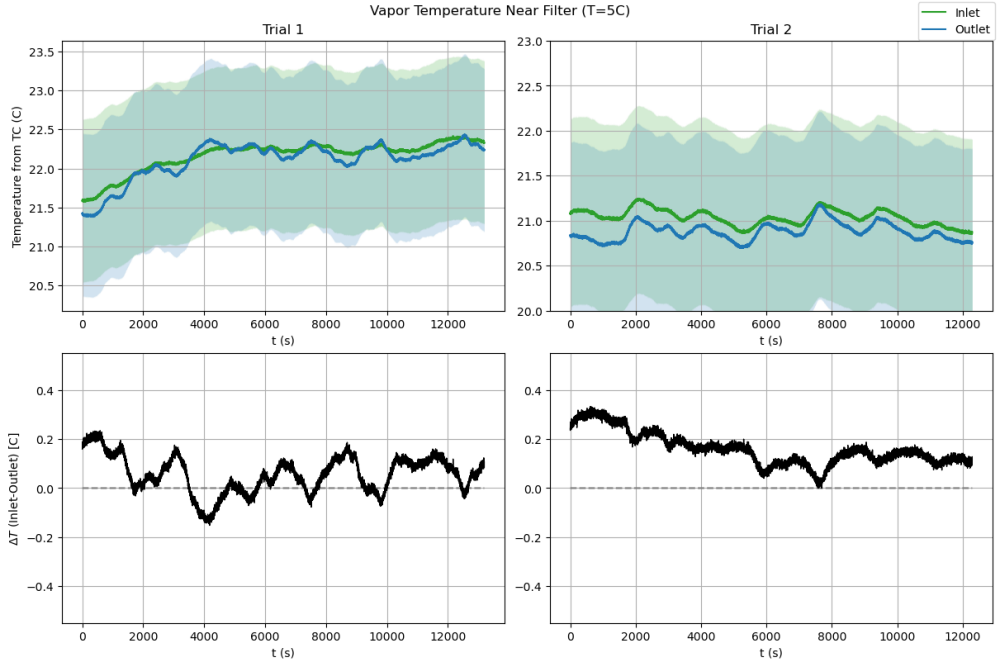

Figure 5.15: Temperature data across filter for $T = 5°C$.

Thus, comparison between the Weber equation and the experimental data is valid.

5.2.4.3 Assumption #3: Low Speed Flow

Mach number, $\mathcal{M}$, does not appear in Weber's equation, so it is important to demonstrate that the data collected is low speed flow before using it for model validation. It may seem obvious that the flow has a low-mach number because it is much less than the speed of sound, but it is prudent to calculate the mach number because the porous plug *does* act as

an expansion nozzle where the potential for high mach flow exists. The mach number is the ratio between a flow's velocity and the speed of sound at the flow conditions:

$$\mathcal{M} = \frac{V}{c} \tag{5.1}$$

where V is the flow velocity calculated from experimental data and c is the speed of sound from RefProp [18].

$$V = \frac{\dot{m}}{\rho A} \tag{5.2}$$

The mass flow rate is taken from the experimental data. The area is the cross-sectional area of the porous plug times the porosity ϕ: $A = 2.23 * 10^{-4}\ m^2$ [72]. The density is calculated from the ideal gas law under the experimental conditions for every temperature trial, from the inlet to the outlet of the porous plug using

$$\rho = \frac{PM_{H_2O}}{RT} \tag{5.3}$$

The Knudsen number through the porous plug is calculated using Equations 4.18 and 4.19. It *is* possible that the flow of an individual water molecule is greater than the values used in these calculations, but not enough to make a significant difference in mach number. The two plots below show the Mach number of the flow throughout the depth of the porous plug, from the inlet to the outlet, all of which is well below $\mathcal{M} = 0.3$. In Figure 5.16, the Mach number is plotted over the Knudsen range that describes the flow (diffusion) through the porous plug, illustrating the very low speed nature of the flow. The Knudsen number is cut off at $Kn = 100$, even though the Knudsen number of the water vapor at the porous plug outlet is up to two magnitudes greater. This is because at such rarefied flows, the mach number holds little meaning; speed of sound cannot really exist if there is no continuous medium through which the energy can travel. In summary, the experimental data can be appropriately used to validate the rarefied diffusion model outlined in Chapter 4.

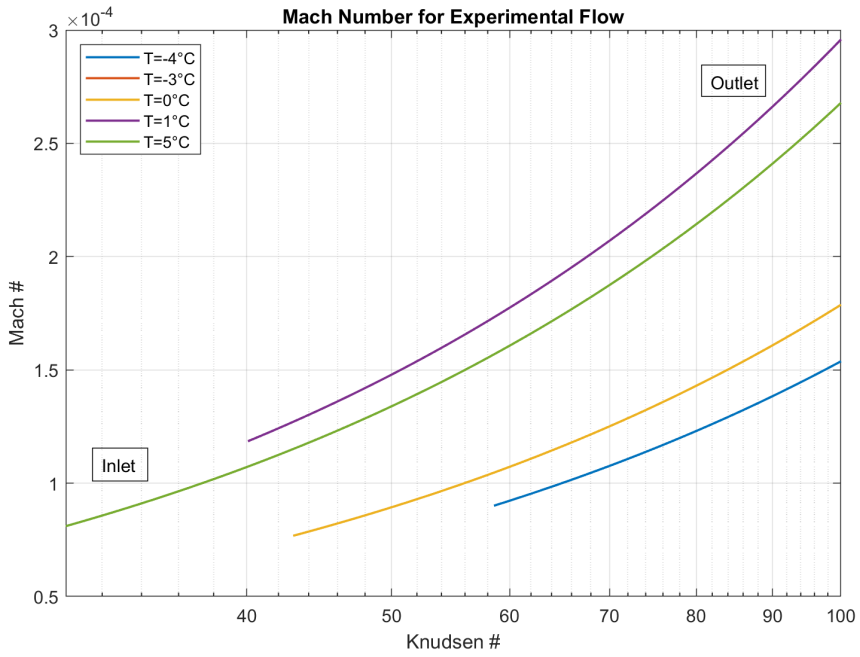

Figure 5.16: Mach number versus Knudsen number along the porous plug for each set of temperature trials.

5.2.4.4 Observation #1: Adiabatic

The vapor diffusion is adiabatic (no heat transfer between the flow and its surroundings), as observed in the temperature measurements. There is no significant difference between the temperature of the water vapor flow in the filter (measured with probes at the upstream and downstream sides of the flow section) and the external temperature of the tubing, measured with thermocouples taped to various locations on the tubing. Figure 5.3 shows the locations of the two temperature probes upstream and downstream of the filter and the two external thermocouples, as well as the five thermocouples inside the vacuum chamber. Figures 5.18 and 5.17 show the average thermocouple temperature measurement for the filter (two measurements), long tube (two external measurements), and vacuum chamber (5 measurements) for all 11 trials. Note that error bars are not shown on these plots; the plots are meant to show the proximity in temperature for all the measurements to illustrate the adiabatic nature of the flow. The y-axis for all the plots spans 2.5 degrees near room temperature and the difference between the filter, long tube, and vacuum chamber are within one degree. This small difference is often within the measurement confidence interval, as is discussed in more

detail later in this section.

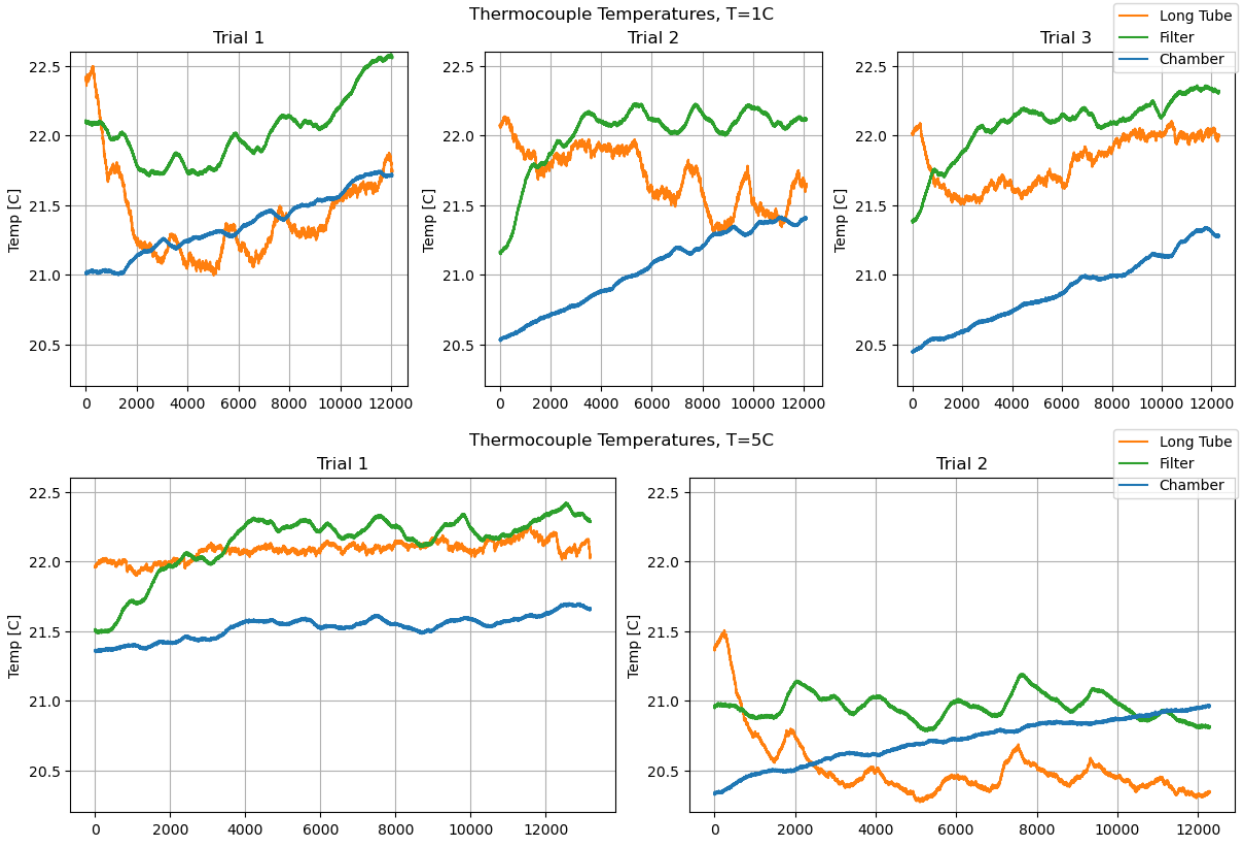

Figure 5.17: Continuation; thermocouple temperatures in support of validity of adiabatic assumption. Note the y-axis range is only 2.5 degrees and the confidence intervals are not shown.

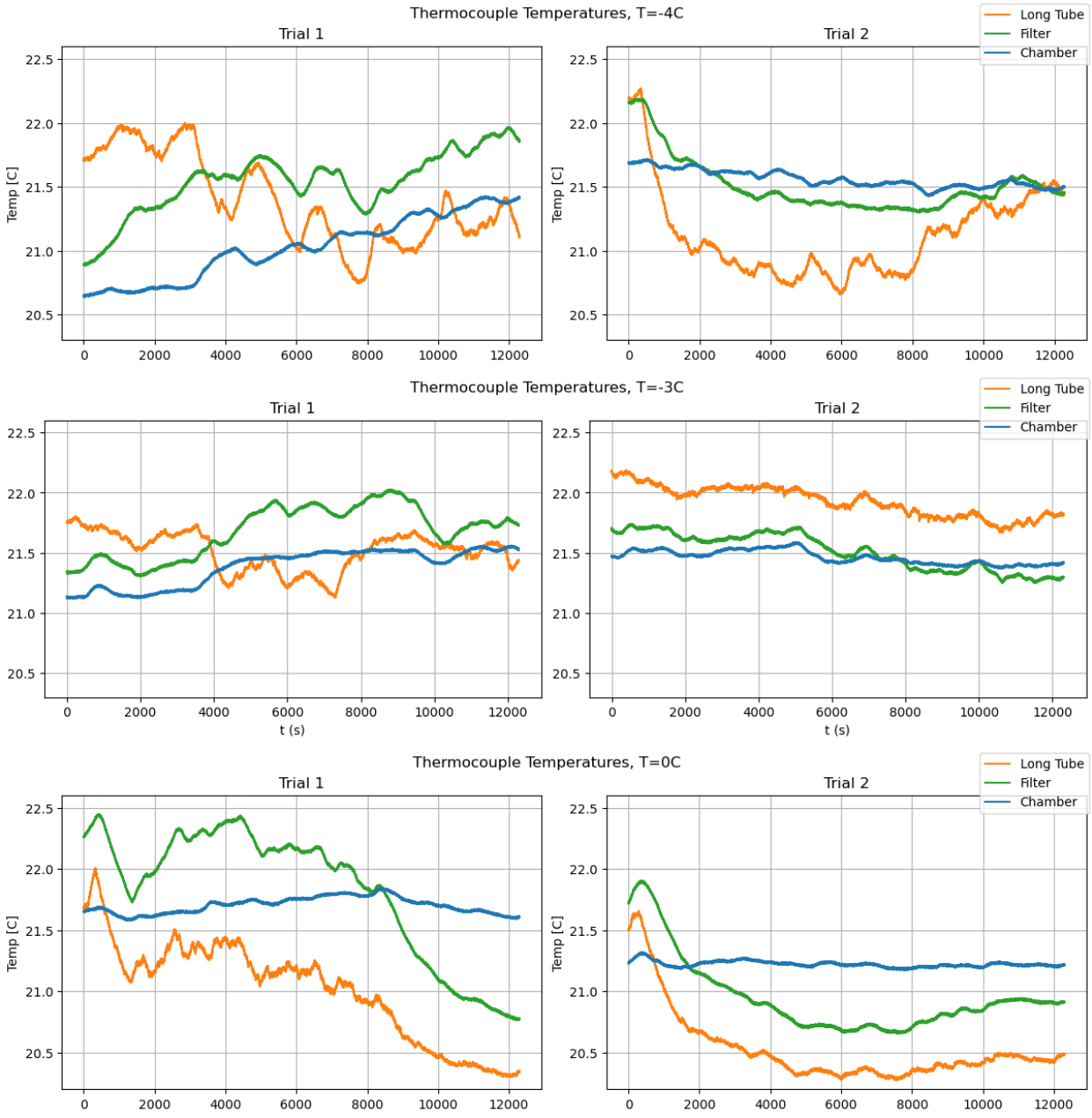

Figure 5.18: Thermocouple temperatures in support of validity of adiabatic assumption. Note the y-axis range is only 2.5 degrees and the confidence intervals are not shown.

5.2.4.5 Observation #2: Isenthalpic

If a flow is considered an ideal gas, at low speeds, and isothermal, then it will be isenthalpic, rendering this observation redundant [23]. Adiabatic flow going through a "restrictor" or throttling valve, such as the porous plug, is isenthalpic- another reason why this observation is somewhat redundant. That being said, it is important to understand the nature of this

vapor flow from many perspectives, and temperature-pressure-enthalpy relations can be used to verify the validity of the ideal gas assumption. Table 5.7 shows the difference between measured and idealized outlet temperature for each trial. The first two columns, T_{sat}, show the 11 trials for the water vapor saturation temperatures between $-4°C$ and $+5°C$. The median values of the measured T_{inlet} and p_{inlet} are taken over the trial duration, and the associated enthalpy, h_{lv}, is found from NIST's *MiniRefProp* database using the inlet conditions [18]. The median of the measured p_{outlet} is also taken over the trial duration. Then, the outlet pressure and enthalpy from MiniRefProp are used to find the expected ideal $Toutlet$ *as if the flow were isenthalpic*. The median of the measured T_{outlet} is taken over the trial duration and compared to the expected outlet temperature. The ΔT between the measured and expected outlet temperature is indicative of the validity of the isenthalpic, ideal gas, and isothermal assumptions. Table 5.7 shows the measured and computed values for the aforementioned approach, the result of which is a temperature difference between the measured outlet temperature and idealized outlet temperature of less than $\pm 0.5°C$, which supports these assumptions and observations.

Table 5.7: Temperature - pressure - enthalpy comparison for ideal gas and superheated water vapor in experiment.

$T_{sat}[°C]$ **(Goal)**		T_{inlet} Meas. $[°C]$	P_{inlet} Meas. $[Pa]$	h_{lv} Ideal $[*10^6 J/kg]$	P_{outlet} Meas. $[Pa]$	T_{outlet} Ideal $[°C]$	T_{outlet} Meas. $[°C]$	ΔT $[°C]$
-4	1	21.711	453.9	2.5416	18.91	21.581	21.429	0.152
-4	2	21.632	437.4	2.5415	18.64	21.527	21.250	0.277
-3	1	21.737	501.7	2.5417	20.26	21.635	21.722	-0.087
-3	2	21.657	481.1	2.5415	19.80	21.528	21.404	0.124
0	1	21.881	607.6	2.5419	22.905	1.743	22.151	-0.408
0	2	20.913	607.2	2.5401	22.934	20.777	20.852	-0.075
1	1	22.039	650.4	2.5422	23.955	21.904	21.936	-0.032
1	2	22.187	651.8	2.5424	23.997	22.012	21.971	0.041
1	3	22.202	651.8	2.5425	23.948	22.065	22.041	0.024
5	1	22.233	863.1	2.5424	28.56	22.013	22.181	-0.168
5	2	21.033	862.2	2.5402	28.69	20.832	20.869	-0.037

5.2.5 Results: Pressure Drop

Figure 5.19 shows the pressure data for all eleven experimental trials, categorized into the five target saturation temperatures. ΔP was calculated by taking the difference between P_1, the upstream pressure, and P_2, the downstream pressure closer to the vacuum chamber, at every second. Note that the vacuum chamber presesure was constant and close to zero, so the plots in Figure 5.19 absolute upstream pressure measurement, p_1. There are a few notable observations:

- As expected, the colder the water vapor saturation temperature, the lower the saturation (upstream) pressure and the smaller the ΔP.
- There is an obvious transient period in the beginning of each trial for the first 500-1500 seconds (about 8-25 minutes). This is discussed in more detail in Section 5.2.7.
- In $T_{sat} = -3°C$, Trial 1, the pressure steadily and continuously decreases because the water chiller temperature had not fully stabilized so it was still cooling down. That being said, the relationship between pressure drop and mass flow rate can still be obtained.

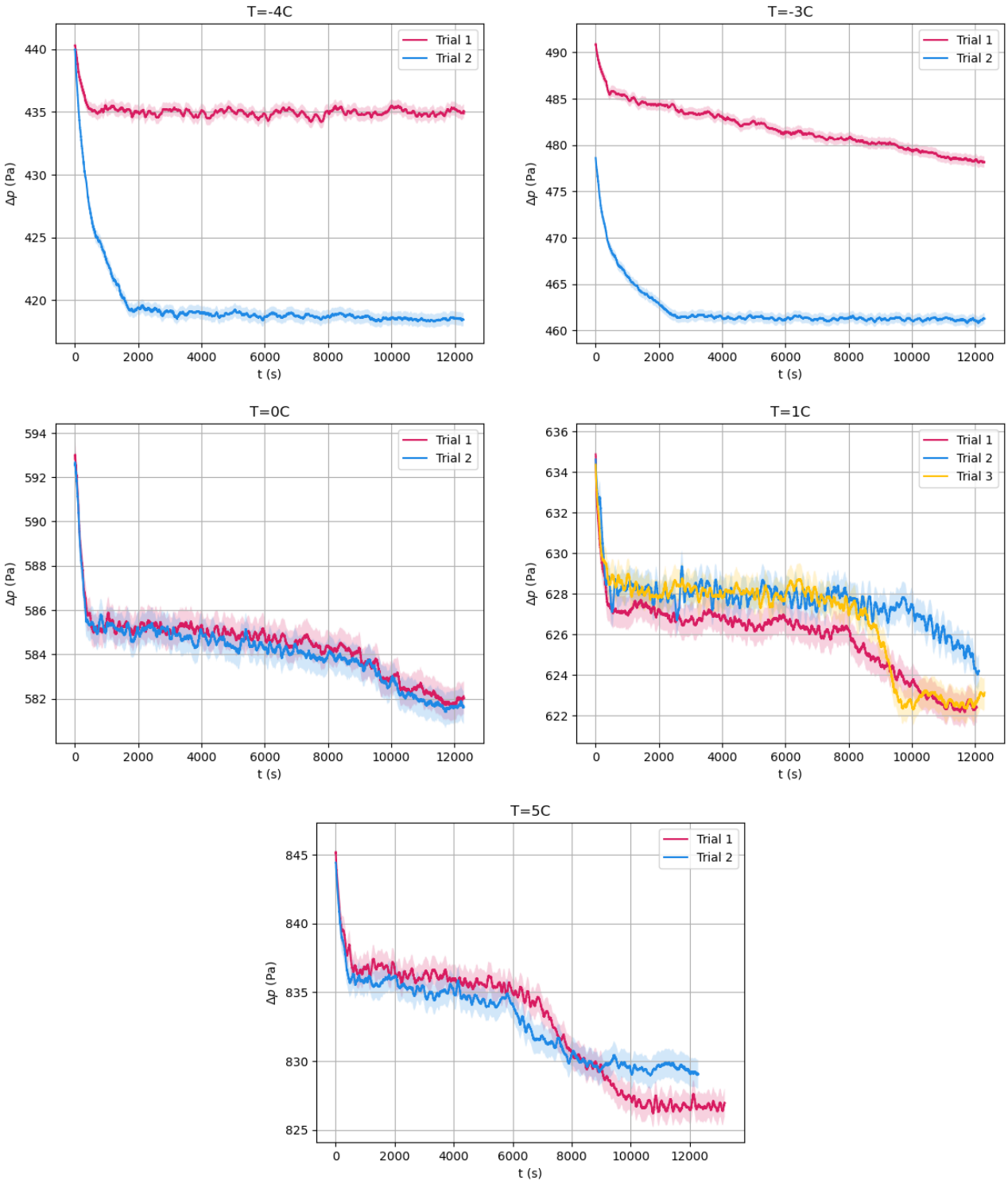

Figure 5.19: Pressure drop across filter porous plug.

In the trials where $T_{sat} \geq 0°C$, there is a minor experiment artifact: a drop-off part-way through each trial duration. The larger the saturation temperature/pressure, the earlier on

the drop-off occurs and the larger the decrease in pressure. The pressures should generally trend slightly downward because the system is being actively pumped on, slowly lowering the saturation pressure over time. Note that the y-axis ranges in Figure 5.19 are zoomed-in; if the axes instead started at 0 Pa, this drop-off would not be apparent because the pressure drop-off is less than 1% of the measured pressure values. Figure 5.20 shows the region of interest when comparing "before" and "after" the sudden pressure drop.

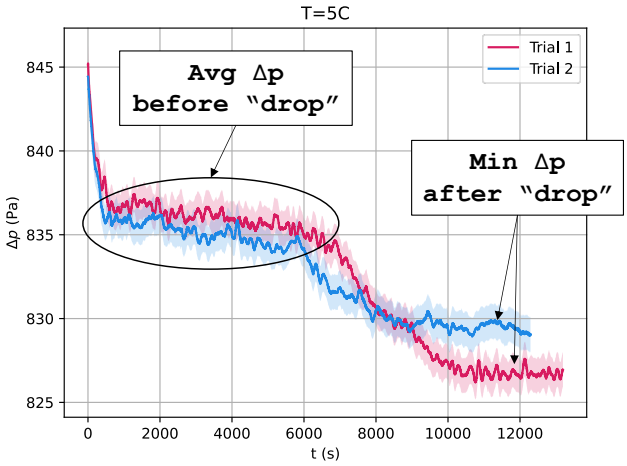

Figure 5.20: Pressure drop across filter porous plug ($P_1 - P_2$ from experiment schematic) with labels pointing to the "pressure drop phenomena".

We have no explanation of this observed decrease in pressure, so the effect of that drop-off must be demonstrably negligible. Table 5.8 show the values associated with each of those regions with the small numerical and percentage differences. These differences would not translate into any detectable change in mass flow rate with the scale used in this experiment.

Table 5.8: Difference in ΔP in the beginning versus end of trials.

T_{sat} [°C] (Target)	Trial	Avg ΔP [Pa] before "drop"	Min ΔP [Pa] after "drop"	Difference [Pa]	Difference %
0	1	585.3	582.0	3.33	0.57%
0	2	585.3	582.0	3.33	0.57%
1	1	627.3	622.6	4.67	0.74%
1	2	628.6	623.9	4.67	0.74%
1	3	628.6	622.6	6.00	0.95%
5	1	836.6	826.6	10.00	1.20%
5	2	835.9	829.3	6.67	0.80%

5.2.6 Results: Saturation Temperature Comparison

This experiment involves the measurement of temperature to find pressure at saturation conditions, and vice-versa. Therefore, the saturation temperature and pressure must be verified prior to an experimental trial. This verification ensures there are no non-condensable gases remaining in the experimental set-up (i.e. from the atmosphere) or entrapped air in the water. Prior to every trial, the relationship between p_{sat} and T_{sat} was verified to within an acceptable error.

Figure 5.21 shows data for all eleven experimental trials, categorized into the five target saturation temperatures. The measured temperature did not always match the target temperature because it was difficult to control the water vapor saturation temperature via the chiller bath temperature. Each plot shows (1) the temperature of the water vapor as measured from the PRT probe taped to the outside of the water reservoir (as in Figure 5.5) in solid lines and (2) the *calculated* T_{sat} of the water vapor using the upstream pressure measurement (P1 in Figure 5.3) in dashed lines. The National Institude of Standards and Technology (NIST) database [18] was used to calculate the expected water vapor temperature from measured vapor pressure, so there was no need to compute the propagation of error in the nonlinear Clausius-Clapeyron Equation 4.15. Note that the error band for the PRT temperature measurement is significantly greater than the error band for the calculated T_{sat} because thermocouples (of which the PRT is a type) have significantly greater uncertainty than baratron capacitance manometers (pressure sensors), as described in Section 5.2.3.

When $T_{sat,goal} = -4°C$, in Trial 1 the measured temperature is *lower* than the calculated temperature, the maximum variation of all the trials, at $0.35°C$. In Trial 2 the measured temperature is slightly *higher* than the calculated temperature. When $T_{sat,goal} = -3°C$, in Trial 1 the measured temperature is *lower* than the calculated temperature. Both the measured and calculated temperature values steadily and continuously decrease because this trial began before the water cooler had stabilized. In Trial 2, the measured temperature is slightly *higher* than the calculated temperature. When $T_{sat,goal} = 0°C$ in Trials 1 and 2, $T_{sat,goal} = 1°C$ in Trials 1, 2, and 3, and $T_{sat,goal} = 5°C$ in Trials 1 and 2, the measured temperature is slightly *higher* than the calculated temperature.

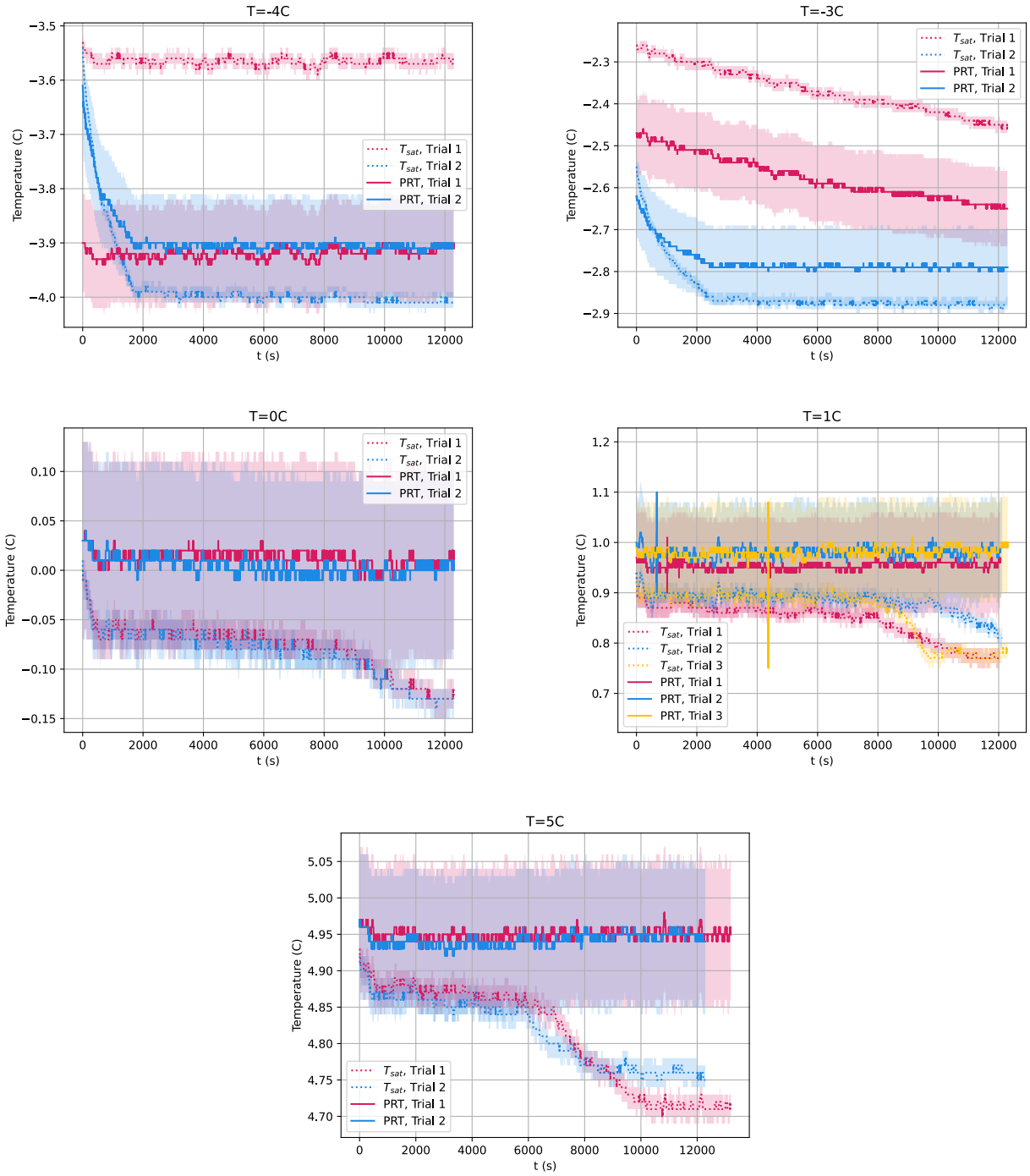

Figure 5.21: Water Reservoir Temperature: Measured from temperature probe and calculated from measured saturation pressure.

When the measured PRT temperature is higher than the calculated saturation temperature, the temperature difference is just within the PRT accuracy for most of the trial.

The difference can be attributed to the sensor locations: the pressure sensor is *directly*

upstream of the filter and the temperature sensor is outside the water reservoir, farther upstream. The discrepancies between the expected and measured temperatures (or, conversely, pressures) are expected because the sensor locations are several feet apart in the experimental set-up. In addition, the temperature probe is not placed directly in the vapor space in the water reservoir due to physical limitations of the experimental set-up. Instead, it is placed outside of the reservoir so it does not capture any evaporation interface cooling due to phase change, nor does it capture any temperature gradient within the liquid or vapor space in the water reservoir. This phenomena is reflected in most of the experimental trials where the measured temperature (near the filter) is slightly higher than the calculated temperature (in the water reservoir).

Occasionally, the measured vapor temperature (solid lines) is lower than the calculated vapor temperature (dashed lines). For the first four experimental trials ($T_{sat,goal} = -3°C$ and $T_{sat,goal} = -4°C$), there was an ethanol-water mixture used in the chiller bath to prevent the circulating fluid from freezing at below-zero temperatures. The chiller bath needed to be set to a temperature $0.15°C$ cooler than the target vapor temperature, so the PRT was biased cold because the probe was partially exposed to this chiller fluid. In addition, there was likely a spatial temperature gradient in the chiller bath itself, not just inside the water reservoir as previously mentioned. The tube from which the circulating fluid exited was near the PRT probe in the lower half of the chiller bath so the cooler water was likely near the bottom and the warmer water would be expected near the top of the chiller bath.

Even though there are some slight discrepancies between the saturation temperature and pressure data, most of them are within the uncertainty range. The discrepancies can be attributed to experimental set-up, operation, and cooling phenomena in the chiller bath and/or the evaporation interface. The measured ΔP and $\dot{m}$ can still be used to obtain important relationships for both model and assumption verification purposes.

5.2.7 Results: Mass Flow Rate & Steady-State Assumption

The mass flow rate measurement is only valid if the flow reaches steady-state after a relatively short transient period. After showing a table and plot of the Δm values, the validity of the steady-state assumption is explored.

Table 5.9: Mass flow rate data.

Trial	T_{sat} $[°C]$ **(Target)**	**Measured** T_{sat} $[°C]$	Δm [g]	Δt [s]	$\Delta m/\Delta t$ $[*10^{-8} kg/s]$
1	-4	-3.9	0.33	12600	2.619
2	-4	-3.9	0.47	12600	3.730
1	-3	-2.55	0.41	12600	3.254
2	-3	-2.8	0.52	12600	4.127
1	0	0.02	0.43	12600	3.413
2	0	0.02	0.50	12600	3.968
1	1	0.95	0.82	12339	6.646
2	1	1	0.77	12420	6.200
3	1	1	0.69	12600	5.476
1	5	4.95	0.83	13520	6.139
2	5	4.95	0.62	12600	4.921

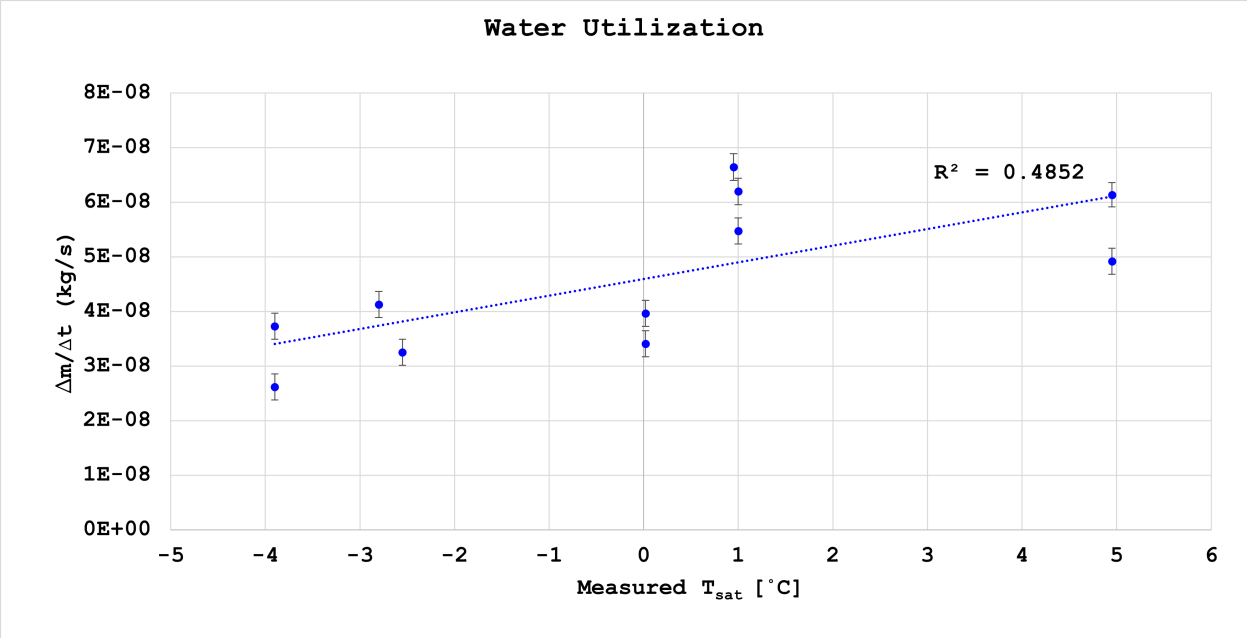

Figure 5.22: Mass flow rate for all experiment trials.

Although there is a linear fit in Figure 5.22, any trend is not immediately obvious. This is because the Knudsen numbers are greater than the Knudsen minimum ($Kn = 0.8$) so the relationship between mass flux and pressure is counter-intuitive: the mass flux may decrease with an increase in pressure. There is a spread of mass flow rate over the entire collection range: some data points at the *lowest* T_{sat} are very close in value to the mass flow rate data points from the *highest* T_{sat} trials. This may be the effects of non-continuum flow, where an

increase in mass flux is seen at smaller pressures.

The duration of the transient period and its affect on the measured water mass loss is captured by looking at the Δp plots in Figure 5.23. For most trials, the transient period was small and for a couple trials ($T_{sat} = -4°C$, Trial 2 and $T_{sat} = -3°C$, Trial 2), the transient period was more significant. In $T_{sat} = -3°C$, Trial 1, the water in the reservoir (the water vapor source) was still cooling to a steady-state so there is a slight decrease in saturation pressure and the Δp measurement throughout the duration of the trial. That being said, there was still an obvious transient period. In Figure 5.23, the area of the yellow triangle compared to the entire area under the ΔP - t curve is small, which is shown numerically in Table 5.10. For almost all the experimental trials, the fraction of the total mass used in the transient time frame is small, so steady-state flow can be assumed.

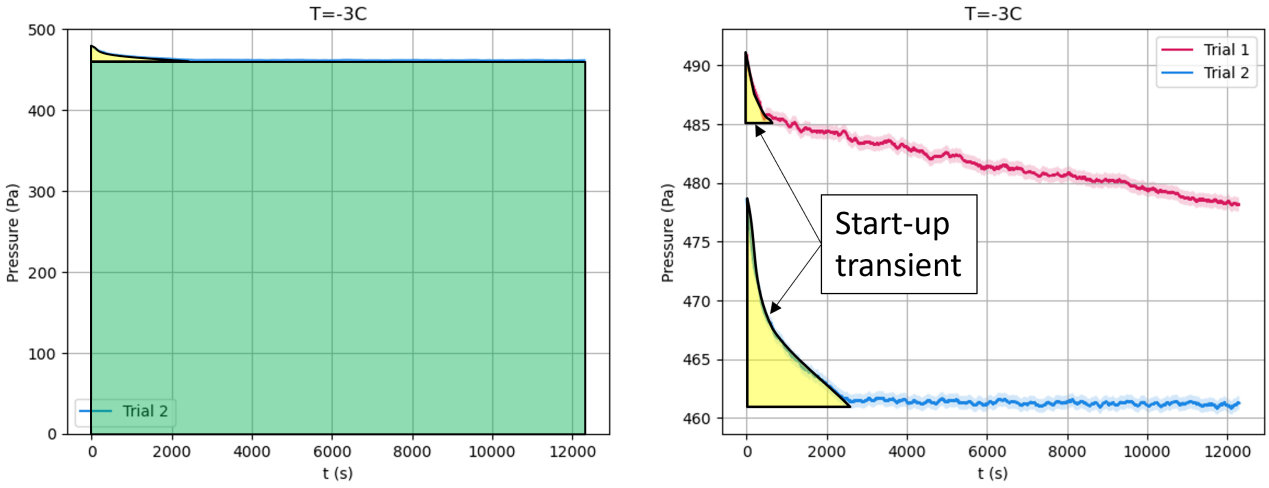

Figure 5.23: Pressure drop across porous filter for $T_{sat} = -3°C$, Trial 2. The green rectangle on the left figure shows the steady-state region and the yellow triangle on both plots show the transient region.

Table 5.10: Extra mass of water utilized during transient period.

T_{sat} [°C] (Target)	Trial	Mass Util. (transient) [g]	Total Mass Utilized [g]	%
-4	1	0.01074	0.33	3.3
-4	2	0.06218	0.47	13.2
-3	1	0.01346	0.41	3.3
-3	2	0.10663	0.52	20.5
0	1	0.01752	0.43	4.1
0	2	0.02038	0.50	4.1
1	1	0.02723	0.82	3.3
1	2	0.02541	0.77	3.3
1	3	0.02243	0.69	3.3
5	1	0.01960	0.83	2.4
5	2	0.02447	0.62	3.9

5.2.8 Results: Mass Flow Rate - Pressure Drop Ratio

For each trial, the ratio of mass flow rate to pressure drop was computed from measured data. As seen in Figure 5.19, the measured pressure drop across the filter's porous plug often had a detectable but not significant change, so the **median pressure** for each trial was used in the $\frac{\dot{m}}{\Delta P}$ calculation. Figure 5.24 shows the mass flow rate/pressure ratio versus inlet pressure (which is also the saturation pressure of the water vapor). The leftmost points correspond to the lowest saturation temperatures and the rightmost points correspond to the largest saturation temperatures.

The two data points for $T_{sat} = 5°C$ are slightly lower than the rest of the data points due to "continuum effects". Considering the mean free path calculation at the upstream end of the porous plug ($p = 866Pa$) and superheated temperature ($T = 21°C$), the calculated mean free path is $\lambda = 15.02\mu m$. Using the largest reported pore size ($d_{max} = 2\mu m$), the Knudsen number is $Kn = 7.5$ which is in the transition flow regime rather than the rarefied flow regime. It is apparent that the mass flow rate shown in Figures 5.22 and 5.24 are slightly lower than expected for the highest saturation temperature. While the transition flow regime is not considered continuum, the water vapor flow in the porous plug also may not be completely rarefied, reducing the flow rate. As discussed in Section 4.7.1, the Knudsen

minimum occurs near the boundary between transition and free molecular flow during which the mass flux "reaches a minimum value and then increases with decreasing pressure" [100]. The data points from the trial at the highest saturation pressure are near the Knudsen minimum which is characterized by a smaller mass flow rate.

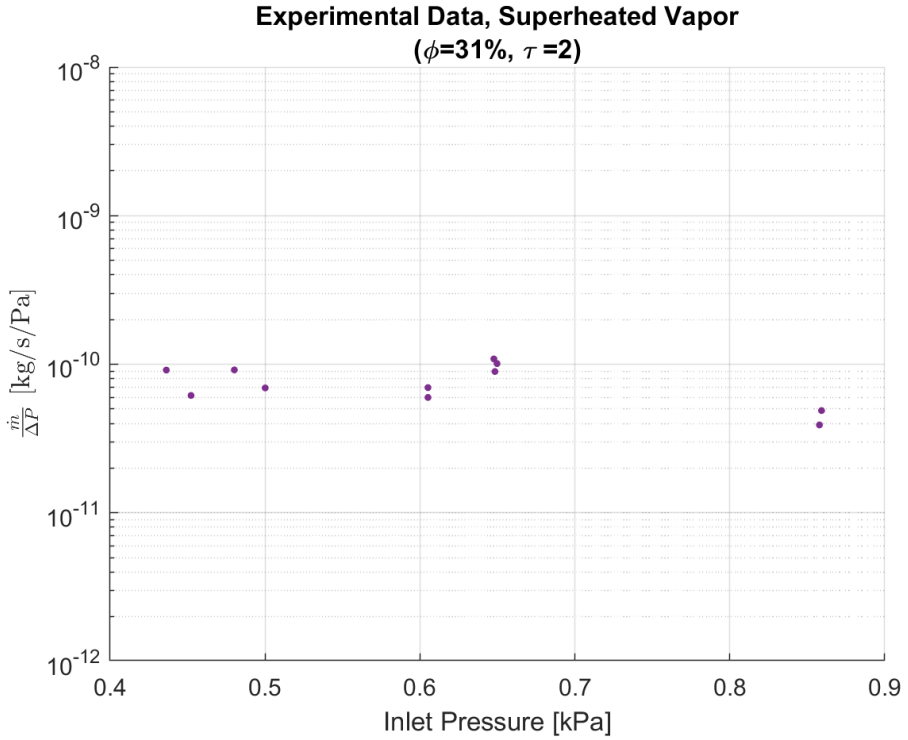

Figure 5.24: Mass flow rate per pressure drop for all experimental trials. Note that confidence interval is not visible on the logarithmic scale.

Table 5.11: Experimental Data of $\frac{\dot{m}}{\Delta P}$

T_{sat} [°C] (Target)	Trial	$\frac{\dot{m}}{\Delta P} * 10^{-11}$ [kg/s/Pa]
-4	1	6.17
-4	2	9.14
-3	1	6.93
-3	2	9.16
0	1	5.98
0	2	6.96
1	1	10.85
1	2	10.11
1	3	8.93
5	1	3.9
5	2	4.88

5.3 Lessons Learned

The lessons outlined in this section were learned during the experiment and should be emphasized in future rarefied flow experiments.

- The importance of purging with nitrogen.
  - Add N_2 purge valve as far upstream as possible to purge the entire system between trials. This also helps eliminate any lingering non-condensable gases from the system.
  - Add N_2 purge directly to roughing pump and continue to purge it throughout entire trial to prevent over-saturating pump. Importance of relief valves whenever there is a glass element to prevent breaking.
- Importance of checking that the water vapor source (in the reservoir) is at saturation conditions.
  - When comparing p_{sat}-T_{sat}, if the pressure is higher than expected for a given temperature, there are non-condensable gases in the system. If the pressure is lower than expected, then it most likely means that the vapor inside the reservoir is colder than what the pressure sensor implies.
- Importance of degassing to eliminate non-condensable gases and ensure p_{sat}-T_{sat} match.
  - Evaporate water at high temperatures for a more aggressive degassing process and measure p_{sat} at low temperatures (and p_{sat}) for more accurate measurements.
- When weighing the water reservoir, make sure the outside is completely dry and place in an air oven because there may be a few drops of water on the outside contributing to a higher value.
- After all the vacuum fittings have been tightened, perform a leak check. This was done using a helium leak detector.
- Place a scale in an enclosed space to avoid any air flow disturbing the tare.

5.4 Future Improvements

While the experiment conducted is considered successful, the following list includes improvements which could be made in the future to decrease uncertainties and discrepancies and make the data collection process more efficient.

- Measure the temperature of the vapor space in the water reservoir more directly, rather than an externally-mounted PRT.
- Ensure the chiller temperature has stabilized before starting each trial. This is especially important if the water in the reservoir needs to undergo a phase change, like if it is starting at room temperature and needs to reach freezing temperatures.
- Conduct each trial for a longer period for more precise mass measurements. Each trial should be 10 hours instead of 3.5 hours.
- Use a higher concentration of ethanol in the chiller's ethanol/water mixture to ensure the circulating fluid does not freeze on the pipes in the chiller.
- Use a reservoir shaped differently to reduce the temperature gradient through the liquid region. This would be helpful only if it is not possible to have a more direct measurement of the temperature in the vapor space.
- "Pre-evacuate" reservoir and then draw water into the reservoir via a vacuum. This ensures there are fewer non-condensable gases in the water reservoir before it is filled.

This chapter discussed the use of porous media samples to gain a better understanding of the physical parameters used to describe the porous microstructure and the water vapor flow experiment to gather experimental data for validating one aspect of the sublimator model which can apply to both evaporation and sublimation. The next chapter compares the experimental data to the analytical model for water vapor diffusion through porous media.

Chapter 6

Model Validation

The assumptions made to validate the Weber Equation were addressed in the previous chapter and are summarized here:

- Ideal gas: The water vapor can be considered an ideal gas because the compressibility factor is nearly 1 and the Joule-Thomson coefficient is nearly 0 (Section 5.2.4.1).
- Isothermal: The temperature of the water vapor is virtually unchanging throughout each trial (Section 5.2.4.2).
- Low Mach Number: The flow has a low mach number as it exits the porous plug — the speed of sound is magnitudes greater than the water vapor velocity as it exits the porous plug (Section 5.2.4.3).
- Steady-state: The amount of water vapor that flowed during the transient period is negligible compared to the water flowed during steady-state (Section 5.2.7).

The observations made about the experimental data, which add insight to its use in validating the Weber Equation, are summarized here:

- Adiabatic: There is no change in temperature of the water vapor which suggests negligible heat transfer (Section 5.2.4.4).

- Isenthalpic: Comparing the temperature, pressure, and enthalpy of vaporization from the National Institute of Standards and Technology (NIST) and measured during the experiment demonstrated this assumption is valid (Section 5.2.4.5).

6.1 Ideal Gas Assumption for a CubeSat

The ideal gas assumption applies to the Weber Equation, to the experimental data, and to a realistic CubeSat sublimator in which the water vapor is near saturation and not superheated. Table 6.1 shows Z and μ_J for the water vapor in the CubeSat sublimator and both values support the ideal gas assumption. Thus, the Weber equation and experimental results can be compared to water vapor in a realistic sublimator.

Table 6.1: Compressibility Factor and Joule-Thomson Coefficient for near-saturation water vapor in experiment [18].

T_{sat} [C]	P_{sat} [Pa]	**Vapor Compress. Factor (Z)**	**Joule-Thomson Coeff [C/Pa]**
-8	309.95	0.99964	0.00073098
-6	368.71	0.99959	0.00069386
-4	437.45	0.99954	0.00065851
-2	517.70	0.99949	0.00062485
0	611.15	0.99942	0.0005928
2	705.99	0.99937	0.00055623
4	813.55	0.99931	0.00052204
6	935.35	0.99924	0.00049015
8	1073.00	0.99918	0.00046042

6.2 Weber Equation & Experimental Data: Pore Size

Another means of validating the model is by calculating the pore size using Weber's equation. In Equation 4.20, the temperature and pressure variables come from the collected experimental data and the porous filter thickness and cross-sectional area come from manufacturer specifications. The *calculated* pore size is then compared to the *reported* pore size from the manufacturer. This calculation excluded the trials for $T_{sat} = 5°C$ because of the

continuum effects described in Section 5.2.8. The root mean square error (RMSE) of the difference between the calculated and manufacturer pore diameter is computed using

$$RMSE = \sqrt{\frac{\Sigma_{i=1}^{N} (x_i - \hat{x}_i)^2}{N}} \tag{6.1}$$

where N is the number of trials (9), x_i is the calculated pore diameter and $\hat{x}_i$ is the median of the manufacturer's reported pore diameter ($1.25\mu m$). The results are shown in Table 6.2. The range in calculated pore diameter is 0.92 μm to 1.72 μm and the reported pore diameter range from the manufacturer is 0.5 μm to 2 μm.

Table 6.2: Pore Size data for RMSE calculation.

Temp [C]	**Trial**	**Calculated Pore Diam. (x_i) [μm]**	**Avg. Mfr. Pore Diam. ($\hat{x}_i$) [μm]**	**Diff**	**% Diff**
-4	1	0.9480	1.25	-0.3020	24%
-4	2	1.4148	1.25	0.1648	13%
-3	1	1.0694	1.25	-0.1806	14%
-3	2	1.4222	1.25	0.1722	14%
0	1	0.9234	1.25	-0.3266	26%
0	2	1.0789	1.25	-0.1711	14%
1	1	1.7130	1.25	0.4630	37%
1	2	1.5906	1.25	0.3406	27%
1	3	1.3986	1.25	0.1486	12%
Avg Calc. x_i		1.2843			
RMSE		0.2726			

6.3 Weber Equation & Experimental Data: Mass Flow Rate - Pressure Drop Ratio

The next way in which the model is validated with experimental data involves comparing the mass flow rate-pressure drop ratio taken from experimental data to that from the Weber equation. Figure 6.1 shows this comparison where the purple dots are points from all 11 experimental trials and the three near-horizontal lines are the expected $\frac{\dot{m}}{\Delta p}$ based on the manufacturer's minimum, maximum, and mean pore diameter. Note that the mean pore

diameter is the numerical mean from the range and not a measured value. The experimental data is well within the expected range for $\frac{\dot{m}}{\Delta p}$.

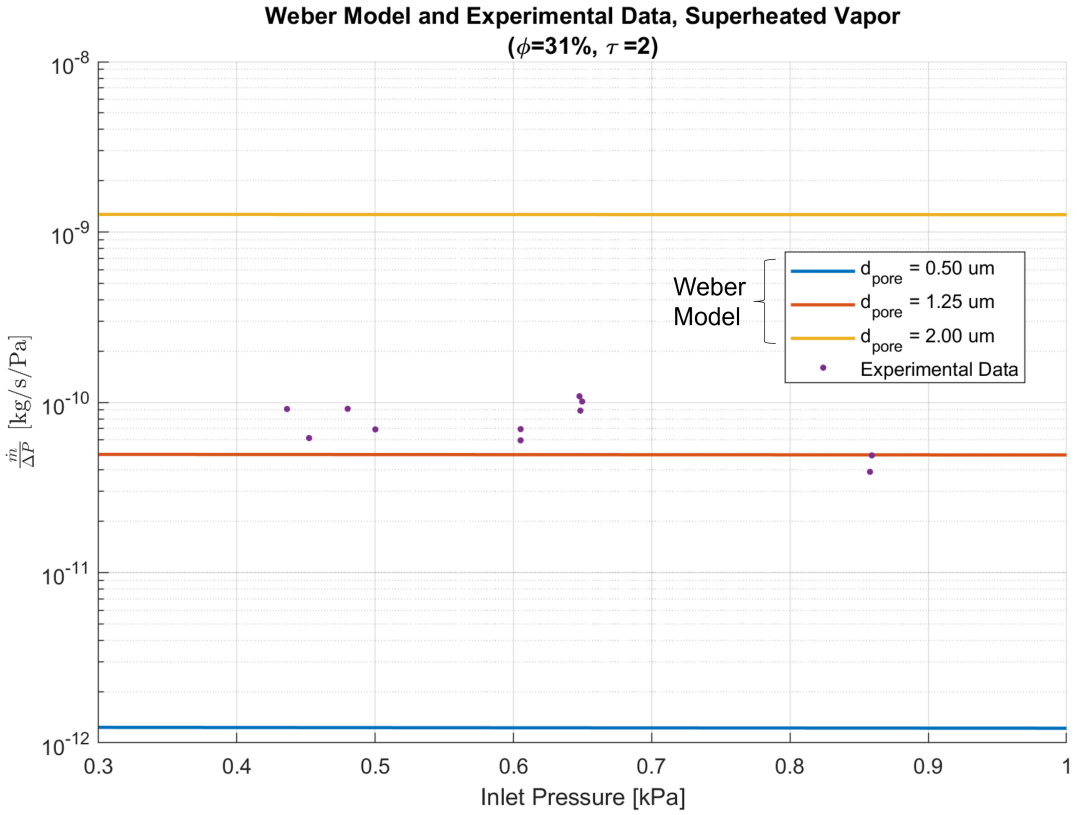

Figure 6.1: Mass flow rate/pressure drop ratio: comparison of Weber model to experimental data. The tortuosity value from PuMA and used in the Weber model is $\tau = 2$. Note that confidence interval is not visible on the logarithmic scale.

Figure 6.2 shows the same data as Figure 6.1 with Knudsen number on the x-axis. The Knudsen numbers are computed for the same 11 data points based on the three different pore sizes across the manufacturer range. While this data appears more skewed, it tells the same story. The blue points representing the median pore size are closest to the corresponding $\frac{\dot{m}}{\Delta p}$ from the model.

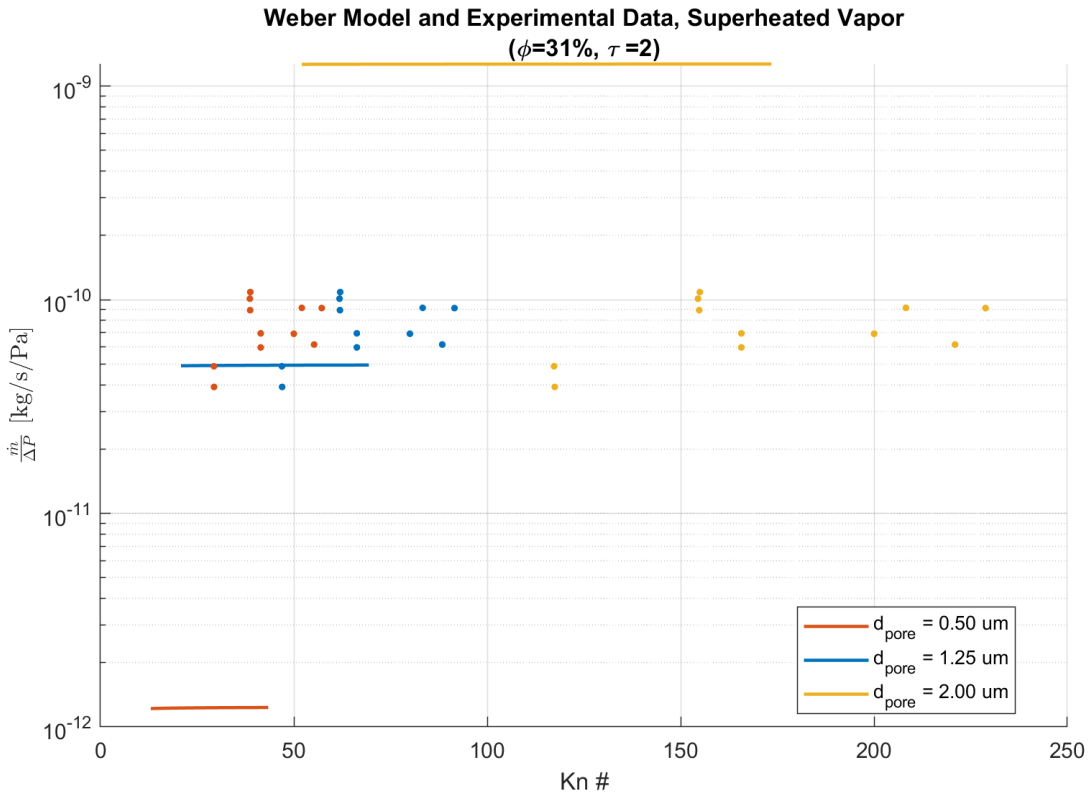

Figure 6.2: Comparison of Weber model to experimental data in terms of Knudsen number. Note that confidence interval is not visible on the logarithmic scale.

6.4 Comparison: Historical & Experimental Data

The last approach to verify that the Weber equation can be used to model rarefied water vapor flow through a sublimator is to compare to historical data in Table 6.3. Equation 4.20 was rearranged to solve for the effective length:

$$l = \Delta p \frac{r^3}{\dot{m}} \frac{4}{3} \sqrt{\frac{2 m_{H_2O} \pi}{k_B T}} \left[\frac{3\pi}{128} \left(\frac{2r}{\lambda} \right) + \frac{\pi}{4} \left(\frac{2r/\lambda}{1 + 2r/\lambda} \right) + \left(\frac{1}{1 + 2r/\lambda} \right) \right] \tag{6.2}$$

and the inputs to this equation are from the available historical data. In this case, the geometric or diffusion tortuosity values are not considered because it was not a measured characteristic of the porous medium, either in the experiment or past sublimator hardware. The reported pore radius and saturation temperature/pressure were used to calculate the Knudsen number. In the historical cases used here, the saturation temperature and pressure were assumed to be at or near the triple point of water ($-1° \rightarrow 0°C$, $611\ Pa$). Table 6.3

shows this comparison with data taken from the sources previously cited in the literature review for the EMU [16, 35], contaminant insensitive sublimator [20, 37] and the sublimator driven cold plate [46]. Note that the two values in red, from an Apollo-era researcher, are a result of the mass flow rate being unusually low [15]. The mass flow rate was computed from reported heat flux and area data from an experiment using the phase change heat transfer Equation, Eq. 1.4. The reported heat flux values are unusually low but there is no follow-up data or discussion found in the literature. In Zhang et al.'s research with CFD and an experiment for the CNSA, the 7% vapor space percentage agrees with what the authors call "void height" during steady-state sublimator operations [52]. In Leimkuehler's work from 2006, the contaminant insensitive sublimator contained pore sizes small enough to enable vapor pressure drop and larger enough to enable sublimation while preventing particulate build up. Overall, there is reasonably good agreement between the historical vapor length and Weber's predicted values using historical inputs. Most data from Table 6.3 shows the vapor space occupies a small fraction of the porous medium, but additional exploration is required to understand the differences in these historical data.

Table 6.3: Historical data and Weber equation.

								Notable Parameters			
Author, Date	Area [m^2]	Thickness [mm]	T_{sv} [°C]	Assumed Δp [Pa]	r [μm]	ϕ	$\dot{m}$ [kg/s]	Kn	Heat Rejection [W]	Vapor Region Thickness [μm]	% of Porous Media
Chapman, 1971	0.01674	2.0	-1	568	2.5	0.1	3.35E-06	8	8	664	33%
	0.01675	2.0	-1	568	5	0.1	3.35E-06	4	8	1313	66%
	0.01676	2.0	-1	568	2.5	0.31	3.35E-06	8	8	2057	103%
	0.01677	2.0	-1	568	5	0.31	3.35E-06	4	8	4070	204%
EMU Reqs, Rev B, 2005	0.0348	2***	-1	568	1	0.07	1.26E-04	21	315	10.3	0.52%
	0.0349	2.0	-1	568	3	0.07	1.26E-04	7	315	30.6	1.53%
	0.0350	2.0	-1	568	1	0.5	1.26E-04	21	315	74.1	3.7%
	0.0351	2.0	-1	568	3	0.5	1.26E-04	7	315	219.0	11%
	0.0352	2.0	-1	568	1	0.07	3.78E-04	21	945	3.4	0.17%
	0.0353	2.0	-1	568	3	0.07	3.78E-04	7	945	10.2	0.51%
	0.0354	2.0	-1	568	1	0.5	3.78E-04	21	945	24.7	1.2%
	0.0355	2.0	-1	568	3	0.5	3.78E-04	7	945	73.0	3.7%
Leimkuehler, 2006	0.2689	3.2	-1	568	5	0.3	4.25E-03	4	10625	3	0.09%
RaviPrakash et al, 2008	0.13	1.588	-1	568	2.5	0.3	1.72E-04	8.4	430	300.5	19%
	0.13	1.588	-1	568	2.5	0.3	1.47E-03	8.4	3670	35.1	2.2%
Sheth, et al. 2010	0.01952	2.0	-1	568	3*	0.2*	3.85E-04	7	962	107.1	5.36%
Zhang et al, 2020	0.03	1.0	-1	568	2.5	0.31	1.74E-04	8.4	435	71	7.10%

* Guess - parameter not reported

** Author distinguishes between mass flow rate for feedwater and sublimation, so the value used was obtained from reported heat flux

*** From CAD drawings

6.5 Realizability of Sublimator Design Parameters

As mentioned in Section 4.4, the coldest coldest possible phase change temperature for a nominally operating sublimator is $T_{sv} = -2°C$. The plots in Figure 6.6 show the physically possible, *realizabile* ranges for pore size and porosity given an interface temperature between $-2°C$ and $1°C$. The possible pore size and porosity values are influenced by T_{sv}: the closer the sublimation temperature is to the triple point of water, the more flexible the sublimator design. The sublimator temperature, however, is not a controlled design point. Rather, these plots indicate that the sublimation temperature is likely very close to the triple point based on the wide range in heat flux used with historical sublimator designs. These plots were obtained by repeating the process described in Section 4.8 where the conduction and rarefied vapor flow models were combined to obtain temperature and pressure distributions through the sublimator. For each of the six distinct T_{sv} values in the six plots in Figure 6.6, the dimensions for the feedwater, ice, and vapor regions were obtained. Figures 4.20 and 4.23 show examples of sublimator design parameters which yield realizable temperature distributions and phase change locations, repeated here for reference.

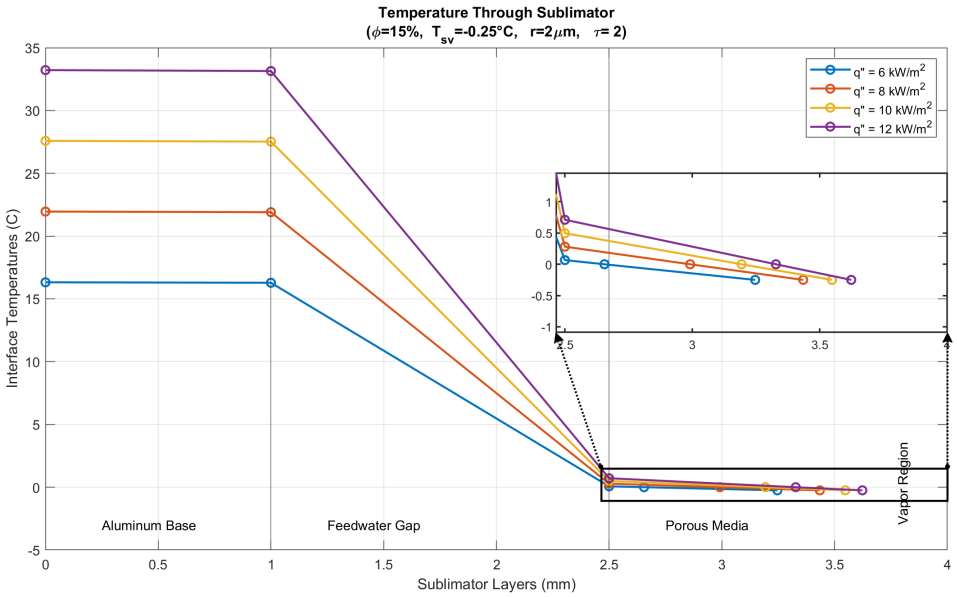

Figure 4.20: Temperature profile within sublimator which incorporates both the solution to the conduction equations and the Weber equation.

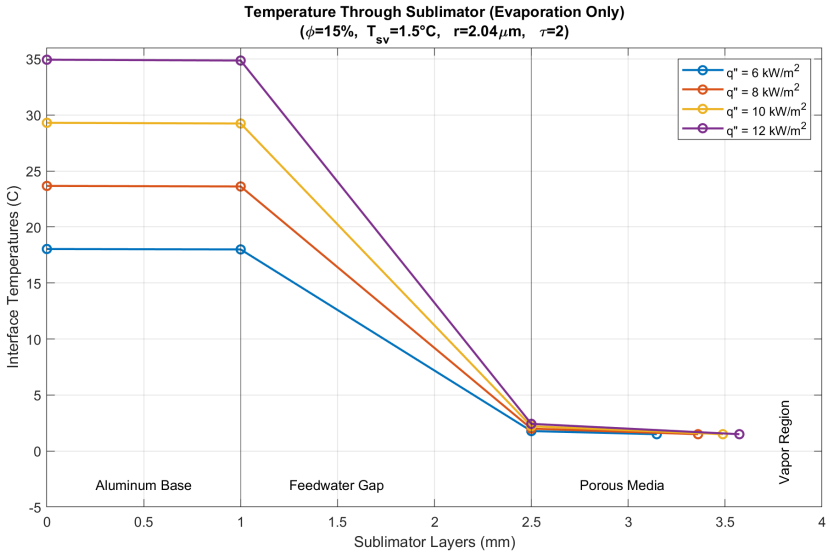

Figure 4.23: Temperature profile within sublimator which incorporates both the solution to the conduction equations and the Weber equation for the evaporation case [104].

If the combined ice and vapor regions sum to more than the thickness of the porous medium itself, then that specific pore size/porosity configuration was deemed not physically possible, or not realizable. If a sublimator were to be designed with a combination of pore size and porosity that is not in the shaded regions, then anomalies may be more likely to occur, such as feedwater breakthrough. Figure 6.5 shows an example of a sublimator design which is *not* realizable: notice that with the selected porosity and pore size, for $q" = 6\ kW/m^2$ and $q" = 8\ kW/m^2$, the temperature of the feedwater reaches the freezing point in the feedwater gap, not within the porous medium. As a result, the locations and thicknesses of the liquid, ice, and vapor regions do not fit within the dimension of the porous component.

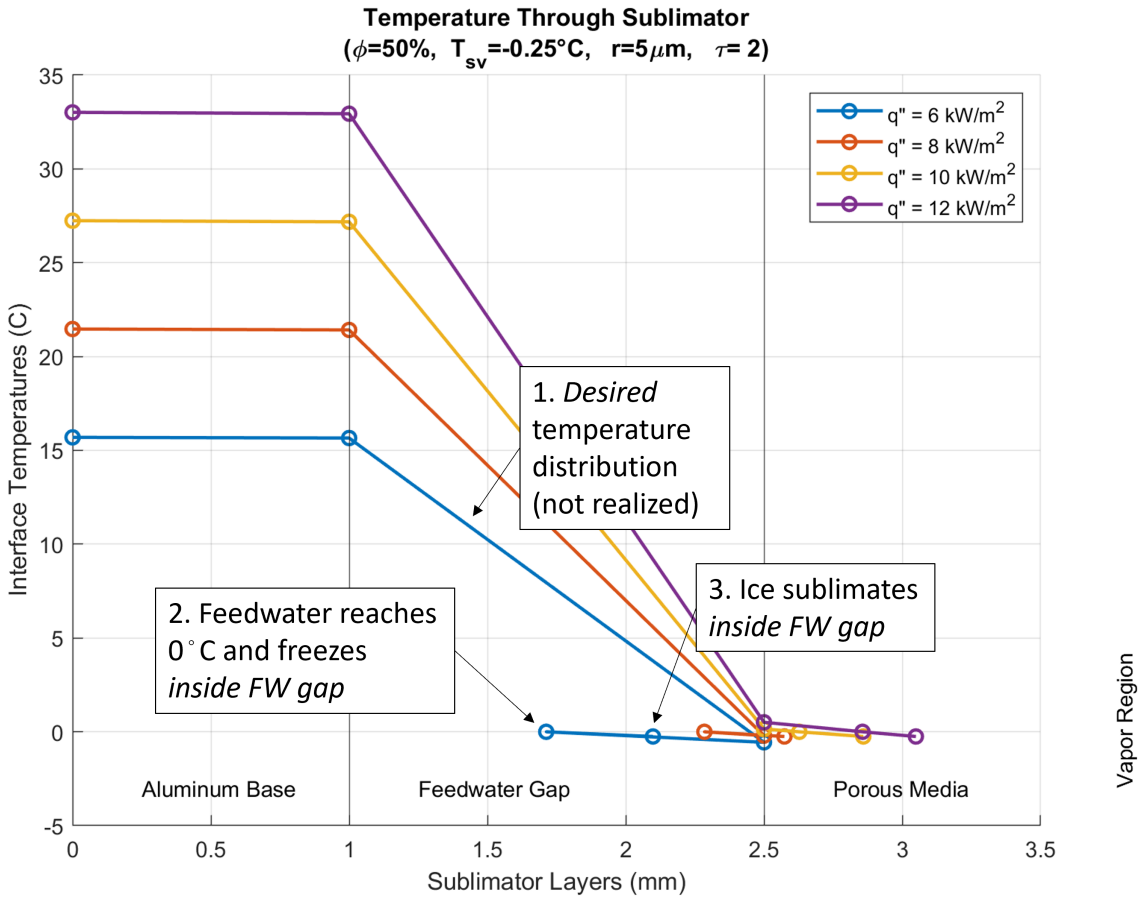

Figure 6.5: Temperature distribution for an example of a non-realizable set of sublimator parameters.

The realizability plots in Figure 6.6 also show that the greater the heat flux, the less stringent the design parameters. In other words, if the sublimator is *too* cold, the ice layer may be too thick which agrees with historical descriptions of too much ice expanding past the edge of the porous medium. These realizability plots are not connected to historical data because there is not enough detail or specific information about past porous media. For example and most notably, the EMU sublimator's porous medium has a porosity and pore size that varies through its depth, but only the parameters of the outer edges can be measured and reported. The realizability plots in Figure 6.6 can be used to identify design points for the sublimator based on big-picture heat rejection requirements for the mission.

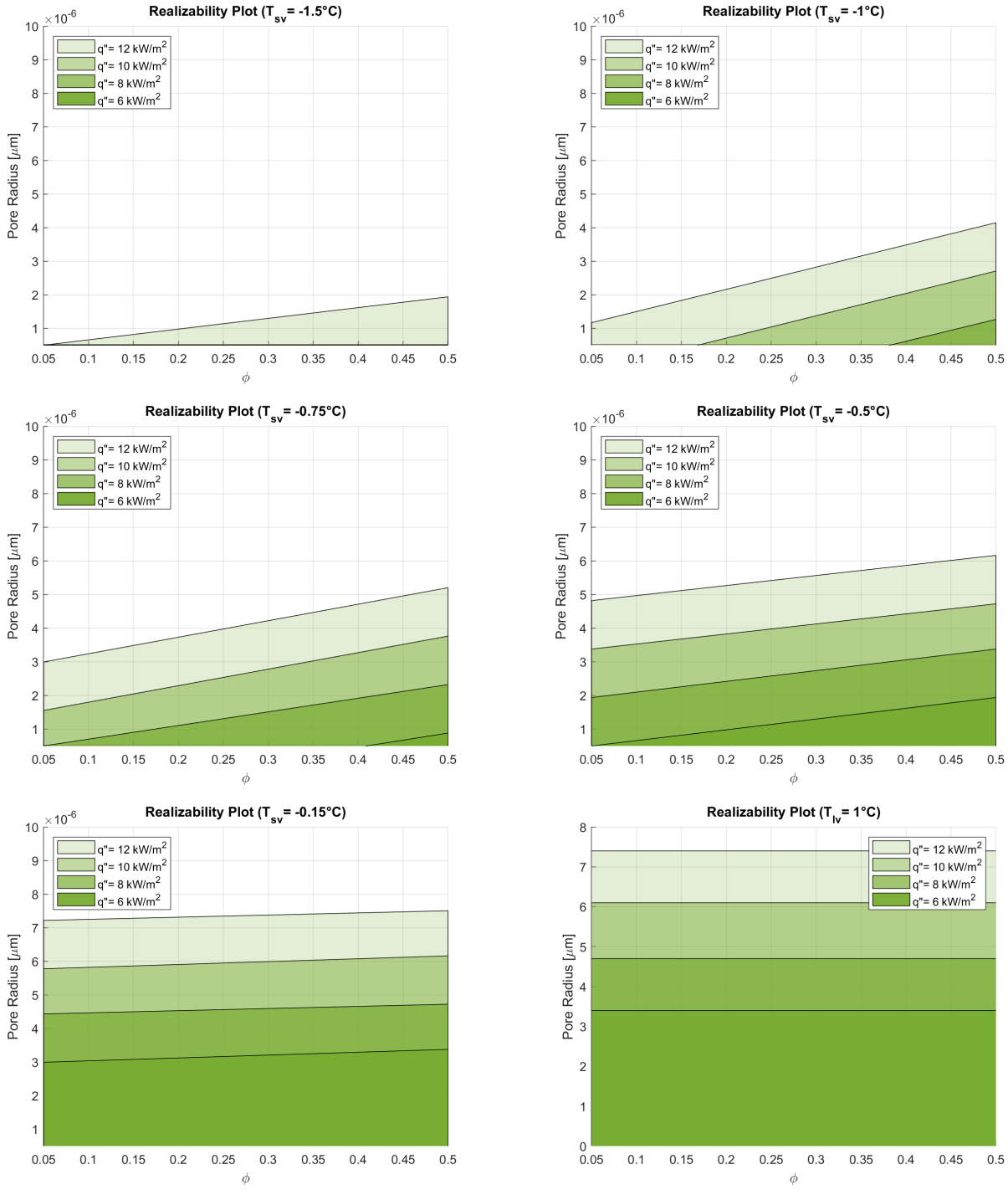

Figure 6.6: Realizable ranges for pore size and porosity for a CubeSat sublimator.

Chapter 7

Conclusion

7.1 Summary of Contributions

This thesis consolidated information about sublimators, especially resources from those in industry who have recently worked on sublimator technology. An initial sizing procedure was proposed for determining the mass, volume, and general configuration of a CubeSat thermal control system/sublimator based on mission requirements. Next, assumptions and shortcomings were identified from previous models and many of them were addressed in this research. Some of those assumptions were supported while others were shown to be inapplicable. An analytical model was used to describe heat conduction through the sublimator and water vapor diffusion through the porous medium, which was validated with an experiment. Both the experiment and the Weber model were compared to reported information from the manufacturer about porous media for further validation. This model, coupled with a series of conduction equations, was used to determine the phase change locations and water/ice/vapor region thicknesses. The model and experiment ultimately relate the small-scale sublimator design choices to the bigger picture mission requirements such as heat rejection capacity. In addition, connections were made with individuals at NASA centers (Goddard Space Flight Center and Ames Research Center) who have not worked directly on sublimator technology but whose fields of work help contribute to this research, namely Dr. John Ferguson (a PuMA creator) and Frank Robinson (the lead of a GSFC thermal lab). This thesis describes the groundwork that was laid for CubeSat applications of sublimator heat rejection

so that future students may make more informed decisions when designing, manufacturing, and testing CubeSat sublimators as well as quantifying their performance.

7.2 Open Research Areas & Future Work

CubeSat heat rejection is a novel application of sublimator technology, and the mechanisms of the sublimation process have been studied for sixty years. Even so, as discussed throughout this thesis, there are still some knowledge gaps in the understanding of sublimator function. This thesis addressed some of those knowledge gaps, and the areas where more research is required are outlined here. Sections 5.3 and 5.4 outline the lessons learned and future improvements pertaining specifically to the experiment conducted at NASA Goddard Space Flight Center. This section describes the future direction of this sublimator research, listed in chronological order according to which gaps the author thinks should be addressed first.

Sublimator Manufacturing and Experiment: Important knowledge, and experience is gained from hands-on experience. This is especially true for sublimator manufacturing: reading about the manufacturing challenges is not the same as working through them. Many of the anomalies seen in the past are attributed to manufacturing methods so special attention must be paid when assembling (especially welding/brazing) a sublimator. The addition of fins in the feedwater gap should be explored to enhance heat transfer across the region. A test sublimator should be manufactured to conduct a complete sublimator experiment to validate or correct the combined conduction and rarefied diffusion model. If a rarefied vapor flow experiment were to be conducted again prior to a full sublimator experiment, then flow from a wider range of Knudsen numbers should be tested to capture behavior in the transition regime which is more likely to occur in the evaporation mode.

Evaporation & Permeability Coefficients: Additional research is required which focuses on evaporation in the sublimator, especially if a combination of sublimation and evaporation occur simultaneously within the porous medium volume or if a cyclical process occurs between sublimation and evaporation, as has been suggested in the past [15, 52]. In the evaporation mode, the vapor pressure in the porous medium could be high enough that the Knudsen number is well in the transition regime near the Knudsen mini-

mum. More research is required to explore why there is not always agreement between the permeability coefficient, Weber model, and Knudsen minimum. The porous medium surface characteristics should be further characterized using parameters such as water surface tension, wettability, hydrophobicity/hydrophillicity, and surface roughness. These parameters influence the percolation of water through the porous medium but the specific ways in which they may affect the sublimation process remains to be seen.

CubeSat TCS Integration As discussed in Chapter 3, the overall CubeSat thermal control system is another area of exploration. The first interest is how the sublimator can be utilized during a mission as a source of propulsion to counteract orbital disturbances. The second interest is setting up a more comprehensive thermal balance for the CubeSat and sublimator TCS. In addition, further exploration into the various sublimator configurations other than the "sandwiched" or "open" configurations is warranted.

Miscellaneous Model Improvements: The feedwater enters the sublimator at a higher temperature than the triple point and equilibrates with the porous medium as described in Section 5.2.4. However, for model completeness, the sensible heat could be incorporated into the conduction model because the feedwater does need to cool down. This sensible heat is minimal compared to the latent heat associated with sublimation/evaporation. More research is also required to explore exactly how the porous nature of the sublimator affects its optical properties, but regardless of the geometry, stainless steel is not a good radiative surface.

Sublimator Performance Metric: When the UC Davis Center for Spaceflight Research builds and tests sublimator hardware, an important metric for comparison is specific heat rejection as in Table 2.1. The sublimator's waste heat rejection capacity per unit mass or unit volume may be especially important on a CubeSat where mass and volume must be optimized.

Numerical Methods for Analysis in Higher Dimensions: While the focus of this research was not one of numerical methods, using CFD could supplement an analytical model. The use of a CFD software such as Ansys or COMSOL requires an in-depth understanding of numerical methods and could be a useful stand-alone research direction to pursue. Both of these software packages would provide more insight into dynamic movements of the

phase-change interfaces in all three dimensions. Additional use of PuMA to capture other characteristics, such as permeability, is worth exploring, as discussed in Section 5.1.1. Dr. Ferguson also suggested using PuMA to obtain diffusion coefficients in all three dimensions for water vapor in the transition and rarefied flow regimes. These coefficients could then be used in Fick's law of diffusion, which typically only applies to continuum flow.

A two- and three-dimension model may help to capture "hot spots" throughout the porous medium or any edge effects (unique interaction between the aluminum frame and the porous medium). Both of these scenarios could increase the risk of anomalous behavior such as feedwater breakthrough. Conduction through the feedwater/porous medium and ice/porous medium sections of the sublimator are assumed to be one-dimensional. Even though the thermal conductivities are modified to account for a mix of water or ice and stainless steel, a specific effort to model this conduction process as three-dimensional could add insight into the freezing interface and the ice thickness, especially if it varies throughout the porous medium. A possible approach could be to model this conduction in COMSOL or Thermal Desktop using the 3D model obtained from the X-ray tomography scan.

The Weber equation for rarefied vapor diffusion is for one dimension, but diffusion in all three dimensions should be captured for a complete sublimator model. There is not currently an analytical multi-dimensional approach using the Weber equation. However, a conversation with Dr. Ferguson, one of the creators of PuMA, suggested that diffusion concepts can be used, such as Fick's law of diffusion, which typically only applies to the continuum regime. PuMA could be used to obtain the diffusion coefficient for rarefied water vapor using real 3D tomography of porous media. This diffusion coefficient could then be used in Fick's law of diffusion to find a relationship between pressure (or concentration) and mass flow rate. It is not yet clear if this diffusion-based approach could provide any additional insight into the phase change interfaces in three dimensions, or if this approach is simply a substitute for the water vapor flow model to obtain some average vapor region thickness.

Transient/Cyclical Analysis: This research touched on the sublimator transient start-up conceptually but a mathematical description should be developed for completeness. Previous sublimator use, both in flight and on the ground, is reported to have taken 30 seconds

to a few minutes to reach steady-state. Few other details are provided so a transient start-up model should be validated with an experiment as well.

The work presented in this thesis lays the foundation for future research to understand sublimator behavior, improve sublimator performance, and enable CubeSats to fly with more power-dense payloads on more complex missions. This research includes details about sublimator modeling, operation, and spacecraft integration — offering a notable contribution which, taken all together, turns the "art" of sublimators into a science.

Bibliography

[1] Kulu, E. "Nanosatellite Launch Forecasts - Track Record and Latest Prediction". In: 36th Annual Small Satellite Conference. Logan, UT, 2022. DOI: SSC22-S1-04.

[2] *State-of-the-Art: Small Spacecraft Technology*. NASA/TP—20210021263. Moffett Field, CA: Ames Research Center, Oct. 2021. URL: https://www.nasa.gov/smallsat-institute/sst-soa.

[3] *CHOMPTT (CubeSat Handling of Multisystem Precision Time Transfer)*. ESA Earth Observation Portal. Aug. 2019. URL: https://www.eoportal.org/satellite-missions/chomptt#spacecraft (visited on 01/26/2023).

[4] Conklin, J.W. et al. "Preliminary results from the CHOMPTT laser time-transfer mission". In: 33rd Annual AIAA/USU Conference on Small Satellites. Logan, UT, 2019, SSC19–VI–03.

[5] Butler-Craig, N.I. "An Investigation of the Thermal Behavior of High Power Density 3U CubeSats Capable of Supporting High-Impulse Missions". In: *2018 Joint Propulsion Conference*. Cincinnati, Ohio: American Institute of Aeronautics and Astronautics, July 9, 2018. ISBN: 978-1-62410-570-8. DOI: 10.2514/6.2018-4972.

[6] Davidson, R. et al. "CubeSat active thermal management in support of cooled electro-optical instrumentation for advanced atmospheric observing missions". In: CubeSats and NanoSats for Remote Sensing II. Ed. by C.D. Norton and T.S. Pagano. San Diego, United States: SPIE, Sept. 18, 2018, p. 6. DOI: 10.1117/12.2321959.

[7] Fennel, T. "Thermal Management Design of a 6U CubeSat with a High-Power Additive Manufacturing Payload Using Analytical Modeling with Experimental Validation". Master of Science. Melbourne, FL: Florida Institute of Technology, May 2020.

[8] Banker, Brian and Askew, Scott. "Seeker 1.0: Prototype Robotic Free Flying Inspector Mission Overview". In: 33rd Annual Conference on Small Satellites. Logan, UT, July 2019, SSC19–XI–04.

[9] Bomani, Bilal M M. *CubeSat Technology Past and Present: Current State-of-the-Art Survey*. NASA/TP-20210000201. Cleveland, Ohio: Glenn Research Center, 2021.

[10] Santa Maria, Sergio R., Zea, Luis, and Ricco, Tony. "Biological CubeSats: What Have We Learned so Far and What Is Next?" Nov. 20, 2019. URL: https://ntrs.nasa.gov/citations/20190033204 (visited on 05/01/2024).

[11] Commons, Wikimedia. *Phase diagram of awter simplified*. 2023. URL: https://commons.wikimedia.org/wiki/File:Phase_diagram_of_water_simplified.svg.

[12] Hansen, T.C. "The everlasting hunt for new ice phases". In: *Nature Communications* 12.1 (May 26, 2021), p. 3161. ISSN: 2041-1723. DOI: 10.1038/s41467-021-23403-6.

[13] Miao, J. et al. *Spacecraft Thermal Control Technologies*. Space Science and Technologies. Singapore: Springer Singapore, 2021. ISBN: 9789811549830. DOI: 10.1007/978-981-15-4984-7.

[14] Andish, K. *X-38 Contamination-Insensitive Sublimator - Model Development and Analysis*. Jacobs Engineering an Science Contract Group Report ESCG-4007-05-TEAN-DOC-0099. NASA Johnson Space Center, Aug. 2005.

[15] Chapman, A. *A Fundamental Study of Sublimation Through a Porous Surface*. Contract NAS 9-7969. Houston, TX: NASA Manned Spacecraft Center, July 1971.

[16] *EMU Requirements Evolution, Rev B*. Extravehicular Activity (EVA) Systems Contract SEMU-66-017B. NASA Johnson Space Center, Sept. 2005.

[17] Gilmore, D.G. *Spacecraft Thermal Control Handbook*. 2nd ed. The Aerospace Corporation, 2002.

[18] Lemmon, E.W. et al. *NIST Standard Reference Database 23: Reference Fluid Thermodynamic and Transport Properties-REFPROP, Version 10.0, National Institute of Standards and Technology*. 2018. DOI: https://doi.org/10.18434/T4/1502528. URL: https://www.nist.gov/srd/refprop.

[19] Hamilton Sundstrand Space Systems International, Inc. *Assured EMU Availability; Fleet Leader Evaluation Report; Round 4; Life Extension from 30 to 35 years; Item 140; Porous Plate Sublimator*. Houston, TX: NASA Johnson Space Center, 2008.

[20] Leimkuehler, T. "Contaminant Insensitive Sublimator Conceptual Design Review". NASA Johnson Space Center, Feb. 2006.

[21] Liao, J., Yang, C., and Yang, H. "Numerical simulation of a porous plate water sublimator working in the periodic mode and analytical study of its evaporation process". In: *Applied Thermal Engineering* 216 (Nov. 2022), p. 119088. ISSN: 13594311. DOI: 10.1016/j.applthermaleng.2022.119088.

[22] White, F. *Fluid Mechanics*. 8th ed. New York: McGraw-Hill, 2016.

[23] Moran, M. et al. *Fundamentals of Engineering Thermodynamics*. 7th ed. Wiley and Sons, Inc., 2011.

[24] Incropera, F. et al. *Fundamentals of Heat and Mass Transfer*. 6th. John Wiley & Sons, 2007.

[25] Chang, K., Wang, Y., and Li, Y. "A review of water sublimation cooling and water evaporation cooling in complex space environments". In: *Progress in Aerospace Sciences* 140 (July 2023), p. 100930. DOI: 10.1016/j.paerosci.2023.100930.

[26] Rannenberg, G., Granby, E., and J., Lovell. *Sublimator*. U.S. Patent 3170303. Feb. 1965.

[27] *Suit Heat Exchanger Assembly*. Item 1.29. Houston, TX: NASA Johnson Space Center, 1969.

[28] Ridings, T.L. and Southerlan, R.E. *Performance Evaluation of the Saturn Instrument Unit Environmental Control System Sublimator Under Simulated flight Conditions*. AEDC-TR-66-235. Arnold Air Force Station, TN: Air Force Systems Command, Feb. 1967, p. 125.

[29] *Portable Life Support System*. Apollo News Conference. Hamilton Standard/NASA.

[30] Hepner, P. H. and Sangiovanni, J. J. *Porous plate water boiler design study final report*. May 20, 1965. URL: http://archive.org/details/nasa_techdoc_19680069313.

[31] Shero, J. "Porous Plate Sublimator Analysis". Doctor of Philosophy. Rice University, Nov. 1969.

[32] Thomas, Kenneth. *The Apollo Portable Life Support System*. white paper.

[33] *Apollo 11: A mission that redefined space exploration*. July 19, 2019. URL: https://www.collinsaerospace.com/news/stories/2019/07/apollo-11-redefining-space-exploration.

[34] Gillen, Richard, Elliot, Frank, and Wilde, Richard. "Lunar Module Environmental Control Subsystem". In: Aeronautic and Space Engineering and Manufacturing Meeting. Feb. 1, 1969. DOI: 10.4271/690619.

[35] Thomas, G. "Packaging Factors for Portable Life Support Subsystems Based on Apollo and Shuttle Systems". In: 23rd International Conference on Environmental Systems. Colorado Springs, CO, July 1993.

[36] *NASA Extravehicular Mobility Unit (EMU) LSS/SSA Data Book*. Rev V. UTC Aerospace Systems, Sept. 2017.

[37] Leimkuehler, T. "Contaminant Insensitive Sublimator Feed Water Model". NASA Johnson Space Center, July 2007.

[38] Steele, J. et al. "Management of the Post-Shuttle Extravehicular Mobility Unit (EMU) Water Circuits". In: 42nd International Conference on Environmental Systems. San Diego, California: American Institute of Aeronautics and Astronautics, July 15, 2012. ISBN: 978-1-60086-934-1. DOI: 10.2514/6.2012-3593.

[39] Abramov, I.P. and Skoog, A.I. *Russian Spacesuits*. Springer-Praxis, 2003.

[40] Moiseev, N. "Life Support Systems for Russian IVA/EVA Space Suits". In: *Handbook of Life Support Systems for Spacecraft and Extraterrestrial Habitats*. Ed. by E. Seedhouse. Cham: Springer International Publishing, 2016. ISBN: 978-3-319-09575-2. DOI: 10.1007/978-3-319-09575-2_208-1.

[41] Planert, C., Kremer, P., and Witt, J. "Development of Sublimator Technology for the European EVA Space Suit". In: *Space Station and Advanced EVA*. Vol. SP-872. SAE International, pp. 201–207. DOI: 911577.

[42] Tongue, S. and Dingell, C.W. "The Porous Plate Sublimator as the X-38/CRV (Crew Return Vehicle) Orbital Heat Sink". In: *SAE Transactions* 108 (1999), pp. 488–495. ISSN: 0096-736X.

[43] RaviPrakash, G.K. and Leimkuehler, T. *Analysis of Contaminant Insensitive Sublimator October - November 2007 Test Data*. ESCG-4470-08-TEAN-DOC-0266. Houston, TX: Jacobs Engineering and Science Contract Gorup, June 2008, p. 34.

[44] Leimkuehler, T., Abounasr, O., and Stephan, R. "Design of a Sublimator Driven Coldplate Development Unit". In: *SAE International Journal of Aerospace* 1 (Jan. 2008), pp. 532–536. DOI: 10.4271/2008-01-2169.

[45] Sheth, R., Stephan, R., and Leimkuehler, T. "Sublimator Driven Coldplate Engineering Development Unit Test Results". In: 40th International Conference on Environmental Systems. Barcelona, Spain: American Institute of Aeronautics and Astronautics, July 11, 2010. ISBN: 978-1-60086-957-0. DOI: 10.2514/6.2010-6082.

[46] Leimkuehler, T. and Bower, C. "Integrated Sublimator Driven Coldplate (ISDC) for Thermal Control Systems". In: 45th International Conference on Environmental Systems. Bellevue, Washington, July 2015, p. 10.

[47] Sheth, R., Stephan, R., and Leimkuehler, T. "Investigation of Transient Performance for a Sublimator". In: 40th International Conference on Environmental Systems. Barcelona, Spain: American Institute of Aeronautics and Astronautics, July 11, 2010.

[48] Hecht, J. et al. "Water Removal Performance of the Humidity Control Subassembly with Variable Vacuum Orifice Sizing". In: 50th International Conference on Environmental Systems. virtual, 2020.

[49] Xianwen, N. et al. "Design and implementation of the integrated thermal control system for Chang'E-5 lunar module". In: *Acta Astronautica* 200 (2022), pp. 188–195. DOI: 10.1016/j.actaastro.2022.08.005.

[50] Wang, Y. et al. "Numerical and experimental study on the heat and mass transfer of porous plate water sublimator with constant heat flux boundary condition". In: *Applied Thermal Engineering* 67.1 (June 2014), pp. 469–479. ISSN: 13594311. DOI: 10.1016/j.applthermaleng.2014.02.059.

[51] Gao, L. et al. "Numerical Investigation on Heat-Transfer and Hydromechanical Performance inside Contaminant-Insensitive Sublimators under a Vacuum Environment for Spacecraft Applications". In: *Energies* 12 (2019). DOI: http://dx.doi.org/10.3390/en12234562.

[52] Zhang, C. et al. "Simulation of evaporation and sublimation process in porous plate water sublimator based on a reduced CFD model — Elsevier Enhanced Reader". In: *International Journal of Heat and Mass Transfer* 154 (June 2020). DOI: 10.1016/j.ijheatmasstransfer.2020.119787.

[53] Wang, Y. et al. "Influences of mass flow rate on heat and mass transfer performances of water sublimator combined with fluid loop". In: *Chinese Journal of Aeronautics* 32 (Feb. 1, 2019). DOI: 10.1016/j.cja.2019.01.010.

[54] Avantor. *Nusil*. https://nusil.avantorsciences.com/nusil/en/product/CV-9341/thermally-conductive-controlled-volatility-silicone-grease [Accessed: February 2024]. 2023.

[55] Laird. *Tflex Interface Material*. https://www.laird.com/products/thermal-interface-materials/gap-fillers/tflex-hd80000/a17882-08 [Accessed: February 2024]. 2023.

[56] Commons, Wikimedia. *Heat Pipe Mechanism*. 2016. URL: https://commons.wikimedia.org/wiki/File:Heat_Pipe_Mechanism.svg.

[57] Thermal-Space. *Thermal Straps*. https://thermal-space.com/thermal-straps/ [Accessed: February 2024].

[58] Goodman, John L. "Apollo 13 Guidance, Navigation, and Control Challenges". In: AIAA Space 2009 Conference and Exposition. Pasadena, CA, Jan. 1, 2009. (Visited on 03/27/2024).

[59] Mesfin, Y. "Investigation of a " Phantom" Disturbance Torque Sensed on Space Station during Russian EVAs". In: 2006 IEEE Aerospace Conference. Mar. 2006. DOI: 10.1109/AERO.2006.1656153.

[60] Wertz, J., Everett, D., and Puschell, J. *Space Mission Engineering: The New SMAD*. Hawathorne, CA: Microcosm Press, 2011.

[61] Montenbruck, O. and Gill, E. *Satellite Orbits: Models, Methods, Applications*. Springer, 2000.

[62] Leimkuehler, T. "Sublimator Calculations". Honeywell/NASA Johnson Space Center, Feb. 2005.

[63] Stephan, R. "Overview of the Altair Lunar Lander Thermal Control System Design". In: 40th International Conference on Environmental Systems. Barcelona, Spain: American Institute of Aeronautics and Astronautics, July 11, 2010.

[64] Weislogel, M. *Convseration with Dr. Mark Weislogel*. personal communication. June 2023.

[65] Leimkeuhler, T. *Convseration with Dr. Tom Leimkuehler*. personal communication. May 2023.

[66] Boomsma, K. and Poulikakos, D. "On the effective thermal conductivity of a three-dimensionally structured fluid-saturated metal foam". In: *International Journal of Heat and Mass Transfer* 55 (2001). DOI: 10.1016/S0017-9310(00)00123-X.

[67] Smith, D. et al. "Thermal Conductivity of Porous Materials". In: *Journal of Materials Research* 28 (Sept. 14, 2013). DOI: 10.1557/jmr.2013.179.

[68] Kossacki, K. et al. "Sublimation coefficient of water ice under simulated cometary-like conditions". In: *Planetary and Space Science* 47 (1999), pp. 1521–1530. DOI: 10.1016/S0032-0633(99)00037-9. (Visited on 10/24/2022).

[69] Hołyst, R., Litniewski, M., and Jakubczyk, D. "A molecular dynamics test of the Hertz–Knudsen equation for evaporating liquids". In: *Soft Matter* 11.36 (2015), pp. 7201–7206. ISSN: 1744-683X, 1744-6848. DOI: 10.1039/C5SM01508A.

[70] Comet Technologies, Canada. *Dragonfly*. Version 2022.2. URL: https://theobjects.com/dragonfly/index.html.

[71] Ferguson, J.C. et al. "PuMA: The porous microstructure analysis software". In: *SoftwareX* 7 (2018), pp. 81–87.

[72] *Mott Porous Metal Data Sheet*. Data Sheet. URL: https://mottcorp.com/resource/316l-stainless-steel-pressed-disc-062-thick-permeability/.

[73] Carey, V.P. *Liquid-Vapor Phase-Change Phenomena*. 3rd ed. CRC Press, 2020.

[74] Scott, K. "Membraine Materials, Preparation, and Characterisation". In: *Handbook of Industrial Membranes*. Amsterdam: Elsevier Science, Jan. 1, 1995, pp. 187–269. ISBN: 978-1-85617-233-2. DOI: 10.1016/B978-185617233-2/50005-2.

[75] *Swagelok Filters (MS-01-92)*. URL: https://www.swagelok.com/downloads/webcatalogs/en/ms-01-92.pdf (visited on 10/03/2023).

[76] Clennell, M. B. "Tortuosity: a guide through the maze". In: *Geological Society Publications* 122.1 (1997), pp. 299–344. DOI: 10.1144/GSL.SP.1997.122.01.18.

[77] Ghanbarian, B. et al. "Tortuosity in Porous Media: A Critical Review". In: *Soil Science Society of America Journal* 77.5 (2013), pp. 1461–1477. ISSN: 1435-0661. DOI: 10.2136/sssaj2012.0435.

[78] Ferguson, J.C. et al. "Continuum to rarefied diffusive tortuosity factors in porous media from X-ray microtomography". In: *Computational Materials Science* 203 (Feb. 15, 2022), p. 111030. ISSN: 0927-0256. DOI: 10.1016/j.commatsci.2021.111030.

[79] Elwinger, F., Pourmand, P., and Furó, I. "Diffusive Transport in Pores. Tortuosity and Molecular Interaction with the Pore Wall". In: *The Journal of Physical Chemistry C* 121.25 (June 29, 2017). Publisher: American Chemical Society, pp. 13757–13764. DOI: 10.1021/acs.jpcc.7b03885. (Visited on 02/07/2024).

[80] Wikimedia. *MSD Anomalous Diffusion*. https://commons.wikimedia.org/wiki/File:Msd_anomalous_diffusion.svg [Accessed: February 2024]. 2012.

[81] Fu, Jinlong, Hywel, Hywel R., and Li, Chenfeng. "Tortuosity of porous media: Image analysis and physical simulation". In: *Earth-Science Reviews* 212 (2021). DOI: https://doi.org/10.1016/j.earscirev.2020.103439.

[82] Ellgen, P. *Thermodynamics and Chemical Equilibrium*. Oklahoma School of Science Mathematics, 2024. ISBN: 1-4921-1427-8.

[83] Gad-el-Hak, M. "The Fluid Mechanics of Microdevices, The Freeman Scholar Lecture". In: *Journal of Fluids Engineering* 121 (Mar. 1999), pp. 5–33.

[84] Mason, E.A. and Malinauskas, A.P. *Gas Transport in Porous Media: The Dusty-gas Model*. Vol. 17. Chemical Engineering Monographs. Amsterdam, The Netherlands: Elsevier Science Publishers B.V., 1983. ISBN: 0-444-42190-4.

[85] Maxwell, J. C. "Illustrations of the dynamical theory of gases". In: *The London, Edinburgh, and Dublin Philosophical Magazine and Journal of Science* 20.130 (July 1860), pp. 21–37. DOI: 10.1080/14786446008642902.

[86] Caravella, Alessio. "Dusty-Gas Model (DGM)". In: *Encyclopedia of Membranes*. Ed. by Enrico Drioli and Lidietta Giorno. Berlin, Heidelberg: Springer, 2016, pp. 604–605. DOI: 10.1007/978-3-662-44324-8_1737.

[87] Cai, J. et al. "Lucas–Washburn Equation-Based Modeling of Capillary-Driven Flow in Porous Systems". In: *Langmuir* 37.5 (Feb. 9, 2021). Publisher: American Chemical Society, pp. 1623–1636. ISSN: 0743-7463. DOI: 10.1021/acs.langmuir.0c03134.

[88] Aldoury, Muzher. "A Discussion About Hydraulic Permeability and Permeability". In: *Petroleum Science and Technology* 28 (Oct. 1, 2010), pp. 1740–1749.

[89] Dyer, D.F. and Sunderland, J.E. "Heat and Mass Tranfser Mechanisms in Sublimation Dehydration". In: *Journal of Heat Transfer* (1968).

[90] Ungar, E. and Almlie, J. "The Water Membrane Evaporator for Space Shuttle Heat Rejection: Membrane Performance and Plans for Pre-Prototype Testing". In: *Proceedings of 2000 IMECE*. International Mechanical Congress and Exposition. Orlango, FL: ASME, Nov. 2000.

[91] Weber, S. "The Connection Between the Laminar Flow of Pure Gases Through Tubes and the Self-Dissusion Coefficient". Danish and English. Trans. by R. Ash and J. B. Sykes. In: *Library, Atomic Energy Research Establishment* (1963).

[92] Scott, T.E. and Milligan, M.W. "Rarefied Gas Flow Through Ultra-Fine Filtering Media". In: *Process Industries Division*. ASME Winter Annual Meeting. Los Angeles, CA, 1969.

[93] Agrawal, A., Kushwaha, H.M., and Jadhav, R.S. *Microscale Flow and Heat Transfer: Mathematical Modelling and Flow Physics*. Mechanical Engineering Series. Springer International Publishing, 2020. DOI: 10.1007/978-3-030-10662-1.

[94] Present, R.D. *Kinetic Theory of Gases*. MCGraw-Hill, 1958.

[95] Billen, M. *2.5: Darcy's Law - Flow in a Porous Medium*. Geosciences LibreTexts. Jan. 25, 2019. URL: https://geo.libretexts.org/Courses/University_of_California_Davis/GEL_056%3A_Introduction_to_Geophysics/Geophysics_is_everywhere_in_geology.../02%3A_Diffusion_and_Darcy's_Law/2.05%3A_Darcy's_Law_-_Flow_in_a_Porous_Medium.

[96] Wadsworth, F.B. et al. "A universal model for the permeability of sintered materials". In: *Acta Materialia* 250 (May 2023). ISSN: 13596454. DOI: 10.1016/j.actamat.2023.118859.

[97] Klinkenberg, L.J. "The Permeability of Porous Media to Liquids and Gases". In: *Production Practice* (1947), pp. 200–214.

[98] Orlander, T., Milsch, H., and Fabricius, I.L. "Comparison of gas, Klinkenberg, and liquid permeability of sandstone: Flow regime and pore size". In: *AAPG Bulletin* 105.7 (July 2021), pp. 1383–1403.

[99] Knudsen, Martin. "Die Gesetze der Molekularströmung und der inneren Reibungsströmung der Gase durch Röhren". In: *Annalen der Physik* 333.1 (1909), pp. 75–130. ISSN: 1521-3889. DOI: 10.1002/andp.19093330106.

[100] Clifford K. Ho and S. W. Webb, eds. *Gas transport in porous media*. Theory and applications of transport in porous media v. 20. Dordrecht: Springer, 2006. 444 pp. ISBN: 978-1-4020-3961-4.

[101] Anez, L. et al. "Gas and liquid permeability in nano composites gels: Comparison of Knudsen and Klinkenberg correction factors". In: *Microporous and Mesoporous Materials* 200 (Dec. 1, 2014), pp. 79–85. ISSN: 1387-1811. DOI: 10.1016/j.micromeso.2014.07.049.

[102] Ziarani, A.S. and Aguilera, R. "Knudsen's Permeability Correction for Tight Porous Media". In: *Transport in Porous Media* 91.1 (Jan. 2012), pp. 239–260. ISSN: 0169-3913, 1573-1634. DOI: 10.1007/s11242-011-9842-6.

[103] Tang, G.H., Tao, W Q., and He, Y L. "Gas slippage effect on microscale porous flow using the lattice Boltzmann method". In: *Physical Review E* 72.5 (Nov. 1, 2005). Publisher: American Physical Society, p. 056301. DOI: 10.1103/PhysRevE.72.056301.

[104] Qiu, K. *ZoomPlot*. https://github.com/iqiukp/ZoomPlot-MATLAB/releases/tag/v1.5.1. Retrieved 13 March 2014. 2024.

[105] *Sigray*. URL: https://sigray.com/.

[106] Otsu, N. "A Threshold Selection Method from Gray-Level Histograms". In: *IEEE Transactions on Systems, Man, and Cybernetics* 9.1 (Jan. 1979), pp. 62–66. ISSN: 0018-9472, 2168-2909. DOI: 10.1109/TSMC.1979.4310076.

[107] Ferguson, J.C. et al. "Update 3.0 to "PuMA: The Porous Microstructure Analysis software",(PII: S2352711018300281)". In: *SoftwareX* 15 (2021), p. 100775.

[108] Ferguson, J. *Convseration with Dr. John Ferguson*. personal communication. Mar. 2024.

[109] *RTD Temperature vs. Resistance Table*. Omega Engineering. URL: https://assets.omega.com/pdf/tables_and_graphs/thermistor-resistance-europe.pdf.

[110] Shoghl, S.N. et al. "Prediction of Joule-Thomson coefficient and inversion curve for natural gas and its components using CFD modeling". In: *Journal of Natural Gas Science and Engineering* 83 (2020). DOI: 103570.

Appendix A

The following steps outline the procedure for using Dragonfly, MatLab, and PuMA to obtain the parameters in Section 5.1.1.

1. Export the file from Dragonfly as a stack of 2D tiffs. The file should be a cropped sample of the 3D micro-tomography scan that does not reach the edges of the sample. A cuboid is the prefferred volume shape.

2. Use MatLab to compress the stack of 2D tiffs into a single 3D tiff file and convert the file from 16-bit to 8-bit. Use `im2uint8` and `imwrite`.

3. In PuMA, import the 3D tiff file, `Rescale Vis`, and adjust the `Vox Length` to the appropriate value (in this case it was 10 μm or 4.7 μm, set by the x-ray configuration).

4. Select `Material Properties`, `Porosity`. Through trial and error, find the appropriate grayscale range to yield a porosity that matches the porosity found in Dragonfly.

5. Select `Material Properties`, `Tortuosity`, `Random Walk`. Random walk is the approach in which a series of particles is "released" in the computational space and moves in a random direction at each solver step.

6. Set the rest of the conditions according to Figure A.1. Note that the grayscale range is determined in Step 4. The mean free path, in voxels, is set for one of two conditions:

   a) Continuum flow: set the mean free path to a voxel size to yield a Knudsen number < 0.001. The parameters calculated from the continuum regime were used in the Weber model, but theoretically they should be the same as those calculated in any other flow regime.

   b) Transition or Rarefied flow: set the mean free path to a voxel size calculated from the CubeSat sublimator conditions using Equation 4.19. This will yield a Knudsen number in the transition or rarefied flow regime.

7. From Figure A.1, the values for tortuosity in the x, y, and z directions were recorded. These values are very similar because the porous media is isotropic. The values for the diffusion coefficient in all three directions were also recorded and used to compute the characteristic length.

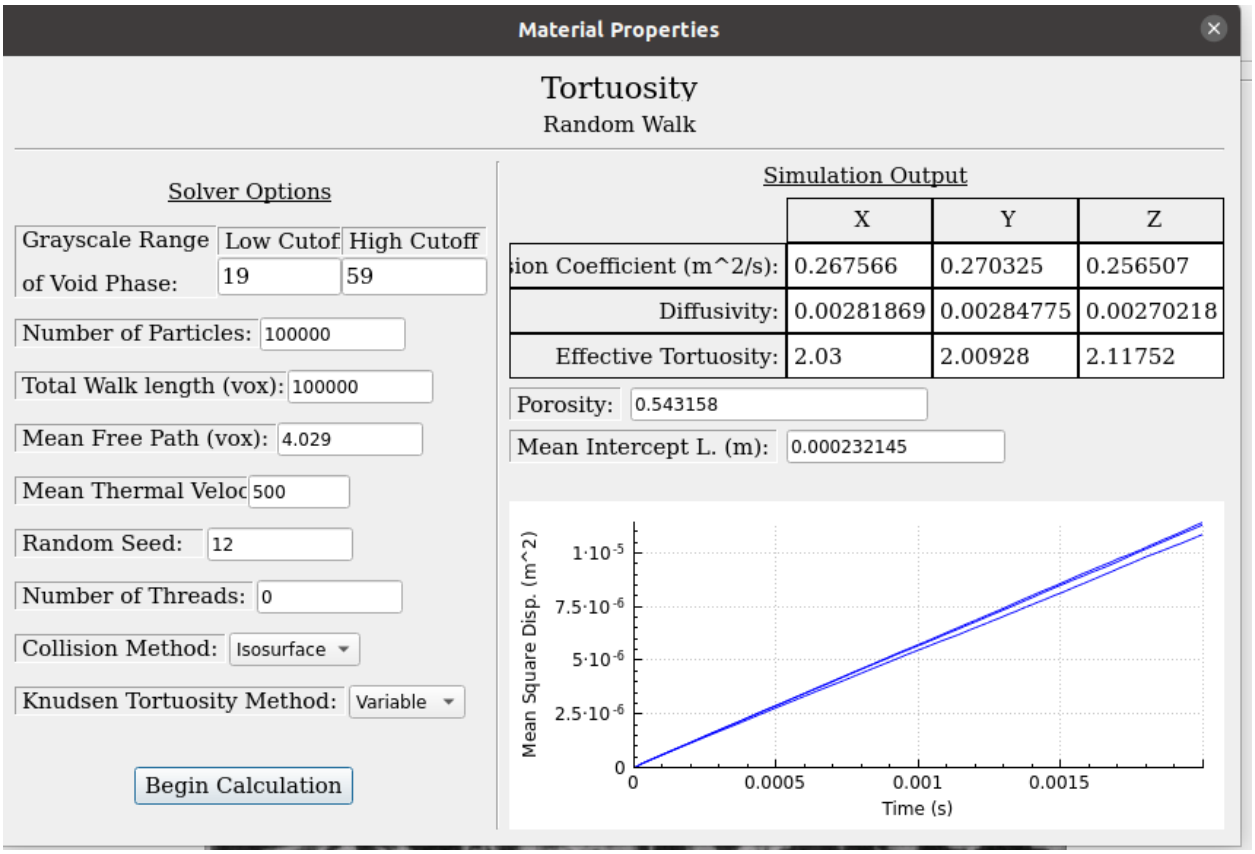

Figure A.1: Inputs for tortuosity calculation in PuMA.

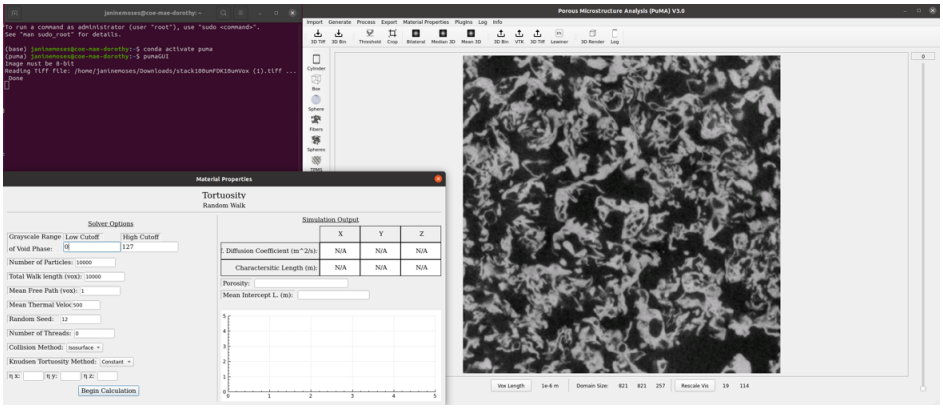

Figure A.2: PuMA GUI with terminal log (upper left), inputs for calculation (lower left), and .tiff file (right).

Table A.1: PuMA Results

Disk	Scan	Voxel Size	Flow Regime	Porosity	D_eff_x	D_eff_y	D_eff_z	tort_x	tort_y	tort_z
100 um (0.54)	FDK	10 um	Continuum	0.54	0.355294	0.3574	0.34321	1.52876	1.51975	1.58258
	Quad	10 um	Continuum	0.564844	0.391839	0.395957	0.392856	1.44152	1.42653	1.43779
	FDK	10 um	Transition	0.54	0.267566	0.270325	0.256507	2.030	2.009	2.118
	Quad	10 um	Transition	0.564844	0.305051	0.312135	0.301797	1.85164	1.80961	1.8716
40 um (0.4)	FDK	4.7 um	Continuum	0.396892	0.24571	0.246956	0.24516	1.615	1.607	1.619
	Quad	4.7 um	Continuum	0.253684	0.253288	0.251868	1.58464	1.58712	1.59607	0.402
	FDK	10 um	Continuum	0.39	0.205733	0.209958	0.201635	1.91711	1.87853	1.95607
	Quad	10 um	Continuum	0.389249	0.215878	0.215244	0.221101	1.80309	1.8084	1.7605
	FDK	4.7 um	Transition	0.40	0.121092	0.120546	0.137907	3.27759	3.29246	2.87797
	Quad	4.7 um	Transition	0.402	0.12752	0.120996	0.142816	3.15244	3.3224	0.8148
	FDK	10 um	Transition	0.39	0.124057	0.126045	0.127119	3.17928	3.12913	3.10269
	Quad	10 um	Transition	0.38925	0.00169012	0.00168709	0.133247	3.16813	3.17383	2.92125
20 um (0.47)	FDK	4.7 um	Continuum	0.359185	0.190171	0.192814	0.174804	1.88875	1.86286	2.05479
	Quad	4.7 um	Continuum	0.359302	0.194691	0.198594	0.184541	1.84549	1.80923	1.94701
	FDK	10 um	Continuum	0.381499	0.188337	0.19399	0.168293	2.02562	1.96659	2.26688
	Quad	10 um	Continuum	0.383298	0.20703	0.213834	0.216644	1.85141	1.79251	1.76925
	FDK	4.7 um	Transition	0.35919	0.0944184	0.0976654	0.0908815	3.80418	3.67771	3.95224
	Quad	4.7 um	Transition	0.3593	0.0961092	0.0990552	0.0974379	3.73847	3.62729	3.68749
	FDK	10 um	Transition	0.381499	0.102912	0.106305	0.0988298	3.70705	3.58873	3.86016
	Quad	10 um	Transition	0.383298	0.0999371	0.107727	0.130638	3.8354	3.55806	2.93406
10 um (0.44)	FDK	4.7 um	Continuum	0.38	0.208741	0.213128	0.202036	1.81676	1.77937	1.87706
	Quad	4.7 um	Continuum	0.400289	0.22792	0.234286	0.23124	1.75627	1.70855	1.73105
	FDK	4.7 um	Transition	0.38	0.101328	0.101586	0.105723	3.74264	3.73313	3.58705
	Quad	4.7 um	Transition	0.400289	0.112933	0.116355	0.128351	3.54449	3.44024	3.11871